Sophie Holme Stokker

Fatigue Design Appropriations for Floating Offshore Wind Turbine Support Structures

Master's thesis

NTNU
Norwegian University of Science and Technology
Faculty of Engineering
Department of Marine Technology

NTNU
Norwegian University of
Science and Technology

7 WAVES
NAVAL ARCHITECTS & MARINE ENGINEERS

Sophie Holme Stokker

Fatigue Design Appropriations for Floating Offshore Wind Turbine Support Structures

Master's thesis in Marine Technology
Supervisor: Bernt Johan Leira
Co-supervisor: Terje Skogan Bøe
June 2023

Norwegian University of Science and Technology
Faculty of Engineering
Department of Marine Technology

NTNU
Norwegian University of
Science and Technology

MASTER THESIS IN MARINE TECHNOLOGY
SPRING 2023
for

Master Student Sophie Holme Stokker

Fatigue Design Appropriations for Floating Offshore Wind Turbine Support Structures

Utmatting-analyse av Bære-konstruksjon for flytende vindturbiner

Background:

In recent years, the wind industry has seen a very fast development, moving from onshore to offshore and from shallow water fixed to deep water floating solutions. Many of the floating wind turbine concepts have been proposed for water depths larger than 100m. So far, the costs of energy of floating wind turbines are quite high as compared to bottom-fixed offshore wind turbines, and a lot larger than onshore turbines. Therefore, reducing the cost of the turbines is one of the main challenges the offshore wind turbines face.

One of the reasons for the high cost of offshore floating wind turbines is that the support structure (such as the floater and type of mooring system) is expensive to fabricate, install and maintain. Fatigue design considerations of these support structures are of key importance in this connection.

In the thesis work, the candidate shall look into the relative importance of wind and wave loading concerning the fatigue design of the floating support structure. A particular wind turbine concept is to be selected based on a discussion with the supervisors. Particular attention should also be paid to the degree of dynamic amplification of the induced load effects caused by these different sources.

Assignment:

The following topics should be addressed in the thesis work:

1. Literature study on wind turbines. Give a presentation on the development of wind turbines. Identify the different types of wind turbines and floaters.
2. Present the methods and theories used in the thesis, also by consideration of the applied computer software.
3. Establish beam models in SIMA for the selected floating wind turbine concept, including rigid body and flexible models. Analysis of eigenvalues and response due to static loading are to be performed to validate and observe the difference between the models.

4. Dynamic response due to regular waves is to be computed for a matrix of load cases agreed upon with the supervisors. Corresponding values of the dynamic response are to be quantified. A number of load cases due to dynamic wind actions are subsequently analyzed, also quantifying dynamic amplification effects.
5. Implications of the computed response levels in relation to relative magnitudes of the fatigue damage contributions due to these two sources of loading are to be highlighted.
6. If time permits, do a local analysis in Sesam Wind Turbine Manager, including making a model in HydroD for Wasim analysis.
7. Conclusions from the findings and recommendations for future work as part of the master thesis are also to be formulated.

The work scope may prove to be larger than initially anticipated. Subject to approval from the supervisors, topics may be deleted from the list above or reduced in extent.

In the project report, the candidate shall present their personal contribution to the resolution of problems within the scope of the project work

Theories and conclusions should be based on mathematical derivations and/or logical reasoning identifying the various steps in the deduction.

The candidates should utilize the existing possibilities for obtaining relevant literature.

Project report format
The project report should be organized in a rational manner to give a clear exposition of results, assessments, and conclusions. The text should be brief and to the point, with clear language. Telegraphic language should be avoided.

The report shall contain the following elements: A text defining the scope, a preface, a list of contents, a summary, a main body of the thesis, conclusions with recommendations for further work, a list of symbols and acronyms, references, and (optional) appendices. All figures, tables, and equations shall be enumerated.

The supervisors may require that the candidates, in an early stage of the work, present a written plan for the completion of the work.

The original contribution of the candidates and material taken from other sources shall be clearly defined. Work from other sources shall be properly referenced using an acknowledged referencing system.

The report shall be submitted in electronic format (.pdf):
- Signed by the candidates
- The text defining the scope shall be included (this document)
- Drawings and/or computer models that are not suited to be part of the report in terms of appendices shall be provided on separate (.zip) files.

Ownership

NTNU has according to the present rules, the owns the project reports. Any report use must be approved by NTNU (or external partner when this applies). The department has the right to use the report as if the work was carried out by a NTNU employee, if nothing else has been agreed in advance.

Thesis supervisors:

Prof. Bernt J. Leira, NTNU, bernt.leira@ntnu.no
Msc. Terje Skogan Bøe, 7Waves, terje.skogan.boe@7waves.no
Msc. John Riis, 7Waves, john.riis@7waves.no

Deadline: June 2023, as informed on the web

Preface

This Master's thesis is written by Stud. Techn. Sophie Holme Stokker in cooperation with 7Waves at the Norwegian University of Science and Technology (NTNU). The thesis serves as the final assignment to obtain the Master of Science degree in Marine Technology with a specialization in Marine structures. The work was carried out during the spring of 2023 and is a continuation of the Project thesis work submitted in the fall of 2022.

The aim of the thesis is to study the relative importance of wind and wave loading in relation to the fatigue design of floating support structures. While writing this thesis, I gained valuable knowledge about the support structure of floating offshore wind turbines and modeling in the SIMA simulation software.

My primary supervisor from NTNU during the Master's thesis work has been Prof. Bernt Johan Leira. I want to thank Prof. Bernt Johan Leira for sharing his expertise and always being available to help and providing relevant feedback.

Terje Skogan Bøe has been my supervisor from 7Waves. I want to thank Terje for being available to share his competence and for helping me with problems that have occurred along the way. I am grateful for the opportunity to cooperate with 7Waves during my Master's thesis work. The task provided to me has been challenging but, in return, developed me a lot as an engineer. I feel highly confident that the knowledge I have gained will benefit me greatly in my future engineering career.

A special thanks should also be given to Ph.D. candidate Irene Rivera Arreba at the Department of Marine Technology, NTNU. Irene has helped me with problems in the SIMA software and has guided me out of confusion.

I want to thank my friends and fellow students for all the wonderful memories we have made during the last five years. I would also like to thank my boyfriend, Jostein Nordal Lysberg, for his encouragement and for always brightening my days. Finally, I want to thank my parents for always believing in me and supporting me.

Sophie Holme Stokker

Sophie Holme Stokker

Abstract

Floating offshore wind turbines (FOWT) are being developed to expand wind power generation far from the coast and in deep waters. Utilizing the experience of the oil and gas industry in offshore structures, FOWT design can benefit from this expertise. However, due to wear and tear from wind and waves, the high costs associated with offshore wind remain a challenge. Research on fatigue damage is essential to improve FOWT technology by identifying failure modes and advancing simulation tools. This leads to a longer lifespan, increased energy output, improved reliability, and enhanced safety of wind turbines. Despite these challenges, FOWT development holds promising potential for offshore wind as a renewable energy source.

This thesis employs aero-hydro-servo-elastic analysis using the SIMA simulation software to investigate the effects of waves and wind on fatigue damage in FOWT. Simulations are conducted under three scenarios: irregular waves alone, turbulent wind alone, and a combination of irregular waves and turbulent wind. The impact of each contribution to fatigue damage is evaluated using the IEA Wind 15-Megawatt offshore reference wind turbine with the UMaine VolturnUS-S reference platform. Both flexible and rigid body models are employed to represent the floater of the wind turbine. The study is based on environmental conditions from scatter diagrams of wave heights, peak periods, and wind speeds, aiming to explore fatigue damage development on the substructure.

The thesis also covers the underlying theory and principles of FOWT design and dynamics, highlighting the complexity of analyzing semi-submersible wind turbine systems. Factors such as aerodynamics, hydrodynamics, control systems, and structural mechanics make it necessary to do time-domain simulations to capture non-linear effects from environmental loads accurately. Traditional frequency domain methods are inadequate for flexible structures with wind forces.

The flexible model is validated to accurately capture loads and exhibit results considering the flexibility of the floater, as evident from the tower bending eigenfrequency and damping coefficients. Constant wind and decay tests confirm the structure as a representative of the wind turbine.

Fatigue damage analyses focused on wave-only conditions indicate that parked wind turbines experience more damage than operating turbines due to pitch movement variation regulated by the controller. Fatigue damage in the pontoon is significantly lower than in the tower base, attributed to the exponential decrease in wave energy with depth. In wind-only fatigue damage analyses, the damage increases with turbulence intensity and wind velocity. The difference between parked and operating turbines is significant, with enhanced response observed at the tower eigenfrequency and 3P-frequency. The difference between the tower base and the pontoon is relatively small compared to wave-only analyses.

Regarding combined wind and wave analyses of parked turbines, where the blades do not rotate and are feathered, fatigue damage is generally higher for low wind conditions and lower for high wind conditions compared to the summation of separate wind-only and wave-only simulations. However, for operating turbines with rotating blades and a blade pitch angle optimized for maximum power generation, the summation of fatigue damage is generally higher than the combined simulations, indicating force cancellation.

Sammendrag

Flytende havvindturbiner (FOWT) utvikles for å utvide vindkraftproduksjonen til områder langt fra kysten og i dypere farvann. Ved å bruke erfaringen fra olje- og gassindustrien innen offshore-strukturer, kan FOWT-design dra nytte av denne ekspertisen. Imidlertid utgjør slitasje fra vind og bølger og de høye kostnadene knyttet til havvind en utfordring. Forskning på utmattingsskader er avgjørende for å forbedre FOWT-teknologien ved å identifisere sviktmoder og utvikle simuleringsverktøy. Dette fører til en lengre levetid, økt energiproduksjon, forbedret pålitelighet og økt sikkerhet for vindturbiner. Til tross for disse utfordringene har FOWT-utvikling lovende potensial som en fornybar energikilde offshore.

Denne oppgaven bruker aero-hydro-servo-elastisk analyse ved hjelp av SIMA-simuleringsprogramvaren for å undersøke effekten av bølger og vind på utmattingsskader i FOWT. Simuleringer blir utført under tre scenarier: uregelmessige bølger alene, turbulent vind alene og en kombinasjon av uregelmessige bølger og turbulent vind. Effekten av hver bidrag til utmattingsskader blir evaluert ved hjelp av IEA Wind 15-megawatt offshore-referansevindturbinen med UMaine VolturnUS-S referanseplattformen. Både fleksible og stive modeller blir brukt til å representere flyteren til vindturbinen. Undersøkelsene er basert på miljøforhold fra spredningsdiagrammer for bølgehøyder, topp-perioder og vindhastigheter, med mål om å utforske utviklingen av utmattingsskader på underkonstruksjonen.

Oppgaven dekker også den underliggende teorien og prinsippene for FOWT-design og dynamikk, og fremhever kompleksiteten involvert i å analysere halvt nedsenkbare vindturbinsystemer. Faktorer som aerodynamikk, hydrodynamikk, kontrollsystemer og strukturell mekanikk gjør det nødvendig å kjøre simuleringer av tidsdomene for å fange opp ikke-lineære effekter fra miljøbelastninger nøyaktig. Tradisjonelle frekvensdomenemetoder er utilstrekkelige for fleksible strukturer og vindstyrker.

Den fleksible modellen er validert for å nøyaktig fange opp laster og vise resultater med tanke på fleksibiliteten til flyteren, noe som fremgår av tårnets bøyningsegenfrekvens og dempningskoeffisienter. Tester med konstant vind og tester for å identifisere eigenperioder bekrefter strukturen som en representativ vindturbin.

Utmattelsesskadeanalyser fokusert på kun bølgeforhold indikerer at parkerte vindturbiner opplever mer skade sammenlignet med turbiner i drift på grunn av kontrollering av variasjonen av stamp bevegelse. Utmattingsskader i pongtongen er betydelig lavere enn i basen på tårnet, ettersom det er en eksponentiell reduksjon i bølgeenergi med dybden. I analyse av utmattingsskader med hensyn på vind øker skadene med turbulensintensitet og vindhastighet. Forskjellen mellom parkerte og operative turbiner er betydelig, med høyere respons observert ved tårnets egenfrekvens og 3P-frekvens. Forskjellen mellom tårnbasen og pongtongen er relativt liten sammenlignet med bølgeanalyser.

Når det gjelder kombinerte vind- og bølgeanalyser av parkerte turbiner, der bladene ikke roterer og er vinklet for å minimere motstand fra vinden, er utmattingsskadene generelt høyere for lav vind og lavere for høy vind sammenlignet med separate simuleringer for kun vind og kun bølger. Imidlertid, for operative turbiner med roterende blader og et bladvinkel optimalisert for maksimal kraftgenerering, er summert utmattingsskade generelt høyere enn i de kombinerte simuleringene, noe som indikerer kraftkansellering.

List of Symbols

Symbol	Description
Greek symbols	
α_1, α_2	Mass-/ Stiffness proportional coefficient
β	Frequency ratio
ϵ	Phase angle
η	Displacement and surface elevation
λ	Modal damping ratio
ω	Frequency
ϕ	Velocity potential vector
Φ	Eigenvector and velocity potential matrix
ρ	Density
σ_i	Axial stress in i-direction
τ	Shear stress
ζ	Displacement and motion
Latin symbols	
A	Amplitude and area
a, a'	Axial-/ Angular induction factor
C_D	Drag coefficient
C_M	Mass coefficient
C_P	Power coefficient
D	Displacement and Damage value and Diameter
g	Gravitational acceleration
$H(\omega)$	Transfer function
Hs	Significant wave height
I	Second moment of area
Tp	Peak period
U	Kinetic energy
u	Displacement
Uw	Wind velocity
W	Work
A	Added mass matrix
B	Radiation damping matrix
C, $\bar{c}_i$	Hydrodynamic stiffness and Damping matrix/ Generalized damping quantities
K, $\bar{k}_i$	Stiffness matrix/ Generalized stiffness quantities
M, $\bar{m}_i$	Mass matrix/ Generalized mass quantities
Units	
Hz	Hertz [1/s]
m	Meters
N	Newton
Pa	Pascal
s	Seconds
W	Watt
rpm	Rotations per minute

List of Acronyms

Symbol	Description
1DOF	One-degree-of-freedom
1P	Rotation frequency of on blade of the rotor
3P	Blade passing frequency
6DOF	Six-degree-of-freedom
ALS	Accidental limit state
BEMT	Blade element momentum theory
BEM	Boundary element method
COG	Center of gravity
DAF	Dynamic amplification factor
DNV	Det Norske Veritas
FA	Fore-aft
FAST	Fatigue, Aerodynamics, Structures, and Turbulence simulation tool
FD	fatigue damage
FEM	Finite element method
FE	Finite element
FFT	Fast Fourier transform
FLS	Fatigue limit state
FOWT	Floating offshore wind turbine
GDW	Generalized dynamic wake
IEA	International Energy Agency
IEC	International Electrotechnical Commission
NREL	National Renewable Energy Laboratory
NTM	Normal turbulence model
PM	Pierson-Moskowitz wave spectrum
PRVSC	Pitch-Regulated Variable Speed Control
RAO	Response amplitude operator
RNA	Rotor-nacelle assembly
ROSCO	Reference Open Source Controller
SIMA	Simulation Workbench for Marine Applications
SLS	Service limit state
SS	side-side
SWL	Sea water level
TI	Turbulence intensity
TLP	Tension leg platform
TSR	Tip Speed Ratio
ULS	Ultimate limit state
VCB	Vertical center of bouyancy
VCG	Vertical center of gravity
WT	Wind turbine

Table of Contents

List of Figures

List of Tables

Chapter 1

Introduction

This Master's thesis is a research collaboration with 7Waves AS, an independent Norwegian engineering company specializing in naval architecture and marine engineering [24]. The aim of the thesis is to investigate the relative importance of wind and wave loading in the fatigue design of floating support structures. The study examines how these loading conditions affect the durability and long-term performance of the structure. By understanding the role of wind and wave loading in the fatigue design process, the design and optimization of floating support structures can be improved. Section 1.1 clarifies the motivation for the thesis. Section 1.2 introduces the different types of wind turbines. Section 1.3 briefly describes the challenges in designing wind turbines. Section 1.4 presents work relevant to the thesis.

The problem addressed in this thesis was initiated in the fall of 2022, and the background theory is based on the theory presented in the project thesis.

1.1   Motivation

Since the construction of the successful offshore wind farm in Denmark in 1991 [25], the development of wind turbines has achieved remarkable growth. Wind turbine technology has evolved significantly, leading to the establishment of turbine farms that generate substantial amounts of clean electricity. The first offshore wind farm, known as Vindeby [25], began the expansion of wind energy production at sea. Over the years, wind turbines have become more efficient in aerodynamics, materials, and control systems. Offshore wind farms have also grown in scale and capacity. Modern offshore wind farms can consist of hundreds of wind turbines, with some projects producing gigawatts of electricity. The dimensions and capacity of wind turbines have increased significantly, with larger rotor diameters and increased hub elevations.

The wind industry has seen significant growth in recent years, particularly in the area of offshore and floating solutions for use in deep water. These expansions have led to a growing interest in floating wind turbine concepts for use at water depths greater than 100 meters. The innovations have opened up new possibilities for harnessing wind energy in deep water environments and have the potential to considerably expand the use of wind power as a renewable energy source. The demand for sustainable energy alternatives to fossil fuels has driven the expansion of the wind industry. Statistics from the World Wind Energy Association show that the global market for wind turbines reached a capacity of 97.5 GW in 2021, an increase from 92.7 GW in 2020 [26]. This means that the overall capacity of all wind turbines exceeds 840 GW, providing enough power to meet 7% of global demand. The long-term growth trend over the past three decades is illustrated in Figure 1.1. This graphical representation was originally created by Cambridge University in 2011 but remains relevant in the present context.

Currently, the energy costs for floating wind turbines are higher than for bottom-fixed offshore wind turbines. However, the increasing global demand for power makes bottom-fixed offshore wind

turbines insufficient in the long term, making floating offshore wind turbines a viable option. The technology and experience gained from the oil and gas industry can be applied to the development of floating wind turbines, making them a potential solution for meeting the growing demand for renewable energy [27].
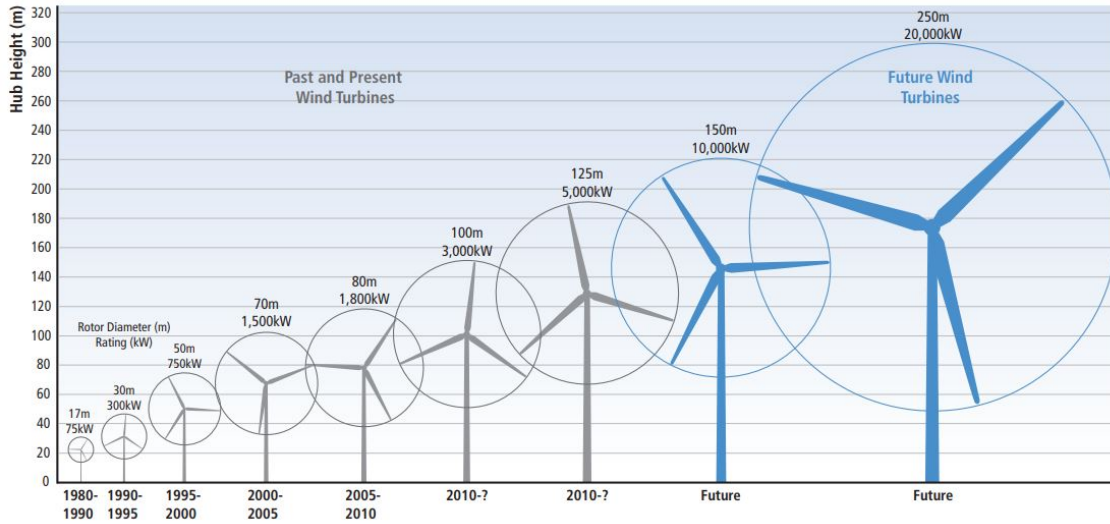
Figure 1.1: Growth in size of typical commercial wind turbines [1]

1.2 Offshore Wind Turbines

As the demand for sustainable energy increases, wind turbines are being relocated from onshore to offshore environments and from bottom-fixed structures to floating offshore wind turbines (FOWT). Currently, most of these offshore wind turbines are developed at transitional water depths. Monopiles are typically used in shallow water, while jackets or tripods are more commonly employed in deeper waters [28]. FOWTs offer several advantages over their onshore and bottom-fixed counterparts. They can produce a higher power level and have a utilization rate of up to 60% compared to 45% - 50% for bottom-fixed offshore wind turbines and 25% - 30% for onshore wind turbines [29].

Four main types of floaters are used for floating offshore wind turbines: spar buoys, semi-submersibles, barges, and tension leg platforms (TLP). Figure 1.2 illustrates the different types of offshore wind turbines. Spar buoys are vertical buoyant cylinders with a center of gravity below sea level. This helps stabilize the wind turbine during operation and allows large rotor movements in response to waves of large amplitudes [30]. Spar buoys have a small water-plane area and a large draft. Semi-submersibles are large-volume structures consisting of multiple columns and pontoons, where the columns provide stability, and the pontoons provide additional buoyancy. They have a medium draft and good stability. TLPs are similar to semi-submersibles, but their mooring systems are vertical tensioned tendons rather than mooring lines. The mooring system contributes to the stability of the TLP. On the contrary, barges have a large water plane area and a small draft [31].

There are two primary types of wind turbines: horizontal axis and vertical axis [32]. Vertical-axis turbines are omnidirectional, which means that they can operate without being adjusted to the wind. Horizontal-axis turbines, on the other hand, operate "upwind" and must be aligned with the wind direction. Horizontal-axis wind turbines are the most commonly used wind turbine, consisting of a rotor with blades attached to a horizontal shaft. The rotor is mounted on a tower, and the blades are inclined to capture the wind and convert its kinetic energy into rotational energy. This rotational energy is transferred to a generator and converted into electricity.

Vertical-axis wind turbines have a rotor with blades attached to a vertical shaft. These turbines can operate in any direction of the wind and are less affected by turbulence, making them suitable for use in urban environments [32]. However, they are typically less efficient than horizontal-axis turbines and are not as commonly used.
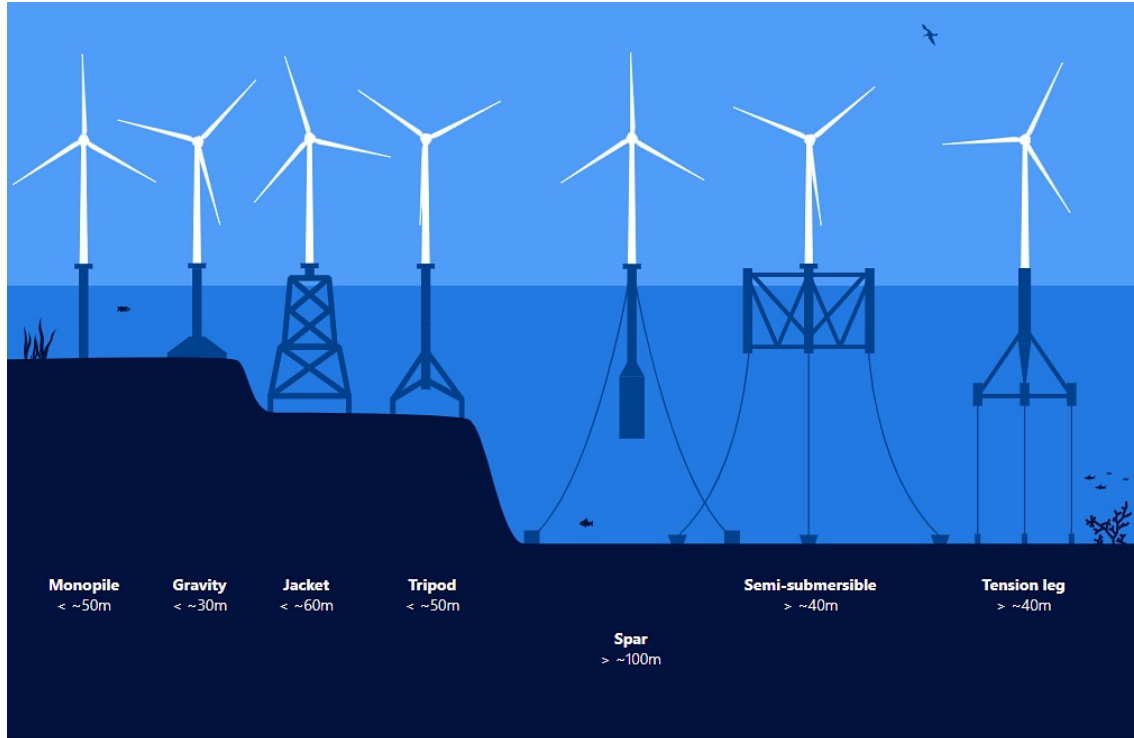
Figure 1.2: Offshore wind foundation types [2].

1.3 Challenges in Designing Offshore Wind Turbines

When designing Floating offshore wind turbine (FOWT), several challenges must be considered, many of which are more complex than those faced by onshore and bottom-fixed offshore wind turbines. These challenges include stability, corrosion, fatigue, erosion, lightning strikes, and biofouling [33]. FOWTs are subjected to more complex coupling effects because of the combined hydrodynamic and aerodynamic loads they experience.

Reducing the cost of FOWTs while ensuring their structural integrity is a key objective in the designing phase. This requires a comprehensive understanding of the various load conditions to which FOWTs are subjected, such as wind, waves, currents, and ice. New design standards for FOWTs also consider the mooring system and the interaction between the floating structures and the wind turbine [12].

In addition to the challenges mentioned above, several others must be considered when designing a FOWT. These include:

- Extreme environmental conditions: FOWTs are exposed to some of the most brutal environmental conditions on earth, including strong winds, large waves, and corrosive saltwater. A significant challenge is developing structures that can withstand these conditions while maintaining structural integrity.

- High installation and maintenance costs: The cost of installing and maintaining a FOWT is typically higher than that of an onshore or bottom-fixed offshore wind turbine. This is due to the additional challenges associated with working in offshore environments, such as needing personnel and specialized equipment.

- Limited knowledge and experience: The technology used in FOWTs is relatively new, and there is still much to learn about their design and operation. This can make it difficult for designers to accurately predict their performance and make design decisions.

- Distance from shore: FOWTs are typically located further from shore than bottom-fixed offshore wind turbines, making it difficult to access them for maintenance and repair.

- Interaction with other ocean users: FOWTs are often located in areas where conflicts with other vessels, such as ships and fishing boats, may arise. Designing a FOWT that minimizes its impact on these users while maintaining its performance is a challenge.

1.4   Relevant Work

Numerous studies have been conducted on the coupled dynamic analysis of Floating offshore wind turbine (FOWT), focusing on various floating foundation types such as spar, TLP, and semi-submersible. Most of these studies employ numerical analysis, with the rigid body modeling approach of the floater being the most commonly used approach.

Hall and Goupee used the numerical tool FAST to analyze coupled wind-wave loads on a semi-submersible FOWT and found that the lumped-mass method was able to capture the dynamic effects of the mooring lines [34]. These results were validated by experimental data from a 1:50-scale model tested by NREL. Couling further validated the results for the aero-hydro-servo-elastic response of a 5 MW wind turbine on the DeepCwind platform [35].

Lee et al. conducted a fatigue study of the hydrodynamic-structure interaction on a FOWT supported by the DeepCwind platform and proposed a deterministic fatigue damage analysis method [36]. Netzband analyzed the platform motions of a 5 MW FOWT with the DeepCwind concept and investigated the influence of blade loads on the structure [37].

Zhang et al. performed a hydrodynamic analysis of three different semi-submersible FOWTs, considering second-order hydrodynamic effects [38]. Their findings showed that these loads can induce resonance in the platform pitch motion, resulting in increased fatigue damage. Similarly, Zhao et al. conducted fully coupled time-domain simulations on 10 MW and 5 MW semi-submersible FOWTs and found that second-order hydrodynamic loads can cause severe resonance at eigen-frequencies, leading to increased fatigue damage, particularly in the 10 MW FOWT [39]. Mei et al. also investigated the effects of second-order hydrodynamic loads on a 15 MW FOWT. They concluded that neglecting these loads can significantly underestimate the accumulation of fatigue damage over 25 years at the base of the tower [40]. These studies underscore the significance of accounting for second-order hydrodynamic loads in the design and analysis of FOWTs.

Haaland explored the feasibility of using a combined method of coupled analysis in Simulation Workbench for Marine Applications (SIMA) and time-domain potential flow analysis in Wasim for load transfer analysis of 10 MW FOWTs [3]. The method was successfully applied to analyze the time and frequency domains in Wasim and Wadam.

Kvittem and Moan conducted fatigue analysis for a wide range of environmental conditions for a semi-submersible FOWT, using a coupled analysis approach that considers hydrodynamic loads and the structural response of the platform. Their study revealed that fatigue damage was sensitive to environmental conditions and structural response, highlighting the importance of considering these factors in the fatigue analysis of FOWTs [41].

Li et al. developed a new approach for modeling flexible floaters in FOWTs [23]. They divided the floater into rigid bodies connected by flexible beams and conducted coupled time-domain simulations. The study emphasizes the importance of considering structural flexibility for accurate predictions of global dynamic responses. The effects of floater flexibility on a 15 MW semi-submersible FOWT were investigated under different wind and wave conditions. Results show that considering floater flexibility reduces the tower bending natural frequency and increases bending moment amplitudes at the tower base, especially in high wind conditions.

1.5 Thesis Outline

The following is the outline of this thesis.

Chapter 2 Provides the theory the thesis is built upon. In this chapter, all necessary background theory is elaborated on.

Chapter 3 Elaborates on the case scenario, including a detailed description of the 15 MW UMaine Volturnus Wind Turbine and the chosen Lifes50+-environment.

Chapter 4 Describes the methodology used throughout the thesis.

Chapter 5 Contains results of analyses to validate the models in SIMA.

Chapter 5.7.4 Contains the results of the fatigue analysis.

Chapter 6 Gives conclusions regarding the results where Section 6.3 also contains suggestions for further work

Chapter 2

Background Theory

This chapter presents the theoretical foundation necessary for understanding the content of this thesis. In Section 2.1, the different conceptual foundations of floating wind turbines are briefly introduced. Section 2.2 explains the main methods for performing global structural dynamic analysis. Section 2.3 describes how wave loads are determined, and Section 2.4 describes how aerodynamic loads are calculated. Section 2.5 briefly introduces wind turbine controller theory. Section 2.6 presents the concept of hydro-aero-servo-elastic coupled analysis. Section 2.7 describes how the sea can be properly represented by means of a statistical description. Section 2.8 and Section 2.9 represent the different limit states and how fatigue is calculated. Finally, Section 2.10 describes the numerical tools available for conducting analysis of floating wind turbines.

2.1 Foundation Concepts for Floating Wind Turbines

The classification of foundations for floating offshore wind turbines can be divided into three main groups, depending on the contributions to the stability [42]:

- **Buoyancy stabilized:** A semi-submerged floating platform that is anchored to the seafloor by mooring lines. The stability is achieved by using the distributed buoyancy and taking advantage of the water-plane area for the righting arm. An example of a buoyancy-stabilized foundation is the WindFloat project [43]. The main advantages of a semi-submersible foundation are the manufacturing being onshore and the platforms being fully equipped. The disadvantage is, among other things, the tendency to higher dynamic wave-induced motions that easily become critical [44].

- **Ballast stabilized:** A cylindrical structure stabilized by ballast, commonly referred to as a spar buoy foundation. The stability is gained from having its center of gravity below the center of buoyancy. An example of such a foundation is the Hywind concept [43]. Spar buoys are a simple design with low installation mooring costs and will typically exhibit reduced dynamic wave-induced motions. However, offshore operations require heavy-lift vessels, and the concept needs water deeper than 100 m [44].

- **Mooring line stabilized:** A structure semi-submerged and anchored to the seabed in a way that it reaches stability by the tension from the mooring lines. Tension leg platforms (TLP) have a shallow draft. Compared with the tension stability TLPs, this is often smaller and lighter than the two foundations mentioned above. However, the design increases stress on the tendon and anchor system [42].

Figure 2.1 illustrates the different design concepts, with a few examples of real-life designs [3]. The figure reveals that commercial designs usually can be classified as one of three main groups, but incorporate features from the two other categories.
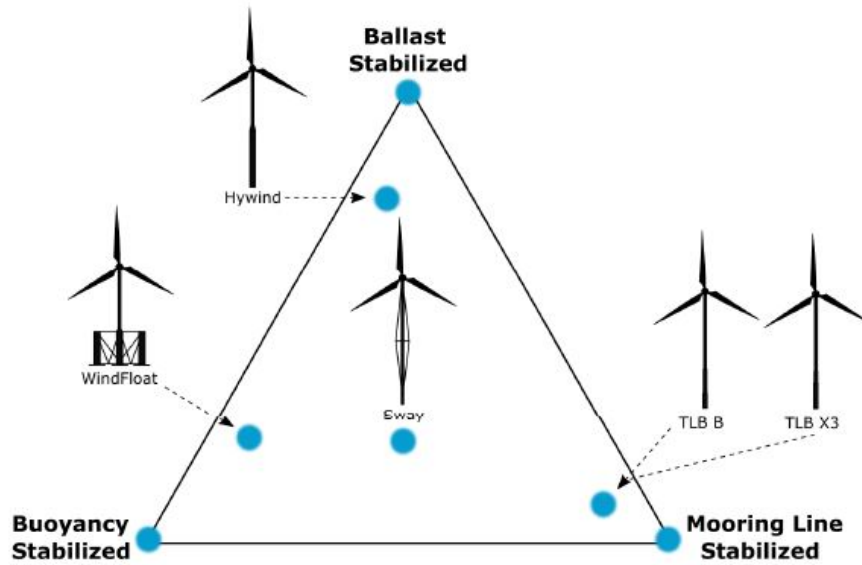
Figure 2.1: Categorization of FOWT foundations [3]

2.1.1 Semi-Submersible Designs

Numerous proposals have been made and implemented for the substructure of 15 MW wind turbines, utilizing semi-submersibles as their foundation. These designs aim to optimize stability, hydrodynamic performance, structural integrity, and cost-effectiveness. The popularity of the semi-submersible as a wind turbine foundation grew after the introduction of the WindFloat concept in 2009 [16]. The typical design features a three-column semi-submersible, with the tower mounted on one of the columns. The columns are connected by pontoons, which are reinforced with braces for added structural strength. Additionally, heave plates are incorporated to increase the heave period of the wind turbine [45, 46, 47]. During that phase of wind turbine development, the Wind-Float project installed a 2 MW turbine. However, due to the rising demand for power, the current market envisions the development of even larger wind turbines, with capacities reaching up to 15 MW and beyond. A notable example is the WindFloat Atlantic project, which employs 8.4 MW turbines with an upscaled design for the floating platform [48].

Another design example is the GustoMSc Tri-Floater or Dutch Tri-Floater, which is designed to be upscaled for larger wind turbines. With a displacement of 14,000 tons, it can support a 15 MW wind turbine [49]. The design consists of three columns with additional horizontal ring webs and heave plates [50]. In contrast to the WindFloat design, the Tri-Floater centers the weight of the tower and wind turbine. A similar design to the Tri-Floater is the UMaine VolturnUS-S platform, which is designed to support the 15 MW reference turbine by NREL [4]. Like the Tri-Floater, it centers the weight of the tower and wind turbine but is also placed on top of a center column.

Lastly, a V-shaped semi-submersible design was introduced in the WINFLO project [51]. The WINFLO floater is designed as a lightweight semi-submersible, symmetrical in the x-direction. Positioned along the central vertical axis, the tower is supported by three columns, which both enhance the hydrostatic stiffness and stability and restrict the displacement of the floater. The three discussed semi-submersible designs are illustrated in Figure 2.2.

(a) WindFloat design [50]

(b) Dutch Tri-Floater design [50]

(c) WINFLO V-shaped design [38]
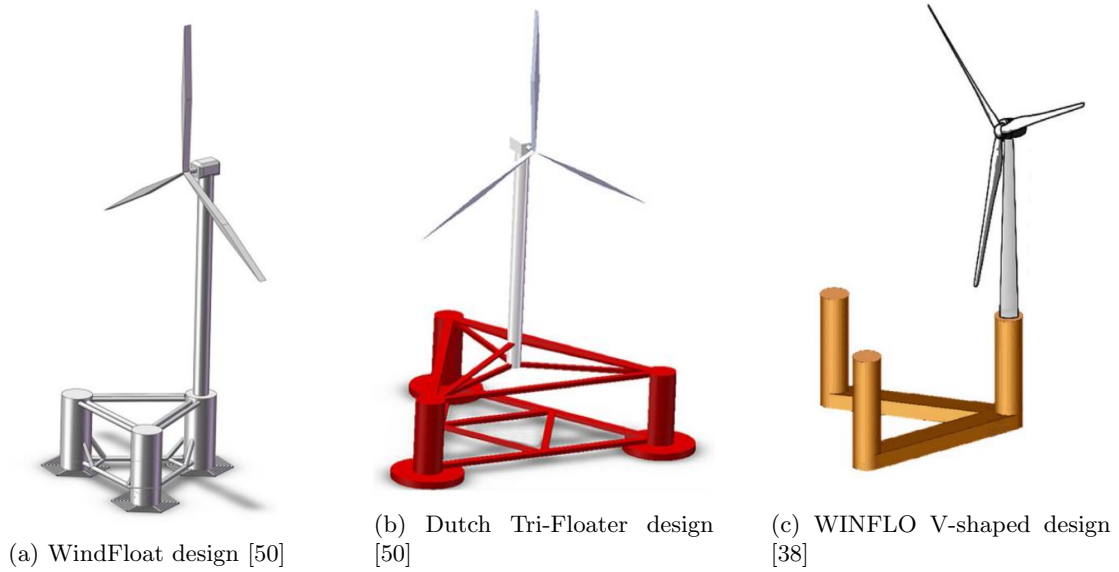
Figure 2.2: Commercial semi-submersible designs

2.2 Structural Mechanics

Several methods exist for performing global structural dynamic analysis of a floating structure. These methods include the linear rigid body approach, modal method, nonlinear beam models, and more detailed finite element models considering 2D or 3D shell elements.

2.2.1 Rigid Body Mechanics

A rigid floating body can be defined by three global translation degrees of freedom (DOFs) and three global rotational DOFs, and is a body where no segments move relative to each other. The DOFs are referred to as surge, sway, heave, roll, pitch, and yaw and are expressed with a motion vector in Equation 2.1 [12]. A structure cannot be infinitely stiff, and the assumption that a structure is a rigid body is more of an idealization. However, it is a good approximation in many cases.

$$\vec{\eta} = [\zeta_1(t), \zeta_2(t), ..., \zeta_6(t)]^T \tag{2.1}$$

If the six rigid body motions are known, the position on every point of a rigid body is also known. In the case of small motions, the motion of a point s can be expressed as in Equation 2.2, where '$\times$' denotes the vector cross-product [3]. When the motion is obtained, $x, y,$ and z are the coordinates of the point.

$$\mathbf{s}(x, y, z) = [\zeta_1 \quad \zeta_2 \quad \zeta_3] + [\zeta_4 \quad \zeta_5 \quad \zeta_6] \times [x \quad y \quad z] \tag{2.2}$$

Figure 2.3 illustrates the global coordinate system used throughout the thesis for the FOWT and the corresponding DOFs. The total mass of the structural system consists of the hydrodynamic added mass and the structural mass, and there is hydrodynamic, aerodynamic, and damping present [52]. The governing dynamic equilibrium can be expressed by a system of differential equations as in Equation 2.3, originating from Newton's second law [12]. Here, $\vec{F}$ is a time-dependent vector consisting of the external excitation forces acting on the structure for all modes of motion. $\mathbf{M}$ is the matrix for the dry mass of the structural, while $\mathbf{A}$ is the matrix containing the added mass, meaning the component due to the external fluid that opposes the body acceleration.
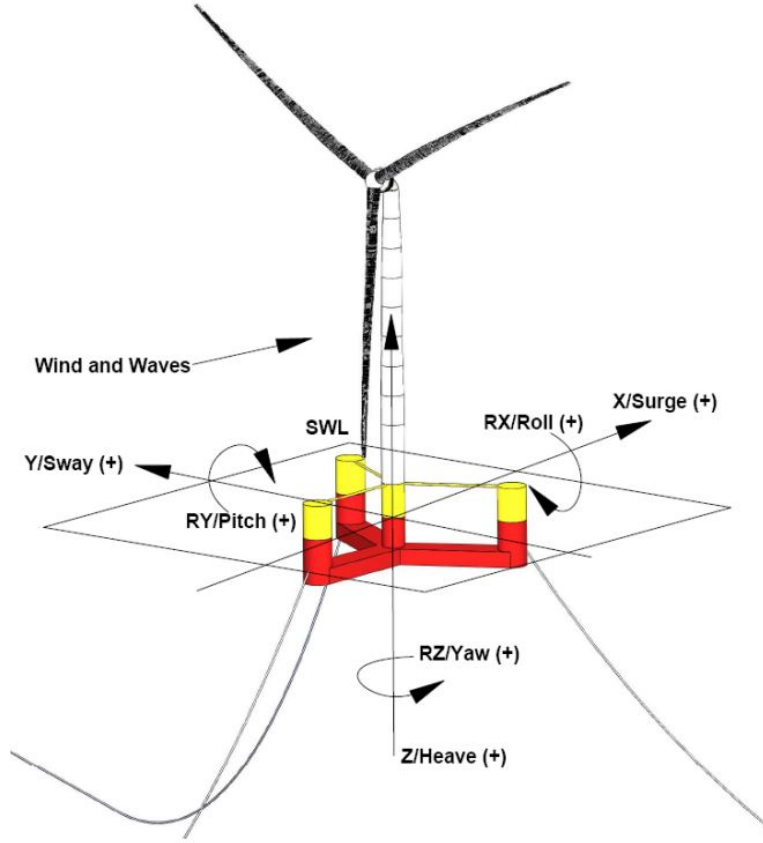
Figure 2.3: Coordinate system of reference wind turbine [4].

B is the damping matrix of the structure and is proportional to the velocity vector of the body. **C** contains the hydrostatic restoring terms of the structure, while **K** contains the restoring effects of the mooring system. While $\vec{F}$ is a 6-1 vector, **M, A, B, C** and **K** are 6-by-6 matrices. Equation 2.3 gives a linear description of the system, and including non-linear effects would require additional terms in this equation.

$$[\mathbf{M} + \mathbf{A}]\ddot{\vec{\zeta}} + \mathbf{B}\dot{\vec{\zeta}} + [\mathbf{C} + \mathbf{K}]\vec{\zeta} = \vec{F} \tag{2.3}$$

According to Faltinsen [5], it is convenient to consider the frequency domain for a linear wave-only analysis for a floating body. The body response (and wave excitation at one frequency) can be assumed harmonic by neglecting nonlinear wave excitation terms. The regular wave excitation can be rewritten to Equation 2.4 for a given frequency. Here, the symbol $\tilde{F}$ denotes a complex-valued force vector.

$$\vec{F}(\omega) = \Re(\tilde{\vec{F}}e^{-i\omega t}) \tag{2.4}$$

Equation 2.3 can then be rewritten to the frequency domain, as in Equation 2.5 [5].

$$(-\omega^2[\mathbf{M} + \mathbf{A}(\omega)] + i\omega\mathbf{B}(\omega) + [\mathbf{C} + \mathbf{K}])\tilde{\vec{\zeta}} = \vec{F}(\omega) \tag{2.5}$$

The frequency domain response is a good approach for capturing important responses. However, for a floating wind turbine, there is a necessary modification to be done in order to include the loads and damping induced by the wind and second-order wave forces [12]. In general, to solve the equation of motion in the time domain, it is necessary to include non-linear load effects. The frequency dependence can be included through a convolution integral or a state-space representation of the time-dependent coefficients. In SIMO, explained further in Section 4.4, the convolution integral approach is implemented [13], in Equation 2.6.

$$(\mathbf{M} + \mathbf{A}^\infty)\vec{\ddot{x}}(t) + \int_0^t \kappa(t-\tau)\vec{\dot{x}}(\tau)d\tau + \mathbf{C}\vec{x}(t) = \vec{F}(t) \tag{2.6}$$

2.2.2 Modal Analysis

Modal analysis is a powerful technique commonly used to study the dynamic behavior of wind turbine structures. This method involves solving the equation of motion for a structure and determining a set of mode shapes that represent its time-varying deformations [12]. Modal analysis can help identify critical modes of vibration that may cause structural damage or fatigue, making it an essential tool in wind turbine design. The theory is based on the equilibrium equation for the system, which gives the eigenvalue problem in Equation 2.7. Here, $\mathbf{K}$ is the stiffness matrix, $\mathbf{M}$ is the mass matrix, ω is the eigenfrequency, and Φ is the eigenvector [11].

$$(\mathbf{K} - \omega^2 \mathbf{M})\mathbf{\Phi} = 0 \tag{2.7}$$

Additionally, for the free undamped vibration, the damping matrix $\mathbf{C}$ is equal to zero. Combining this and Equation 2.7, Rayleigh damping, also known as proportional damping, can be introduced. This takes the basis that the damping can be expressed linearly of the mass and stiffness matrices, as in Equation 2.8. Here, the α_1 and α_2 are the mass- and stiffness-proportional coefficients, respectively. Due to orthogonality, the generalized quantities can be written as in Equation 2.9 [11]. As long as the coefficient α_1 and α_2 are global coefficients, the orthogonal structural damping matrix is obtained.

$$\mathbf{C} = \alpha_1 \mathbf{M} + \alpha_2 \mathbf{K} \tag{2.8}$$

$$\bar{c}_i = \alpha_1 \bar{m}_i + \alpha_2 \bar{k}_i \tag{2.9}$$

However, modal analysis has limitations. This method may not account for the non-linear effects that can occur in certain operating conditions, such as high winds or extreme gusts. As a result, it may be necessary to use other time-domain simulations, to complement the modal analysis results. Additionally, accurate pre-processing of the system modes is crucial for obtaining reliable results from the modal analysis. Any errors or approximations in the pre-processing can affect the accuracy of the mode shapes and eigenvalues, leading to incorrect predictions of the dynamic behavior of the wind turbine.

Therefore, while modal analysis is a useful tool in wind turbine design, it should be used in conjunction with other analysis methods and with careful attention to the accuracy of pre-processing [12]. In this regard, FAST software is commonly used for the modal analysis of wind turbines, as it is based on the formulation of modal dynamics and multibody dynamics [53].

2.2.3 Non-linear Finite Element Formulation

The finite element method (FEM) is a numerical method that subdivides a structure into smaller elements and approximates the solution of differential equations for displacements using a reduced number of displacement patterns [13]. Nonlinear FEM is a solution method considering large displacement effects related to nonlinear boundary conditions or material behavior. In wind turbine modeling, non-linearities related to geometric structural non-linearities are also considered in the non-linear FEM. This includes the effects of large displacements and quadratic load formulations in drag and thrust forces. By using beam, shell, or solid elements and solving the equation of motion stepwise, dynamic effects can be captured [12].

In non-linear FEM, the non-linear equation for dynamic equilibrium of a system of finite elements is expressed in Equation 2.10. This equation requires the virtual work of inertial, dissipative, and internal forces to equal the externally applied loads. The equation is expressed by global matrices that contain the properties of the mass ($\mathbf{M_g}$), damping ($\mathbf{B_g}$), and stiffness ($R^{\vec{int}} = \mathbf{K}_g\vec{D}$) features

of the finite elements. $\vec{D}$ is the displacement vector of the system. The external forces include weight, buoyancy, forced displacements, viscous drag, and wave acceleration terms [13].

$$\mathbf{M}_g \vec{\ddot{D}} + \mathbf{B_g} \vec{\dot{D}} + \vec{R}^{int} = \vec{R}^{ext} \qquad (2.10)$$

Compared to modal analysis, nonlinear FEM captures higher structural modes without requiring the pre-processing that modal analysis requires. However, using non-linear beam elements in FEM can be less computationally efficient. RIFLEX, a structural FEM solver, is commonly used for wind turbine modeling as it employs beam element theory and allows for large rotational deformations. RIFLEX is a part of the computational software SIMA used in this thesis, which includes a range of other analysis methods that can be used in conjunction with FEM for a more comprehensive understanding of wind turbine behavior.

2.2.3.1 Decay Tests

A decay test is a widely used technique for analyzing the natural frequencies and damping characteristics of a structure. This test involves exciting the structure with an impulse force that induces free-body motion. The impulse force is removed, and the response of the structure is measured, characterized by its decay over time. A complete finite element model is used for the time domain simulation. The measured decay data is then fitted to a mathematical model to determine the structure's natural frequencies. The natural frequencies obtained from the decay test can be used to understand the vibrational behavior of the structure and design it for optimal performance.

The decay test can also be used to estimate the damping forces that act on the structure, which is essential to assess its damping characteristics. The damping forces include radiation and viscous components. By assuming uncoupled motions, the decay of the oscillations can be described using a mathematical model. PQ analysis can then be performed to determine the damping coefficient of the structure. The decay of any degree of freedom can be expressed as shown in Equation 2.11, where η represents the displacement, $\omega_0 = \sqrt{k/m}$ represents the natural frequency, and b_1 and b_2 represent the damping coefficients.

$$\ddot{\eta} + b_1 \dot{\eta} + b_2 |\dot{\eta}|\dot{\eta} + \omega_0^2 \eta = 0 \qquad (2.11)$$

After the impulse is removed, the damping force oscillates the structure in the direction of the applied force. The kinetic energy is expressed as in Equation 2.12, and the work done by the damping force can be expressed as in Equation 2.13 [54]. The motion and velocity are respectively expressed $x = \bar{x}_i \cos(\omega t + \epsilon)$ and $\dot{x} = -\omega \bar{x}_i \sin(\omega t + \epsilon)$.

$$\Delta U_i = \frac{1}{2}kx_i^2 - \frac{1}{2}kx_{i+1}^2 = \frac{1}{2}k(x_i + x_{i+1})(x_i + x_{i+1}) = k(\bar{x}_i)(x_i - x_{i+1}) \qquad (2.12)$$

$$W_i = \int_{t_i}^{t_{i+1}} (b_1\dot{x} + b_2|\dot{x}|\dot{x})\dot{x}dt \qquad (2.13)$$

The kinetic energy loss is found to be equal to the work done by the damping forces and can be written as in Equation 2.14. It is apparent that P represents the linear, viscous damping coefficient, and Q represents the quadratic, radiation damping coefficient.

$$\frac{x_i - x_{i+1}}{\bar{x}_i} = \frac{\omega\pi}{k}b_1 = \frac{8\omega^2}{3k}b_2\bar{x}_i = P + Q\bar{x}_i \qquad (2.14)$$

2.2.4 Reduction of Degrees of Freedom

The mathematical formulation of a structural problem using element discretization may involve thousands or even millions of independent degrees of freedom (DOFs). Reducing the number of DOFs has significant advantages, especially with respect to time consumption. The need for an accurate stress analysis determines primarily the number of DOFs. There are several methods to reduce the number of DOFs [11]:

- **Static condensation**: Static condensation involves solving the eigenvalue problem and neglecting the rotational mass. This allows for the mass and stiffness matrices to be divided into static and dynamic DOFs, reducing the number of DOFs required for the analysis. This method is useful when the number of DOFs is large and only a few modes are needed for the analysis.

- **Rayleigh-Ritz condensation**: Rayleigh-Ritz condensation is suitable for cases when only a few modes are needed and applies to the general dynamic equilibrium equation. This method involves approximating the solution using a set of basis functions and minimizing the residual error.

- **Master-Slave method**: The Master-Slave method divides the nodes into masters and slaves, with slaves following their masters statically. If a DOF's natural frequency, $\omega^2 = K_{ii}/M_{ii}$, is large, it is considered a good candidate for being a slave. This method is useful when there are large differences in natural frequencies between DOFs.

- **Sub-structuring technique**: Sub-structuring involves dividing the nodes into internal and external nodes, with the internal nodes following the external nodes either statically or dynamically. This method rearranges the order in which the equation is solved rather than approximating the solution. It is useful for complex structures with many internal and external nodes.

2.3 Wave Loads

The floating structure of a floating offshore wind turbine (FOWT) can typically be divided into two categories: slender structures and large-volume structures. Examples of slender structures include spar buoys, where Morison's equation is applicable. Examples of large-volume structures include tension leg platforms (TLPs) and semi-submersibles, where diffraction and radiation effects can significantly impact the structure. In this thesis, the focus is on semi-submersible FOWTs, which are considered large-volume structures. The following sections will provide an overview of the relevant theory of wave loads.

2.3.1 Hydrostatic Loads

The hydrostatic wave load on a submerged structure arises from the hydrostatic pressure of the fluid at rest, which depends solely on the vertical coordinate. For an incompressible fluid with a positive direction in the upward z-axis, the pressure is described by Equation 2.15, where ρ is the density of seawater and g is the gravitational acceleration.

$$\frac{dp}{dz} = -\rho g \tag{2.15}$$

In considering the structure as a rigid body, the hydrostatic stiffness depends solely on the geometry of the waterline. Thus, the non-zero terms of the hydrostatic stiffness matrix can be determined using the center of buoyancy (z_B) and the center of gravity (z_G) [12] of a body with x, z geometry and area in the waterplane $A_{waterplane}$. Equations 2.16 - 2.19 illustrate how these centers relate to the nonzero terms of the hydrostatic stiffness matrix.

$$C_{33} = \rho g A_{waterplane} \tag{2.16}$$

$$C_{35} = C_{53} = -\rho g \int \int_{A_{waterplane}} x dx dy \tag{2.17}$$

$$C_{44} = \rho g \nabla z_B - M g z_G + \int \int_{A_{waterplane}} y^2 dx dy \tag{2.18}$$

$$C_{55} = \rho g \nabla z_B - M g z_G + \int \int_{A_{waterplane}} x^2 dx dy \tag{2.19}$$

It is important to note that considering a structure as a rigid body assumes that the structure does not deform under hydrostatic load. In contrast, a flexible floating body would experience deformation and a change in the geometry of its waterline.

2.3.2 Potential Flow Theory

First-order potential flow, also known as linear wave theory, is a widely used method to predict wave loads on marine structures [5]. However, for structures with natural frequencies outside the wave excitation range, non-linearities can arise, leading to ringing loads and responses [12]. Potential flow theory assumes that the fluid is incompressible and that the continuity of flow is preserved. In this theory, the flow velocity is defined as the gradient of a scalar function called the velocity potential, denoted by ϕ. The velocity potential Φ expressed in Equation 2.20 can describe the fluid velocity vector in Equation 2.21 [5].

$$\Phi^{(1)}(x, t) = \sum_j \phi_j^{(1)}(x) e^{i\omega_j t} \tag{2.20}$$

$$\mathbf{V} = \mathbf{i}\frac{\partial \Phi}{\partial x} + \mathbf{j}\frac{\partial \Phi}{\partial y} + \mathbf{k}\frac{\partial \Phi}{\partial z} = \mathbf{i}u + \mathbf{j}v + \mathbf{k}w \tag{2.21}$$

The Bernoulli equation, as shown in Equation 2.22, is a fundamental equation of fluid mechanics that describes the total pressure of the fluid relative to the atmospheric pressure. In this equation, ρ is the fluid density, g is the gravitational acceleration, and ∇ is the vector differential operator. The pressure consists of linear dynamic, quadratic, and hydrostatic. By expressing the pressure as a function of the velocity potential, only one unknown parameter, ϕ, needs to be considered instead of the three velocity variables u, v, w, and the pressure variable p. The last term in the equation is the same as the hydrostatic pressure term in Equation 2.15.

$$p - p_a = -\rho \left(\frac{\partial \phi}{\partial t} + \frac{1}{2}|\nabla \phi|^2 + gz \right) \tag{2.22}$$

To fully describe the velocity field of a fluid using a velocity potential, two additional assumptions must be made: the flow is irrotational, and the fluid is inviscid [5]. An irrotational flow has no net rotation, which allows the velocity field to be described by a single scalar function. Inviscid fluids have no internal friction or viscosity, making it easier to analyze fluid flow without considering the effects of viscosity. However, most real-world fluids have some level of viscosity, which cannot be ignored in practical applications.

Due to incompressible, inviscid, and rotational flow, second-order potential flow theory is important to consider for structures with natural frequencies outside the wave excitation range. The interaction between two waves with frequencies ω_j and ω_k can result in excitation at frequencies outside

the wave excitation range, and second-order potential includes sum frequency (ϕ_{jk}^{+}) and difference frequency (ϕ_{jk}^{-}) components [55, 5]. The second order potential is defined as in Equation 2.23.

$$\Phi^{(2)}(x,t) = \Re \sum_{j} \sum_{k} [\phi_{jk}^{+}(x)e^{i(\omega_j+\omega_k)t} + \phi_{jk}^{-}(x)e^{i(\omega_j-\omega_k)t}] \qquad (2.23)$$

2.3.3   Panel Methods

The panel method, also known as the boundary element method (BEM), is a typically used technique for analyzing the linear steady-state response of large-volume structures. It is based on potential theory and is applied to the study of surface waves. Several panel methods exist, such as distributing sources and sinks over the mean wetted body surface or distributing a mix of sources, sinks, and normal dipoles over the wetted body surface [5].

The paneling of the hull surface involves using quadrilateral or triangular elements in three-dimensional problems. In these methods, the three-dimensional Laplace equation governing the fluid volume is transformed into a surface integral equation over the boundaries of the solution domain, using Green's theorem. This integral equation is then solved by dividing the submerged part of the structure into smaller elements.

Each of these elements represents distributed sources or sinks and must satisfy the Laplace equation. For each element, the individual velocity potential is determined, and the total velocity potential is obtained by the superposition of these individual contributions. Common practice is that the length of the elements should be smaller than 1/8 of the wavelength. Also, for vertical columns with circular cross-sections, it is suggested to have 15-20 circumferential elements at any given height [5].

However, it is important to mention that panel methods assume small oscillation amplitudes of the fluid and the body relative to the cross-sectional dimensions of the body, neglecting flow separation. This means that the methods predict damping due to the radiation of surface waves and do not adequately predict the rolling motion of ships near roll resonance periods, where wave radiation damping moments may be small, and viscous damping effects due to flow separation become significant.

2.3.4   Morison's Equation

The Morison equation, developed by Morison, O'Brien, Johnson, and Shaaf, describes horizontal forces acting on a vertical pile that extends from the bottom through the free surface [56]. It is often used for slender systems where the diameter D is small compared to the wavelength λ [12]. A modified Morison equation for a structure free to oscillate can be written as in Equation 2.24. The horizontal fluid velocity and acceleration are expressed as u and $\dot{u}$. U is the velocity of the current, C_M and C_D are the empirical mass and drag coefficient, D is the diameter of the cylinder, ρ is the density of seawater and η is the movement of the body.

$$dF = \frac{1}{2}\rho C_D D dz(u \pm U - \dot{\eta})|u \pm U - \dot{\eta}| + \rho C_M \frac{\pi D^2}{4}\dot{u} - \rho(C_M - 1)\frac{\pi D^2}{4}dz\ddot{\eta} \qquad (2.24)$$

The first term in Equation 2.24 represents the viscous term, the second represents the Froude-Krylov term, and the final term contains the added mass contributions [12]. The first term is said to be the drag load, F_D, while the other two terms represent the inertial loads, F_I. The potential flow theory covers the internal loads but not the drag term. The deep water limit of linear wave theory states that the water particle acceleration is given as in Equation 2.25.

$$\dot{u} = \omega^2 \zeta e^{kz} cos(\omega t - kx) \qquad (2.25)$$

The Morison equation is not restricted to circular structures and can be used for slender structures with different cross sections. C_M and C_D are different for different cross sections and are a function of, for example, surface roughness and Reynolds number. The wave loads acting on a structure can be categorized with respect to the diameter of the structure D and wave height H on the wavelength λ. This is illustrated in Figure 2.4.
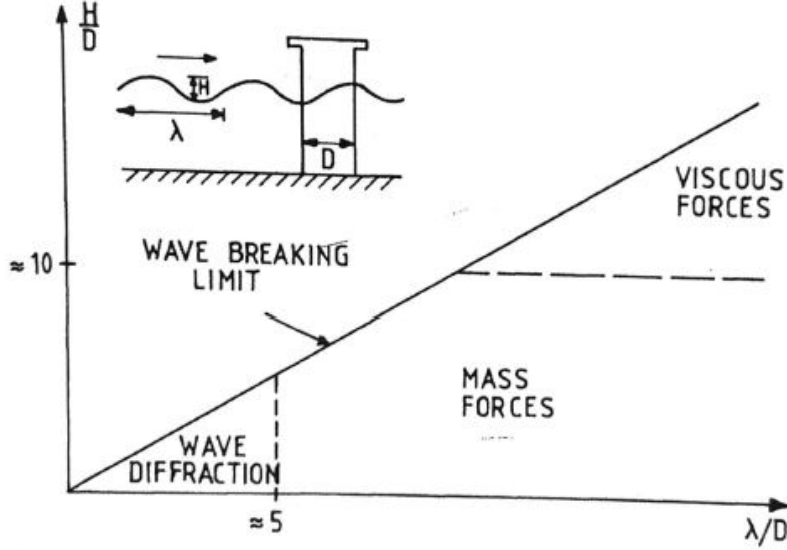
Figure 2.4: The importance of mass, viscous drag and diffraction forces on structures [5]

2.3.5   Hydrodynamic Loads

Wave loads on floating structures are calculated using linear potential theory [5], which is divided into two sub-problems: the diffraction problem and the radiation problem. In the diffraction problem, the forces and moments of the structure are calculated when it is fixed and cannot oscillate with the incoming waves. These loads include Froude-Krylov and diffraction forces and moments. The radiation problem involves calculating the forces and moments of the structure when it is forced to oscillate with the wave excitation frequency. These loads include added mass, damping, and restoring terms. The velocity potential can be divided into the diffraction and radiation problems, as shown in Equation 2.26. Viscous effects on structural members are typically modeled as a drag force.

$$\phi = \phi_D + \phi_R \tag{2.26}$$

The frequency-dependent wave excitation is found from the diffraction problem, while the frequency-dependent added mass and linear radiation are found from the radiation problem. Hydrodynamic forces and moments are obtained by integrating the pressure over the wetted body surface.

The added mass, damping, and restoring loads are the result of the radiation problem. The radiation velocity potential can be expressed as a sum of the velocity potential for the rigid body motion k^{th}, as shown in Equation 2.27.

$$\phi_R = \sum_{j=1}^{6} \phi_k \tag{2.27}$$

The added mass is proportional to the acceleration, the damping to the velocity, and the restoring loads to the displacement. This leads to the total radiation load being expressed as in Equation 2.28, where the load is expressed in the k direction for the kth degree of freedom.

$$F_{rad,k}^{(1)} = -\int_{S_{OB}} \rho \frac{\partial \Phi_R}{\partial t} n_k dS = \sum_{j=1}^{6} -(A_{k,j}\ddot{\eta}_j + B_{k,j}\dot{\eta}_j) \tag{2.28}$$

The diffraction problem can be divided into two sub-problems: the incident wave problem (Φ_0) and the scattered wave field due to the body's presence (Φ). The wave excitation force becomes as in Equation 2.29. Here, the S_{OB} is the wetter surface area of the structure.

$$F_{diff,k}^{(1)} = -\int_{S_{OB}} \rho \frac{\partial \Phi_0}{\partial t} n_k dS - \int_{S_{OB}} \rho \frac{\partial \Phi_D}{\partial t} n_k dS \tag{2.29}$$

The diffraction due to incident wave is assumed to be divided further into two parts, the first-order and the second-order [39]. The first-order wave-excitation forces oscillate with the wave frequencies and can be expressed as in Equation 2.30. Here, A_j is the complex wave amplitude with the corresponding frequency ω_j and direction β_j, $X^{(1)}$ si the normalized wave-excitation force and $e^{i\omega_j t}$ is the harmonic exponential.

$$F^{(1)}(t) = \Re \sum_{j}^{N} A_j X^{(1)}(\omega_j, \beta_j) e^{i\omega_j t} \tag{2.30}$$

Second-order hydrodynamic loads are found to be proportional to the square of the wave amplitude, and the frequencies are equal to the sum and differences in wave frequencies. These wave exciting forces can be divided into the mean drift force, difference-frequency wave drift force, and sum-frequency wave force. [38]. The second-order wave loading can be expressed as in Equation 2.31 [39]. Here, the $D(\omega_j\omega_k)$ and $S(\omega_j\omega_k)$ are the difference- and sum-frequency QTFs.

$$F^{(2)}(t) = \Re \left[\sum_{j}^{N} \sum_{i}^{N} A_j A_k^* D(\omega_j\omega_k) e^{i(\omega_j - \omega_k)t} + \sum_{j}^{N} \sum_{i}^{N} A_j A_k^* S(\omega_j\omega_k) e^{i(\omega_j - \omega_k)t} \right] \tag{2.31}$$

2.4 Aerodynamic Loads

The power production from a wind turbine depends mainly on the interaction between the rotor and the wind. The wind is considered a combination of mean wind and turbulent fluctuations in mean flow. Experience has shown that the source of fatigue loads is the periodic aerodynamic forces caused by wind shear, off-axis winds, rotor rotation, and fluctuating forces induced by turbulence and dynamic effects [57]. This means that the aerodynamic forces acting on the wind turbine contribute to the global dynamic response. The rotor thrust and torque are found by integrating the lift and drag forces acting on the airfoil cross-section. The thrust force causes the pitch and surge motion on the structure, while the torque force causes small roll motions and is the force that actually drives the rotor to spin [57]. The rotational frequencies of the wind turbines are an important aspect of the design of the wind turbine and the spectrum analysis. This includes the rotation frequency of the rotor and the blade passing frequency for a three-blade horizontal axis. This is commonly known as the 1P and 3P frequency, ad it is important to design the natural frequencies of the FOWT outside these frequencies [12].

There are several different methods for computing the aerodynamic loads on a wind turbine. The simplest model is the one-dimensional momentum balance for an ideal rotor, while one of the more computationally expensive ones is a three-dimensional Navier-Stokes solution. In SIMA, the blade element momentum (BEMT) model is used to model aerodynamic loads [58]. Another widely used model is the generalized dynamic wake (GDW) method. The following describes these methods for computing the aerodynamic loads on a wind turbine.

2.4.1 Blade Element Momentum Theory

This thesis calculates the aerodynamic loads with the blade element momentum (BEMT) method. This method combines the theory of momentum for the ideal turbine with wake rotation and airfoil theory. The dynamic inflow is the time delay on changes in induced velocity related to the time it takes to convert vorticity in the wake downstream, away from the rotor. Including the BEMT method in SIMA will give the correct time series of blade and rotor loads when the blade pitch angle, wind speed and direction, and tower motion change[58].
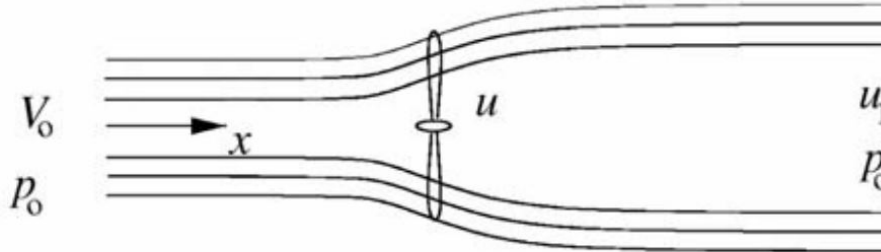
Figure 2.5: One-dimensional actuator disk rotor model [6].

The momentum theory for the ideal turbine models the wind field as a stream tube. The thrust and torque contributions are integrated over the turbine rotor area as small elements. Observing the contributions of an ideal rotor turbine, they are determined by the one-dimensional actuator disk model. Using the ideal rotor turbine, the flow is assumed to be homogeneous, incompressible, and steady state. The flow does not cross the stream tube boundaries, leading to two control volumes; from the inlet to the left side of the rotor disk and from the right side of the rotor disk to the outlet. How the flow acts around the rotor is illustrated in Figure 2.5. An axial induction factor (a) must be introduced, expressing the fractional decrease in wind velocity between the free stream and the turbine rotor.

In reality, the torque exerted by the wind turbine blades causes the flow to rotate. An angular induction factor (a') must also be considered. As the airflow passes over the airfoil, there is a pressure difference between the lower and upper surfaces, which produces a lift force [59]. This pressure difference also generates a drag force. These effects are illustrated in Figure 2.6. By solving the conservation equations of momentum and mass and applying the Bernoulli equation, the equation for power can be derived [59]. However, the actual power extracted from a wind turbine is less than the Betz limit [57], due to factors such as wake rotation, a finite number of blades, non-zero drag, and mechanical and electrical losses. When the tip speed ratio is included in the maximum power coefficient of an ideal turbine, the effect of wake rotation is taken into account.

In the BEMT model, the wind flow is modeled as a stream tube that is divided into annular elements. This model combines the ideal turbine with the wake and the blade elements, as described above. It assumes that the force of the blades on the flow is constant in each element, which is only true if there are infinite blades. In order to obtain accurate results, corrections must be made to account for the idealizations of the momentum theory.

The corrections used in SIMA are listed below [3]:

- Prandtl correction - Corrects the assumption of an infinite number of blades in the idealized momentum theory.

- Glaubert correction - Corrects large induction factors when the momentum theory no longer applies. Empirical relations are used to match measurements.

- Dynamic wake - Takes into account the time it takes for the induced velocities to balance aerodynamic loads when the wind speed changes.

- Dynamic stall - Takes into account sudden attachment and detachment of the flow.

- Skewed inflow - Takes into account a rotor tilt or yaw angle between the rotor and incoming wind.
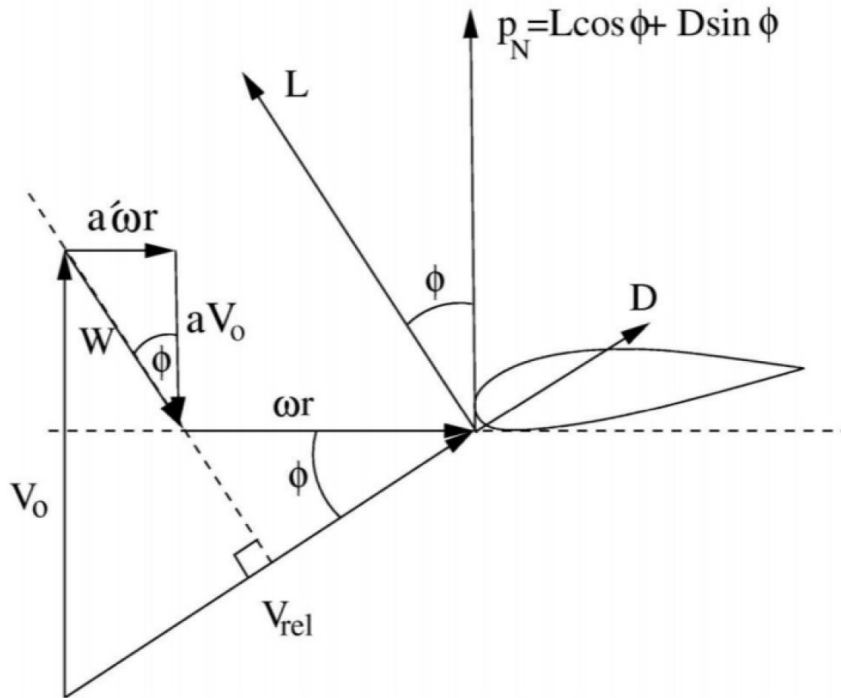
Figure 2.6: Velocity triangle of blade cross-section [6]

2.4.2   Generalized Dynamic Wake Model

The Generalized Dynamic Wake (GDW) model is a computational method to predict aerodynamic loads on a wind turbine. It uses the solution of the Laplace equation based on potential flow theory to obtain the pressure distribution in the rotor plane [12]. The GDW model incorporates dynamic wake effects, skewed wake aerodynamics, and tip loss, which the Blade Element Momentum (BEMT) model does not consider. The boundary conditions for the solution require that the pressure loading on the rotor blades returns to the ambient pressure far from the rotor and that the pressure discontinuity is equal to the thrust. Velocity and pressure are solved as infinite series of Legendre functions and trigonometric functions [12].

One advantage of the GDW model is that it can capture the unsteady wake interactions between the blades, which can significantly affect the aerodynamic loads. However, the model has limitations and is only valid for lightly loaded rotors, as it assumes that the induced velocity is small relative to the mean flow. As a result, the GDW model becomes unstable at low wind speeds. Therefore, it is essential to use caution when using the GDW model and to ensure that it is applied to the correct conditions for accurate predictions of aerodynamic loads on wind turbines [12].

2.4.3   Unsteady Aerodynamic Effects

Wind turbine operation can be affected by several unsteady aerodynamic phenomena. The turbulent wind can cause rapid changes in the speed and in the direction of the rotor. These changes further lead to fluctuating aerodynamic forces [57]. Dynamic stall, dynamic inflow, and tower shadow are other phenomena that affect wind turbine operation.

The towering shadow refers to a deficit in the wind speed behind a tower. The incoming wind has to travel around the tower, resulting in the local inflow being affected by the tower. The blades of a downwind rotor will encounter a towering shadow once per revolution, leading to a rapid decrease in power [57].

Dynamic stall is a phenomenon that occurs when the wind speed changes rapidly due to sudden detachment and reattachment of airflow over an airfoil. This type of behavior cannot be predicted using steady-state aerodynamics. It can occur when a wind turbine blade encounters a shadow from the tower or during operation in windy conditions [57].

Dynamic inflow refers to the response of the wind flow to changes in the inflow field, such as turbulence and rotor operation. In an ideal situation, the induction factor would be updated immediately in response to changes in the incoming wind velocity [57]. The applied BEMT in SIMA includes the dynamic inflow [58].

2.5   Wind Turbine Controller Theory

A wind turbine requires a control system to connect all its subsystems for generating power. The control functions are carried out by a computer or microprocessor-based controller, which includes a safety system. The tasks of the wind turbine can be divided into two parts; supervisory control and operational control. Supervisory control monitors and manages the turbine operation and control actions, such as brake release and fault stopping. Dynamic control, also called operational control, manages the aspects of the machine operations where the dynamics of the machine affect the outcome of the control actions [60].

These control subsystems include blade pitch control, yaw control, generator control, brake control, and power converter control. The blade pitch control is responsible for adjusting the pitch angle of the turbine blades to optimize their angle of attack to the wind [60]. The generator control manages the electrical power output by controlling the rotational speed of the turbine rotor. The brake control system ensures that the turbine can be safely stopped in case of an emergency. The power converter control converts the turbine's electrical power from AC to DC or vice versa.

The 15-megawatt offshore reference IEA wind turbine is an example of a modern wind turbine that uses a Pitch-Regulated Variable Speed Control (PRVSC) [7]. This control system allows the turbine to vary its rotational speed to match the wind speed, resulting in maximum energy extraction.
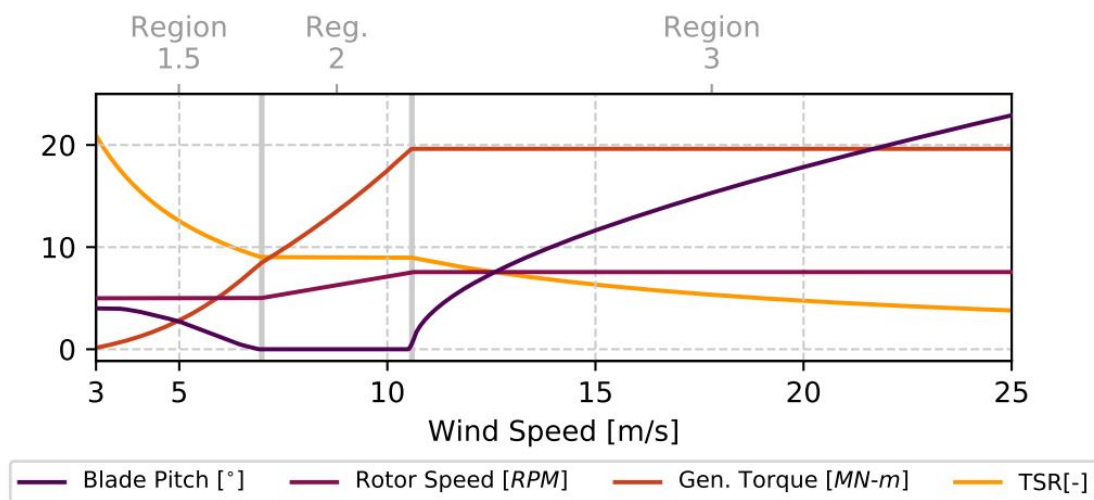
Figure 2.7: Power curve for a variable speed, variable pitch wind turbine [7].

The operational regions of the reference wind turbine are represented in Figure 2.7 [60]. This figure

illustrated developments of the blade pitch angle of the blades, the rotor speed, generated torque, and the tip speed ratio (TSR) for the different regions. In Region 1 (in the figure denoted as Region 1.5), the wind turbine is intentionally kept nonoperational to prevent potential damage resulting from power production. During this phase, the blade pitch angle is systematically decreased, while the torque generated is concurrently increased to optimize the power coefficient, denoted as C_p.

Moving into Region 2, the wind turbine starts to generate power, with the goal of maximizing the output [3]. The beginning of this region is determined by the cut-in wind speed, which is the minimum wind speed required for the turbine to produce useful power. The torque controller maintains a set point of TSR close to or at the maximum C_p [7], resulting in an increase in generated torque and blade pitch angle.

In Region 3, the wind turbine operates at its rated wind speed and rated power, representing the maximum power output it can generate [60]. It remains in this region until extreme weather or the incoming wind reaches the cut-out speed, which is the maximum wind speed at which the turbine can deliver power. To maintain the rated rotor speed, the blade pitch controller adjusts the blade pitch angle to feather during this period.

2.5.1   Negative Damping

The pitch controller of a wind turbine plays a crucial role in regulating the power output and stability of the system. However, the use of pitch control can lead to stability issues when operated at very low frequencies, particularly in floating offshore wind turbines (FOWTs) [8]. Negative damping is a phenomenon that occurs when the pitch controller amplifies the motion of the turbine instead of damping it. This can result in dangerous oscillations and potential damage to the turbine.

Unlike bottom-fixed wind turbines with higher frequencies and typically designed with pitch controllers in mind [12], FOWTs have lower frequencies. When pitch control is used in FOWTs, the controller may have more time to react to changes in wind speed, leading to negative damping. In high winds, the pitch controller reduces the thrust force by pitching the blades to a feathered position [8]. However, this can amplify the motion of the turbine, resulting in higher amplitude oscillations and potential damage to the system.

To avoid negative damping, it is essential that the pitch controller is designed and tuned correctly for the specific wind turbine system. This requires careful consideration of the system's natural frequencies and the effects of the controller on the system's response. By ensuring proper design and tuning, negative damping can be avoided, and the stability and safety of the wind turbine system can be ensured.

Figure 2.8 visually represents the negative damping problem in wind turbines [8]. The first column of the figure illustrates the behavior of a wind turbine located onshore, showing the variations in wind speed, rotor speed, blade pitch angle, and tower position in the y-direction. In this case, the tower frequency is 0.5 Hz, and the control frequency is 0.1 Hz, indicating that the control frequency is lower than the tower frequency. It can be observed that this leads to a stable response. The second column of the figure depicts a similar scenario but with an offshore wind turbine using an on-shore controller. Here, the tower frequency is 0.05 Hz, and the control frequency remains at 0.1 Hz, leading to instability. A coupling between tower motion and pitch control occurs [8]. Finally, the third and last column showcases the use of an adjusted 0.04 Hz controller for an offshore wind turbine with a tower frequency of 0.05 Hz. These three cases effectively highlight the importance of employing a controller that is specifically designed for offshore wind turbines, emphasizing its critical role in mitigating negative damping issues.

Instability in wind turbines is caused by thrust force on tower motion, with positive aerodynamic damping when the change in thrust with a change in wind speed is positive. Damping is positive at wind speeds below rated, but at high wind speeds, changed pitch angle settings result in a negative gradient, reducing loads and changing force direction. However, due to slow time constants in aerodynamics and pitch control, instantaneous changes in wind speed lead to constant induced velocities and pitch settings, resulting in positive damping [8].
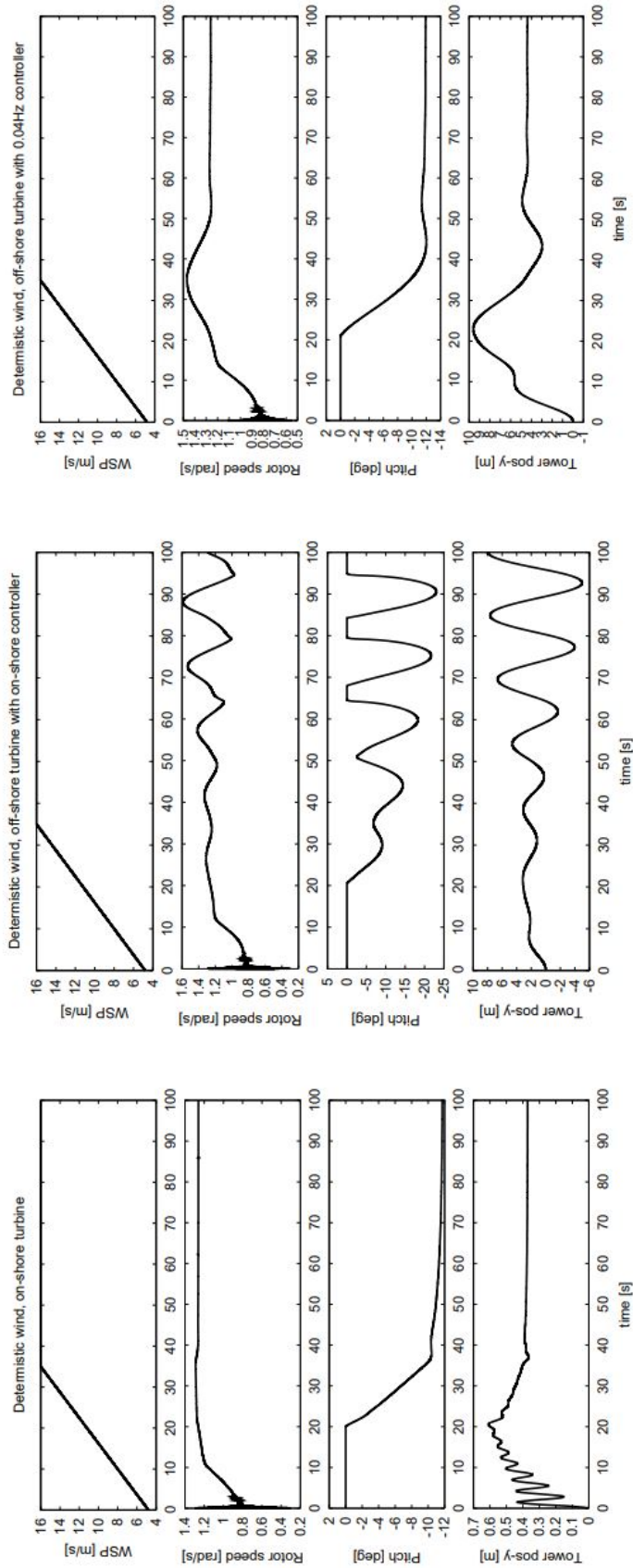
Figure 2.8: Comparison of tower vibration response on offshore and onshore wind turbines using different controllers [8].

2.6 Hydro-Aero-Servo-Elastic Coupling

The technical feasibility of floating offshore wind turbines (FOWT) can be demonstrated through two methods:

- On-site measurements and scaled model tests

- Numerical analysis

Numerical analysis is a more cost-effective and time-efficient option, and the two most popular methods for FOWTs are frequency-domain and time-domain analysis. The frequency-domain analysis is a type of numerical analysis that focuses on the behavior of a system over a range of frequencies. It is commonly used in the oil and gas industry to study the dynamic characteristics of FOWTs, such as the system's response to wave and wind loads. However, frequency domain analysis has limitations and cannot accurately calculate nonlinear behavior, which can be important in the design of FOWTs.

The time-domain analysis is another type of numerical analysis that focuses on the behavior of a system over time. It can consider a fully coupled aero-hydro-servo-elastic model, which considers the interaction between the system's aerodynamic, hydrodynamic, and structural behavior [61]. This type of analysis is more appropriate for FOWTs because it can capture the complex interactions between the different components of the system. Time-domain numerical tools can be developed from codes originally used for onshore bottom-mounted wind turbines or from the field of offshore structures in the oil and gas industry.

Accurate modeling of the behavior of a floating offshore wind turbine (FOWT) requires considering both aerodynamic and hydrodynamic loads [61]. The blade element momentum method with aerodynamic corrections is commonly used to calculate aerodynamic loads. This method uses mathematical models to predict the forces and moments acting on the turbine blades based on their shape, angle of attack, and wind speed and direction. Aerodynamic corrections can be applied to account for factors such as blade skew, twist, and camber. To calculate hydrodynamic loads, a number of different methods may be used. The linear potential-flow theory assumes that the water flows around the turbine can be modeled as a series of simple harmonic waves and uses this assumption to calculate the forces acting on the turbine. The second-order wave force theory is a more complex method that considers the non-linear behavior of the water flow and can provide more accurate results. Morison's formula with the strip theory is another commonly used method that considers the effect of the water flow on individual sections of the turbine. Further explanations of the different theories are presented previously in this chapter.

The structural response to hydrodynamic loads, also considering the load-response interaction, is known as hydro-elasticity and is important to consider in FOWT models. This can be done by coupling the hydrodynamic loads from potential theory with a structural formulation using RIFLEX and SIMO bodies. The same approach can be used for aerodynamic loads, resulting in an aero-elastic model considering the interaction between aerodynamic loads and structural response. A hydro-aero-elastic model can be obtained by coupling the hydro-elastic and aero-elastic models. A hydro-aero-servo-elastic model is obtained when controller logic is implemented, considering the interaction between structural response, hydro and aerodynamic loads, and controller [61]. This allows for a more accurate prediction of the behavior of the FOWT under different operating conditions.

2.7 Statistical Description of Sea

Statistical characteristics, such as significant wave heights, peak wave period, wind speed, and direction, can describe the sea. These statistics can be used to predict and model the behavior of the sea and the wind, as well as their effect on objects in the sea, such as ships and offshore structures.

2.7.1 Ocean Waves

Ocean waves are, in reality, composed of several non-linear components with different directions and are driven over variable distances by the wind. Waves interact with currents, tides, the sea floor, the coastline, and different obstacles. For such a complex situation, reasonable approximations have been proven to be possible by assuming the linear potential wave theory and the flow to be incompressible, irrational, and inviscid [5]. To simulate irregular waves, linear wave theory can be used as a sum of a large number (N) of wave components with different frequencies. The free surface elevation for long-crested waves can be expressed as in Equation 2.32, according to linear wave theory [62]. A_j is the amplitude of the jth wave, ω_j the frequency, k_j the wave number, and ϵ_j the phase angle.

$$\eta(t) = \sum_{j=1}^{N} A_j \sin(\omega_j t + k_j x + \epsilon_j) \tag{2.32}$$

The wave elevation in Equation 2.32 is approximately Gaussian distributed for a large number of N. By assuming Gaussian sea surface elevation and stationarity, then the wave spectrum ($S_\eta(\omega)$) determines all statistical characteristics. The wave spectrum represents the wave energy distribution on the frequencies of the wave components and describes the sea surface as a stochastic process [62]. When the wave spectrum is divided into components j with spacing $\Delta\omega$ and a phase $[0,2\pi]$, the amplitude can be expressed as in Equation 2.33. The relationship between the time-domain solution of the waves, Equation 2.32, and the frequency domain representation of the wave by a wave spectrum is illustrated in Figure 2.9.

$$\frac{1}{2} A_j^2 = S_w(\omega)\Delta\omega \tag{2.33}$$
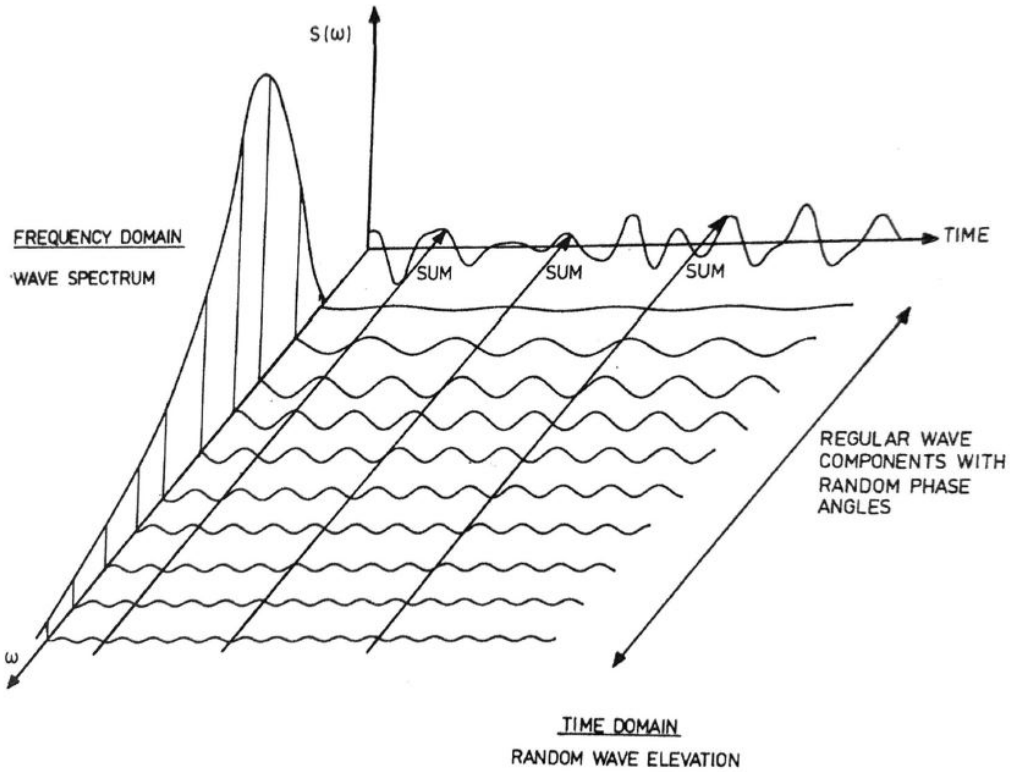
Figure 2.9: Relationship between a frequency domain and time domain representation of waves in a long-crested short-term sea state [5].

A wave spectrum is given by the significant wave height (Hs) and the peak period (Tp). The significant wave height is defined as the mean of the largest waves of one-third in the sea state, and the peak period is the period with the highest value of the spectrum [5]. According to Holthuijsen [62], the spectral moments can express the statistical properties of the wave elevation, Equation 2.34. Further, the significant wave height can be expressed as $Hs = 4\sqrt{m_0}$.

$$m_n = \int_0^\infty \omega^n S(\omega) d\omega \tag{2.34}$$

Several existing spectra describe the sea state; the Pierson-Moskowitz (PM) spectrum, the JON-SWAP spectrum, the Gamma spectrum, the ISSC spectrum, etc. [5]. The PM spectrum is assumed to represent fully developed conditions in deep water, expressed in Equation 2.35. The JONSWAP spectrum was developed for the Southeast part of the North Sea and is expressed as in Equation 2.36 [63].

$$S(\omega) = \frac{\alpha g^2}{\omega^5} \exp\left(-\beta \left(\frac{\omega_p}{\omega}\right)^4\right) \tag{2.35}$$

$$S(\omega) = \frac{\alpha g^2}{\omega^5} \exp\left(-\beta \left(\frac{\omega_p}{\omega}\right)^4\right) \gamma^{\exp\left(\left(\frac{-(\omega-\omega_p)^2}{\sigma^2}\right)\right)} \tag{2.36}$$

The parameters α, β and γ are called the spectral-, form- and peakedness parameters [5, 63], respectively. The parameter σ is the standard deviation, and squared is the wave elevation variance, $\sigma^2 = m_2$. The significant wave height Hs) is related to the spectral parameter, α, while the peak period is related to the peak frequency, $Tp = 2\pi/\omega_p$. Figure 2.10 illustrates the difference between using the PM and the JONSWAP spectrum.
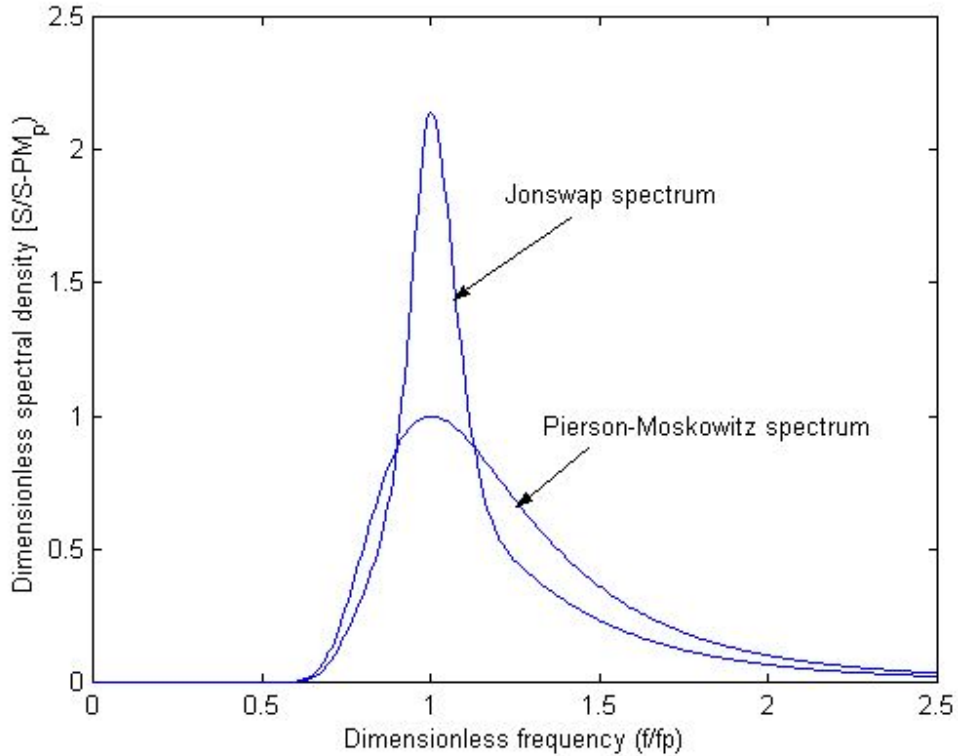
Figure 2.10: Comparison of PM and JONSWAP spectrum [5, 9]

2.7.2 Wind

Wind speed consists of lateral, longitudinal, and vertical components, while the longitudinal components follow the direction of the wind. The mean wind speed varies with the temporal variation and the height above the ground. The variation is due to viscous boundary layer effects, leading to variation of the load of the wind turbine at the 3P frequency [57]. The power law formulation is a widely used formulation for wind speeds at different heights. Equation 2.37 is the recommended formulation from DNV [64], where the $U(z_0)$ is the reference height at usually 10 m, z_0 the reference height and α the power law exponent, recommended to be $\alpha = 0.14$ for offshore locations.

$$U(z) = U(z_0) \left(\frac{z}{z_0} \right)^{\alpha} \tag{2.37}$$

The temporal variations in wind speed can be divided into; inter-annual, annual, diurnal, and short-term (gust and turbulence). The mean wind speed is usually reported for a period of 10 minutes [57]. The longitudinal wind speed is the sum of the mean wind speed and the fluctuating wind speed. The ratio between the mean wind speed at the reference height and the standard deviation of the wind speed define the intensity of the turbulence, given in Equation 2.38. The TI represents the intensity of the turbulence, σ_u is the standard deviation of the wind, and $\bar{U}$ is a mean reference wind. Turbulence intensity can be obtained from design standards, as many locations lack detailed wind observations.

$$TI = \frac{\sigma_u}{\bar{U}_{ref}} \tag{2.38}$$

The turbulence spectrum describes the frequency content of wind speed variation [10]. The law of Kolmogorov states that the spectrum must, at high frequencies, approach an asymptotic limit that is proportional to $\omega^{-5/3}$. Two alternative methods to express the spectrum of the longitudinal component of turbulence are the Kaimal and von Karman spectra. They can be expressed as in Equation 2.39 and Equation 2.40, respectively [10]. σ_u^2 is the variance, and L_{1u} and L_{2u} is the length scale.

$$S(\omega) = \frac{4L_{1u}\sigma_u^2/\bar{U}}{(1 + 6\omega L_{1u}/\bar{U})^{5/3}} \tag{2.39}$$

$$S(\omega) = \frac{4L_{2u}\sigma_u^2/\bar{U}}{(1 + 70.8(\omega L_{2u}/\bar{U})^2)^{5/3}} \tag{2.40}$$

Figure 2.11 compares Kaimal and von Karman spectra for a wind speed of 12 m/s. Note that the notation is slightly different, but the principle still holds.

To simulate the wind turbine's response due to turbulent wind, several methods exist for constructing a "turbulence box" with wind components [12]. One of the methods available is to use a one-dimensional fast Fourier transformation (FFT) to generate time histories of each direction based on Kaimal or von Karman spectra. Another method uses a three-dimensional FFT to create correlated components, the Mann model [12]. Turbsim, developed by NREL, is a stochastic simulator to simulate the turbulent wind of the entire field [17]. The wind is simulated using TurbSim to generate the turbulence box according to the Kaimal spectrum.
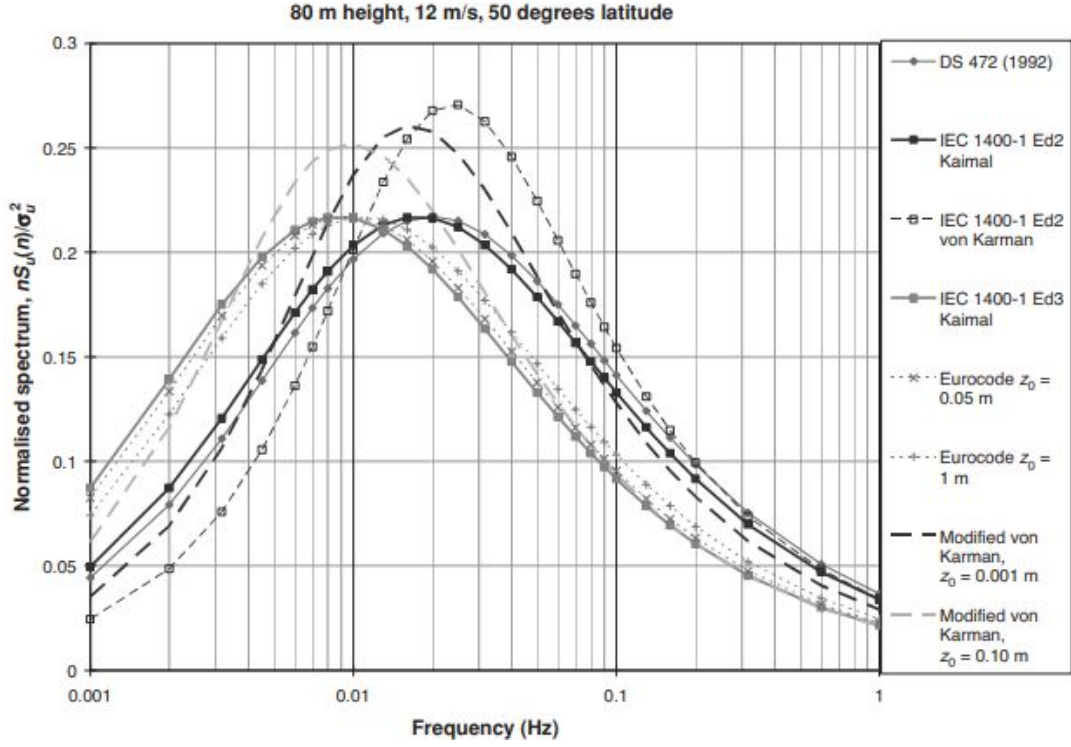
Figure 2.11: Comparion of Kaimal and von Karman for a wind speed of 12 m/s [10]

2.7.3 Response Spectrum

According to Naess [65], the response of a linear and time-invariant system to a stationary load process is also stationary. It can be shown that the response spectrum, S_X, of a single degree of freedom mass-spring-dashpot is related to the forcing spectrum, S_F, by a transfer function H_{FX} [65], given in Equation 2.41.

$$S_X(\omega) = |H_{FX}(\omega)|^2 S_F(\omega) \tag{2.41}$$

For the one degree-of-freedom (1DOF) system, the transfer function can be expressed as in Equation 2.42.

$$H(\omega) = \frac{1}{-m\omega^2 + i\omega c + k} = \frac{1}{k\sqrt{(1 - \beta^2) + 2i\lambda\beta}} \tag{2.42}$$

According to linear wave theory, the wave force is proportional to the wave amplitude. With this assumption, the response amplitude operator (RAO) is the transfer function between the response spectrum and the wave spectrum [12]. The response spectrum is then given as in Equation 2.43 [5, 62]. The transfer function, RAO, is the response amplitude per unit of wave amplitude [5, 66].

$$S_R(\omega) = |H(\omega)|^2 S_\eta(\omega) = |RAO|^2 S_\eta(\omega) \tag{2.43}$$

The RAO is a useful tool in the case of linear systems. However, including non-linearities in the forcing and structure, the response spectrum extends beyond the frequencies included in the input wave spectrum. Also, for the wind turbine, the wind and the controller complicate things even further [12].

2.7.3.1 Multi-DOF System

The equation of motion for a multi-degree-of-freedom (multi-DOF) system can be expressed as shown in Equation 2.44. In this equation, the matrices $\mathbf{M}$, $\mathbf{C}$, and $\mathbf{K}$ represent the mass, damping, and stiffness of the system, respectively. The vector $\vec{r}(t)$ represents the displacement of the system at time t, while $\dot{\vec{r}}(t)$ and $\ddot{\vec{r}}(t)$ represent its velocity and acceleration, respectively. The vector $\mathbf{Q}(t)$ represents the applied external loads.

$$\mathbf{M}\ddot{\vec{r}}(t) + \mathbf{C}\dot{\vec{r}}(t) + \mathbf{K}\vec{r}(t) = \mathbf{Q}(t) \tag{2.44}$$

Solving Equation 2.44 yields a complex frequency-response matrix, expressed in Equation 2.45. Each element $H_{ij}(\omega)$ of the matrix $\mathbf{H}(\omega)$ represents the response in degree-of-freedom number i, which is due to a unit amplitude harmonic load in degree-of-freedom number j [11].

$$\mathbf{H}(\omega) = [\mathbf{K} - \omega^2\mathbf{M} + i\omega\mathbf{C}]^{-1} \tag{2.45}$$

Langen and Sigbjornsson [11] showed that the spectral density of the response, denoted $\mathbf{S_R}(\omega)$, can be expressed as shown in Equation 2.46. In this equation, $\mathbf{S_Q}(\omega)$ represents the spectral density of the external loads, which can be expressed in terms of the hydrodynamic transfer matrix $\mathbf{F}(\omega)$ and the spectral density of the waves, denoted as $S_\eta(\omega)$ [11].

$$\mathbf{S_R}(\omega) = \mathbf{H}(\omega)\mathbf{S_Q}(\omega)\mathbf{H}^{*T}(\omega) = \mathbf{H}(\omega)\mathbf{F}(\omega)\mathbf{H}^{*T}(\omega)S_\eta(\omega) \tag{2.46}$$

2.7.3.2 Dynamic Amplification Factor

Determining the response of a system due to an external force or input is often necessary for analyzing dynamic systems. This response can be characterized by the system's transfer function, which describes the relationship between the input and output signals. The transfer function can be found in the system's equations of motion and is typically expressed in terms of the frequency response, which is the output response as a function of frequency.

For a single-degree-of-freedom system, the transfer function can be expressed in terms of the mechanical properties of the system, such as stiffness, mass, and damping. The mechanical transfer function can be found from the absolute value of the transfer function and can be expressed as in Equation 2.47 [11].

$$|H(\omega)| = \sqrt{H(\omega)H^*(\omega)} = \frac{1}{k\sqrt{(1-\beta^2)^2 + (2\lambda\beta)^2}} \tag{2.47}$$

Here, $\beta = \omega/\omega_n$ is the frequency ratio, and $\lambda = c/(2m\omega_n)$ is the damping ratio, where ω_n is the eigenfrequency of the system. The eigenfrequency describes the relationship between stiffness and mass $\omega_n^2 = k/m$.

The dynamic amplification factor (DAF) is defined as the ratio between dynamic and static displacement and can be expressed as in Equation 2.48 [11].

$$DAF = \frac{(u_{max})dyn}{(u)stat} = \frac{|H(\omega)|}{H(0)} = \frac{1}{\sqrt{(1-\beta^2)^2 + (2\lambda\beta)^2}} \tag{2.48}$$

The DAF provides a measure of the system's response to a harmonic input and can be used to assess the system's stability and performance.

In order to determine the damping matrix of a system, several methods can be used, such as element formulation, proportional damping, and direct development of the orthogonal damping matrix

[11]. Of these methods, element formulation and direct development are the most commonly used. Proportional damping is a commonly used assumption in which the damping matrix is assumed to be proportional to the stiffness and mass matrices. The modal damping coefficient can be expressed as in Equation 2.49, as introduced previously.

$$\bar{c}_i = \alpha_1 \bar{m}_i + \alpha_2 \bar{k}_i \tag{2.49}$$

Where ϕ is the mode shape vector and $\bar{m}_i$ and $\bar{k}_i$ are the mass and stiffness matrices in modal coordinates, respectively. The damping ratio can be expressed as in Equation 2.50 [11].

$$\lambda_i = \frac{\bar{c}_i}{2\bar{m}_i\omega_i} = \frac{1}{2}\left(\frac{\alpha_1}{\omega_1} + \alpha_2\omega_i\right) \tag{2.50}$$

where ω_i is the ith natural frequency. The proportional damping coefficients α_1 and α_2 can be found from the damping ratios using the following equations:

$$\alpha_1 = \frac{2\omega_1\omega_2}{\omega_2^2 - \omega_1^2}(\lambda_1\omega_2 - \lambda_2\omega_1) \tag{2.51}$$

$$\alpha_2 = \frac{2(\omega_2\lambda_2 - \omega_1\lambda_1)}{\omega_2^2 - \omega_1^2} \tag{2.52}$$
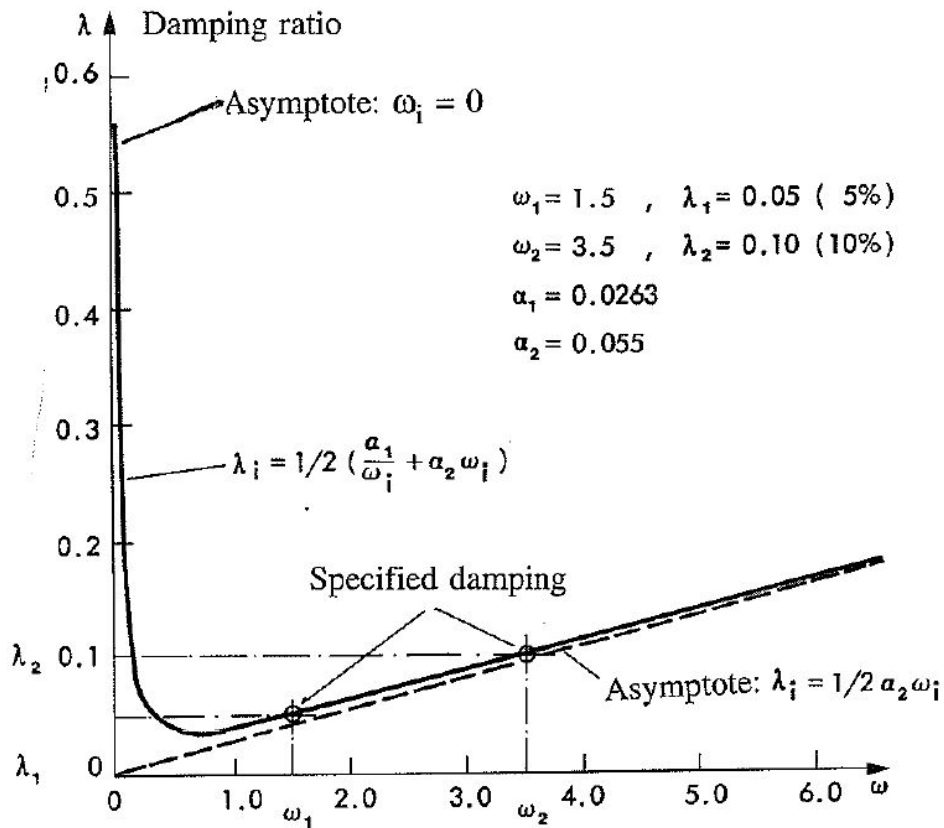
Figure 2.12: Damping ratio as a function of eigenfrequency [11]

2.8   Limit State Design

Steel structures are subjected to several types of loads and deformations resulting from service requirements ranging from routine to accidental or extreme [67]. The traditional allowable stresses design focuses on keeping the stresses resulting from design loads under a certain working stress level based on experience from similar successful cases. Opposed to the allowable stress design, the limit state design is based on the explicit consideration of several different conditions, where the structure may fail to fulfill its intended function [67]. The applicable strength or capacity is used in design as the limit.

The limit-state design approach has become the preferred design method and is commonly used in steel structure codes and standards worldwide. According to the DNV-standard DNV-OS-J101 [68], the limit state is defined as *'a condition beyond which a structure or structural component will no longer satisfy the design requirements.'* The limit states can be divided into:

- Service limit state - SLS

- Ultimate limit state - ULS

- Fatigue limit state - FLS

- Accidental limit state - ALS

The SLS represents the failure state for normal operations. Such a failure state may be caused by excessive vibrations or damage due to corrosion. The ULS corresponds to the maximum load-carrying resistance of a structure, representing the collapse due to loss of strength or stiffness of the structure. Such loss may be related to loss of equilibrium or instability in part of the structure [68].

FLS represents the appearance of fatigue cracks in the structure. This is due to repeated loading leading to stress concentration and damage accumulation. Finally, the ALS represents the maximum load-carrying capacity for rare accidental loads and post-accidental integrity for damaged structures. Such loads may be caused by events such as collision, explosion, or fire [68].

The selection of appropriate limit state design criteria is critical in ensuring that the steel structure is safe, reliable, and durable over its intended service life. Therefore, the limit-state design approach has become the preferred method for designing steel structures. It considers different failure modes and ensures that the structure is safe and fit for its intended purpose [68].

2.9   Fatigue Analysis

Fatigue damage corresponds to a crack in a structure due to variation in cyclic stress. The fatigue process is classified either as high-cycle or low-cycle fatigue. High cycle fatigue failures are caused by stresses lower than the yield stress of the structure. Such material imperfections lead to the formation of cracks. To estimate the fatigue life of a structure, it is necessary to determine the stress history at different locations in the structure. Fragile spots, such as welds and bolts, are especially important [12]. The low cycle fatigue failures are due to stresses in the plastic deformation range [13].

Dynamic finite element results give the history of loads at different cross sections. The loads are denoted N_x (axial force), V_y and V_z (shear force), M_x (torsional moment) and M_y and M_z (bending moments). The σ_x (axial stress) and τ_θ (shear stress) can be determined by Equation 2.53 and Equation 2.54, based on the coordinate system in Figure 2.13. Here, A is the cross-sectional area, J is the polar moment of area, and I_y and I_z are the second moment of area for the cross-section.
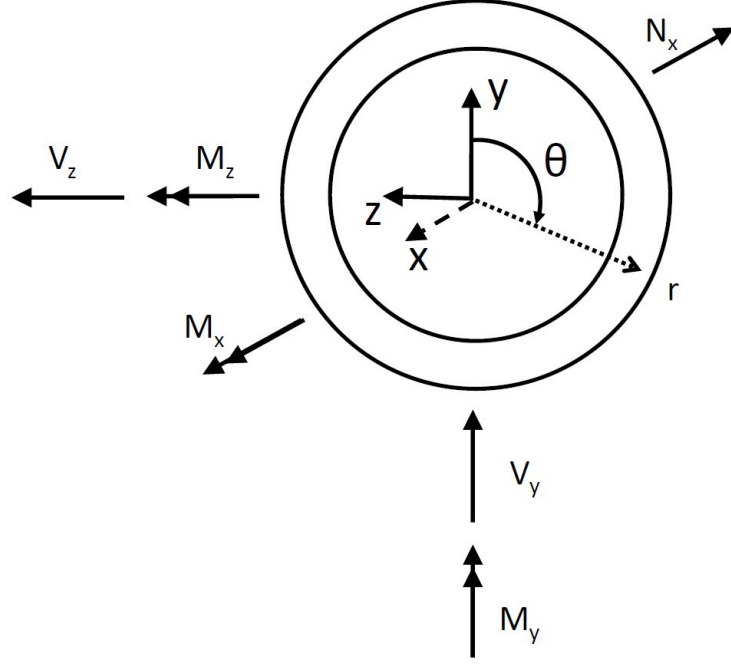
Figure 2.13: Coordinate system for sectional loads [12]

$$\sigma_x = \frac{N_x}{A} + \frac{M_y}{I_y} r \sin(\theta) + \frac{M_z}{I_z} r \cos(\theta) \tag{2.53}$$

$$\tau_\theta = \frac{M_x}{J} r + \frac{2V_y}{A} \sin(\theta) + \frac{2V_z}{A} \cos(\theta) \tag{2.54}$$

For the fatigue design of floating offshore wind turbines, the standard DNV-RP-C203 is commonly used [12, 36, 38]. The fatigue life is based on the S-N fatigue approach, assuming linear cumulative damage, the Miner-Palmgren hypothesis. In accordance with DNV-RP-C203, a two-slope S-N curve is selected to calculate the number of cycles to failure, N, corresponding to the stress range, $\Delta\sigma$. This is expressed in Equation 2.55, where m is the Wöhler exponent, t_{ref} the reference thickness in the tower, t the thickness of the structure, and k is the thickness exponent. For cases where the structure is corrosion protected or in air, a higher number of stress cycles with smaller amplitude is allowed [13]. Figure 2.14 illustrates that the S-to-N relationship can be described as bi-linear. The S-N curve refers to the hot spot stress, which means concentrated stress around a change in geometry, typically a weld toe.

$$N = KS^{-m} \rightarrow \log(N) = \log(\bar{a}) - m \log \left[\Delta\sigma \left(\frac{t}{t_{ref}} \right)^k \right] \tag{2.55}$$

The fatigue damage of the FOWT can be referred to as in Equation 2.56, where D is the accumulated fatigue damage, n_j is the number of stress cycles in stress block i, N_i is the number of cycles to failure at constant stress range, $\bar{a}$ is the intercept of the design S-N curve with the $log(N)$ axis, m is the negative inverse slope of the S-N curve, k is the number of stress block and η is the usage factor. The damage value D can be considered as the proportion of the fatigue life used in one cycle of the stress range S.

$$D = \sum_{i=1}^{k} \frac{n_i}{N_i} = \frac{1}{\bar{a}} \sum_{i=1}^{k} (n_i \cdot (\Delta\sigma_i)^m) \leq \eta \tag{2.56}$$
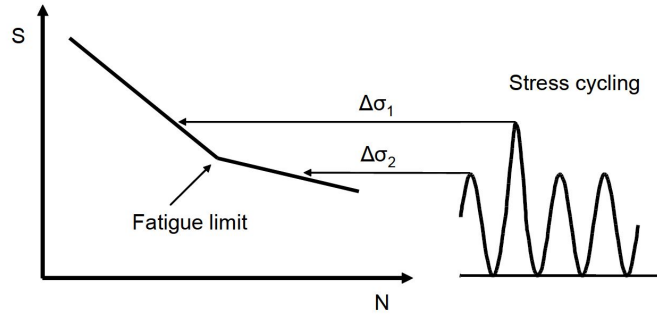
Figure 2.14: Typical bi-linear S-N-curve with an illustration of cyclic stress [13].

To calculate the damage from stress histories using S-N - curves, the cycles, and stress range must be counted. The most commonly used method for cycle counting is the Rainflow method, further explained in Section 2.9.1.

2.9.1 Rain Flow Counting

Rainflow counting is a technique to get the equivalent stress range from the history of loads [14]. Normal stress time series are calculated using Equation 2.53, including axial force and bending moments. The idea of flow counting is to count the cycles of the strain deformation and is done by finding terminations of flow. As illustrated in Figure 2.15, the flow is terminated when it merges with the start of the flow from a previous tensile peak, or encounters an opposite tensile peak with a larger amplitude. It also ends with the time series.
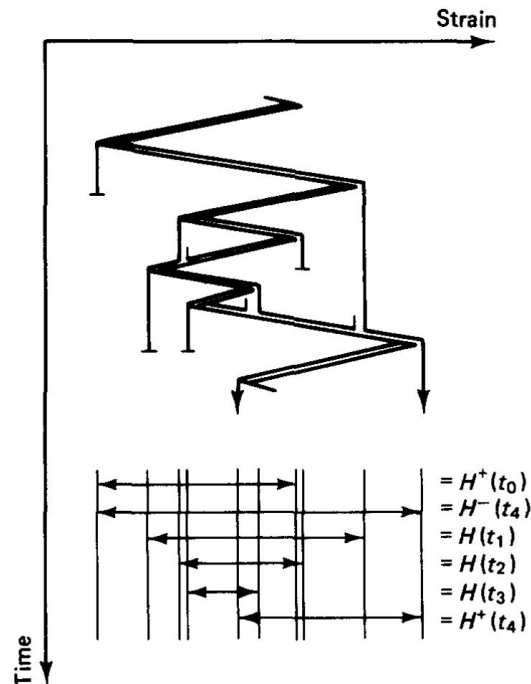
Figure 2.15: Illustration of an example of rainflow counting [14]

After counting the load cycles, the equivalent stress range can be found as in Equation 2.57

$$\Delta\sigma_{eq} = \left[\frac{\sum_i n_i (\Delta\sigma_i)^m}{\sum_i n_i} \right]^{1/m} \tag{2.57}$$

2.10   Numerical Tools for Wind Turbine Analysis

Accurate modeling of wind turbine dynamics, platform hydrodynamics, a mooring system, and control algorithms are required to enable the design of floating offshore wind turbines (FOWT) [69]. A time-domain numerical analysis capable of capturing the aero-hydro-servo-elastic response of FOWTs is necessary to conduct. Cordle and Jonkman provided an overview of several numerical analysis tools [70]. The two simulation tools developed in the wind turbine industry are FAST and SIMA. The different models used for the two numerical tools are presented in Table 2.1.

Numerical tool	Structural model	Aerodynamic model	Hydrodynamic model	Mooring model
SIMA	Finite element	Blade element momentum	Potential flow and Morison	Finite element or Quasi-static
FAST	Modal	Blade element momentum and Generalized dynamic wake	Potential flow and Morison	Quasi-static

Table 2.1: Different models used for FAST and SIMA [13]

2.10.1   FAST

FAST (Fatigue, Aerodynamics, Structures, and Turbulence) is a coupled aero-hydro-servo-elastic analysis tool for FOWTs developed by NREL [71]. OpenFAST is a publicly available code wind turbine simulation tool that builds on FAST version 8 (FAST v8). It represents the effort to support better the open-source developer community around the FAST-based aero-hydro-servo-elastic engineering models. OpenFAST joins aerodynamic models, hydrodynamic models, control and electrical (servo) dynamic models, and structural (elastic) models to enable coupled nonlinear simulations in the time domain [53]. OpenFAST can run large numbers of nonlinear time domain simulations to predict wind system ultimate and fatigue loads. However, the nonlinear model can also be linearized to calculate natural frequencies, damping, and mode shapes.

The aerodynamic model uses wind-inflow data and solves for the rotor-wake effects and blade element loads. The hydrodynamic model simulates both regular and irregular waves, including the current. The control and electrical systems model the controller logic, sensors, and actuators together with the control and electrical systems. The dynamic structural model applies the reactions and loads from the mentioned models, adds gravitational loads, and simulates the elasticity of the rotor, drivetrain, and support structure [53].

Several software combines FAST with other codes. An example is FAST.farm, which extends the capabilities of OpenFAST to simulate each wind turbine in a farm with the OpenFAST model and capture relevant physics. It includes wake dynamics and a super controller. The super controller solves the dynamics of the super controller of a wind plant [53]. Another coupled analysis tool is FASTlink, which couples Orcaflex and FAST. OrcaFlex is a computer program applying a time-domain formulation used to model the coupled behavior between a surface vessel and its mooring system or to model the response of cables [69]. These models discretize the mooring lines into an idealized system of mass components (nodes) connected to visco-elastic elements. FAST models the wind turbines with their aerodynamic loads, control system, tower, and six degrees of freedom platform motions. Orcaflex models the subsea components, such as anchor lines and the hydrodynamics of the support platform [69].

2.10.2   SIMA

For the coupled analysis of the FOWT, the software Simulation Workbench for Marine Applications (SIMA) has been used. SIMA is software for analyzing complex multibody systems, such as the support structure of a wind turbine, and includes mooring analysis [72]. The response of the system is calculated by non-linear time domain analysis. This ensures dynamic equilibrium for every time

step and gives proper time domain interaction between the blade dynamics, the mooring dynamics, and tower motions [73]. The software is used to easily interface RIFLEX, SIMO, the blade element momentum (BEMT) code, and controller logic, and provides a fully coupled analysis: The different components are connected as shown in Figure 2.16. Thus, there was five separate codes/software interacting in the hydro-aero-servo-elastic coupled time-domain global dynamic analysis model:

1. RIFLEX - Structural dynamics

2. SIMO - Hydrodynamic loads

3. The BEMT code (Aerodyn) - Aerodynamic loads

4. The wind turbine controller (Java control)

5. SIMA - Couples the four codes mentioned above
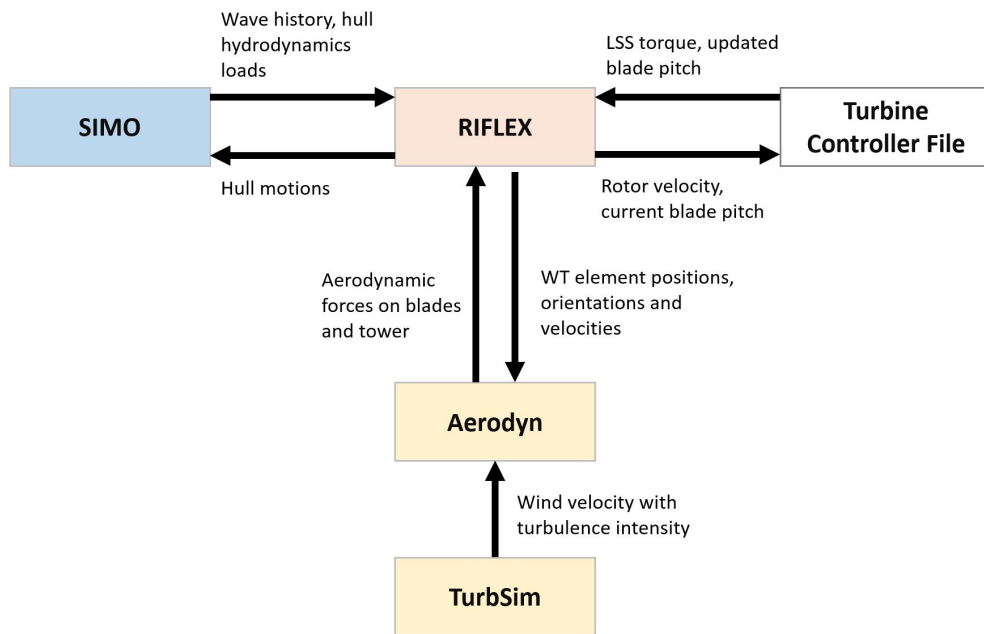
Figure 2.16: Overview of how the different computer programs interact in SIMA [12]

MARINTEK developed RIFLEX as a computer program system for the analysis of slender marine structures and is a nonlinear time domain program with a finite element (FE) formulation. It can perform coupled analysis, where rigid-body floating systems are integrated with dynamic models. Slender structures usually consist of complex cross-sections, which are applied in RIFLEX as a global cross-section model, giving global deformations and stress resultants. The nonlinear cross-section behavior is modeled by the nonlinear relations between global deformation parameters and stress resultant [15]. The element in RIFLEX can be either beam or bar elements. The beam element has three translational and three rotational degrees of freedom (DOF), while the bar element has six translational DOF [3]. The program computes the static and dynamic characteristics of the analyzed structure and is based on a non-linear formulation of finite elements. The key features included in RIFLEX are the following:

- Flexible modeling of both simple and complex systems.

- Nonlinear time domain simulation of motions and forces

- Nonlinear cross-section properties

- Generalized Morison type of load model

An illustration of the structure of RIFLEX is shown in Figure 2.17. SIMO, however, is a computer program for simulating motions and station-keeping behavior of a complex system of floating structures [58]. RIFLEX and SIMO include aerodynamic loads based on blade element momentum theory (BEMT). The aerodynamic formulation includes empirical tip loss and dynamic stall corrections. A PI control algorithm regulates the pitch angle of the blade [73]. Ormberg and Bachynski extended the well-proven state-of-the-art simulation tool for global analysis of floating structures to include offshore wind turbine applications [73]. The program was first developed for rigid-body models, but later it was further developed for elastic models [12].
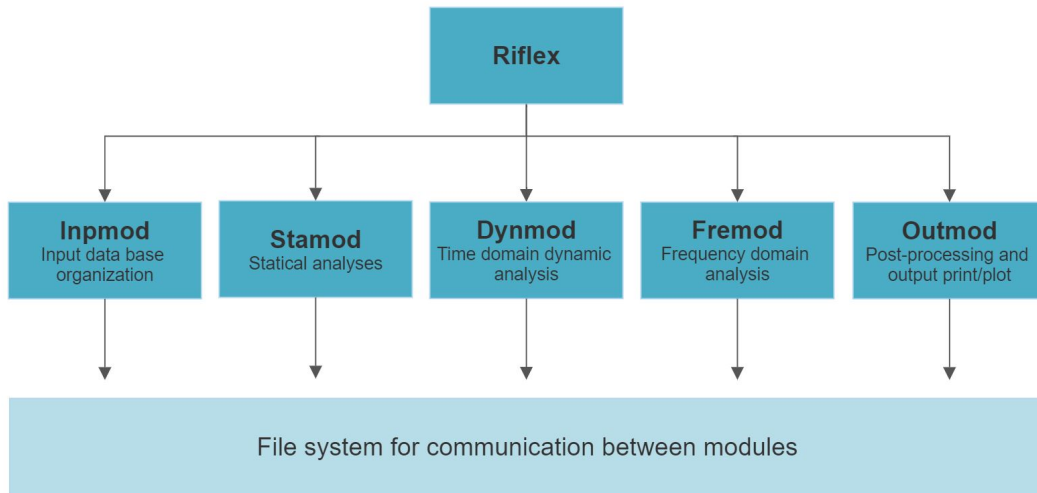
Figure 2.17: Structure of the program system RIFLEX [15]

An overview of a typical structural and external load model for a semi-submersible floater on a floating wind turbine is illustrated in Figure 2.18.
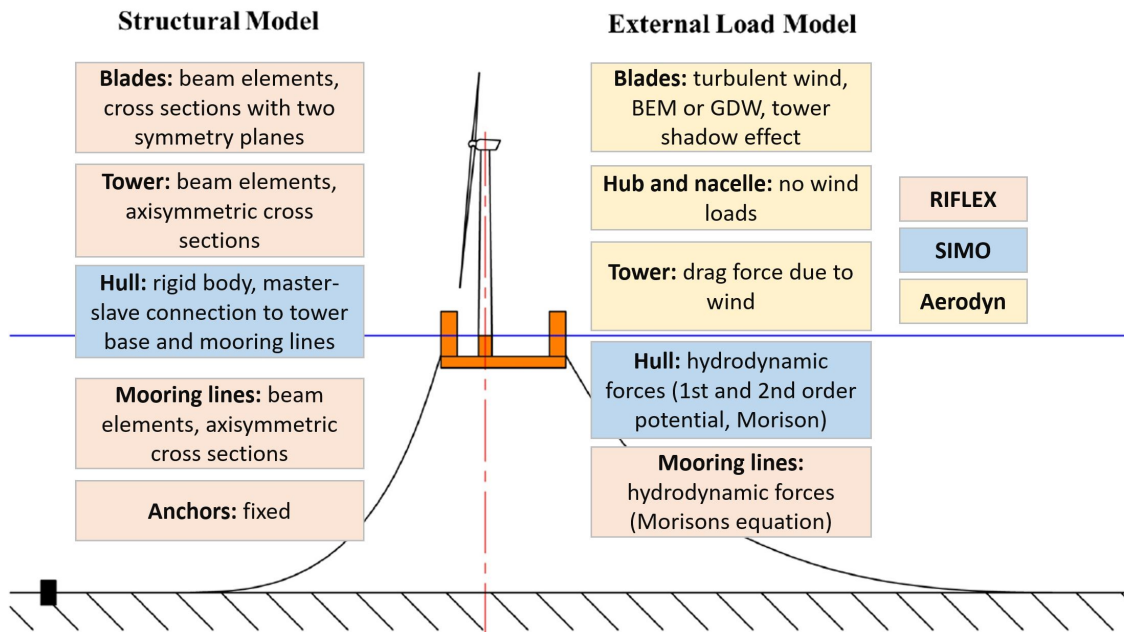
Figure 2.18: Structural model and external load model of the semi-submersible floating wind turbine [12, 16]

2.10.3 TurbSim

This thesis used the TurbSim program from NREL to generate turbulent wind fields. TurbSim simulates stochastic, full-field turbulent wind. It numerically simulates time series of three-component wind speed vectors at certain points in a two-dimensional vertical rectangular grid fixed in space [17]. The set-up of how TurbSim is built is illustrated in Figure 2.19.
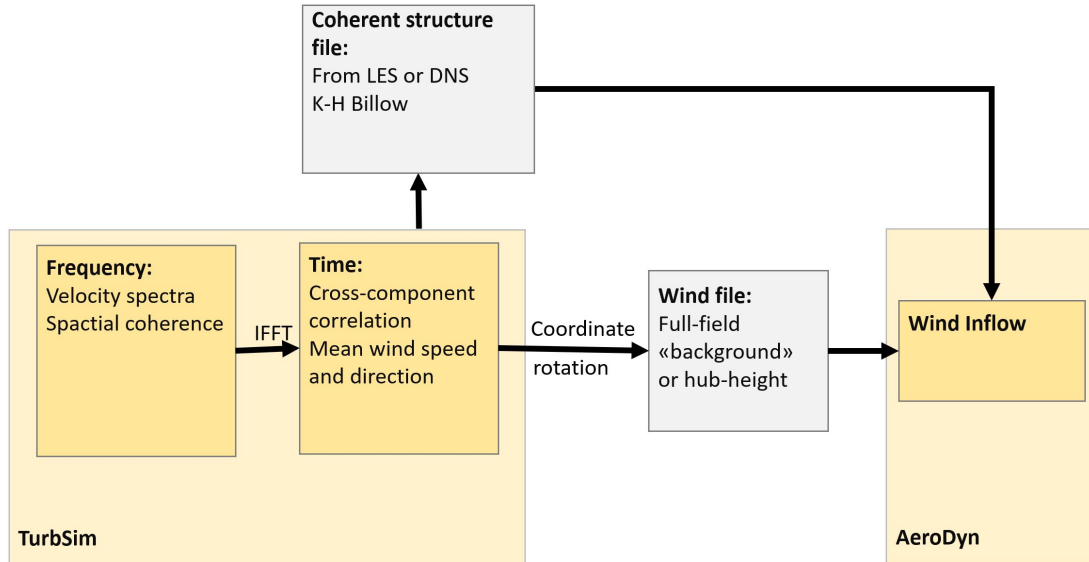
Figure 2.19: TurbSim simulation method [17].

The wind is generated as a turbulence box according to Kaimal or von Karman spectra, including cross-component correlation and spatial coherence [17], as illustrated in Figure 2.20. The frequency domain defines spectra of velocity components and spatial coherence, which can be transformed into time series through inverse Fourier transforms. This simulation method assumes a stationary process. To incorporate non-stationary components, TurbSim can combine coherent turbulent structures with the time series it generates when used in conjunction with AeroDyn [17].
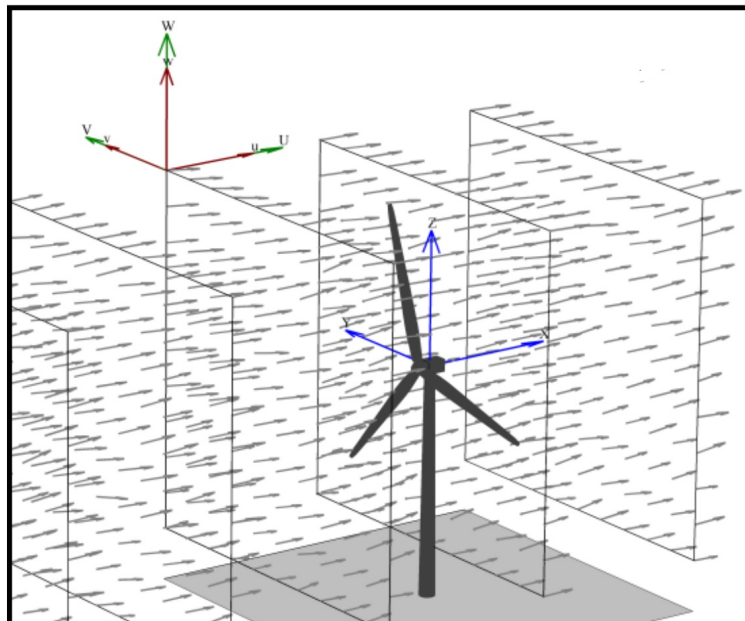
Figure 2.20: Wind field with flow angle 0° [17].

2.10.4 Sesam Package

To model the structure of the floater used in SIMA, several computer programs are essential to mention. The software suite Sesam is a software package for marine applications developed by DNV. The key software relevant to this thesis is GeniE, HydroD, Sesam Wind Manager, and Wadam. Figure 2.21, illustrates the different components in the package, including SIMA.

GeniE is a software tool for conceptual design and models beams, stiffened plates, and shells [18]. Equipment loads, explicit loads, and wind loads are possible to model. For further analysis, the model is transferred to Sestra for structural analysis, Wajac or Wadam for hydrodynamic analysis, Splice for pile-soil analysis, and Installjac for launch and upending analysis. All of these software tools are integrated into GeniE.

With the panel model modeled in GeniE, HydroD calculates the wave-structure interactions for both floating and fixed structures. The hydrodynamic analysis is performed by running Wadam or Wasim in the background. Wadam performs the analysis in the linear frequency domain, while Wasim performs the analysis in the non-linear time domain [18].

The Sesam Wind Manager is software to analyze fatigue and the ultimate strength of offshore wind structures in the time domain. This requires data from Wasim in HydroD and SIMA. The software simplifies the process of configuring and managing multiple simulations with diverse environmental conditions [18].
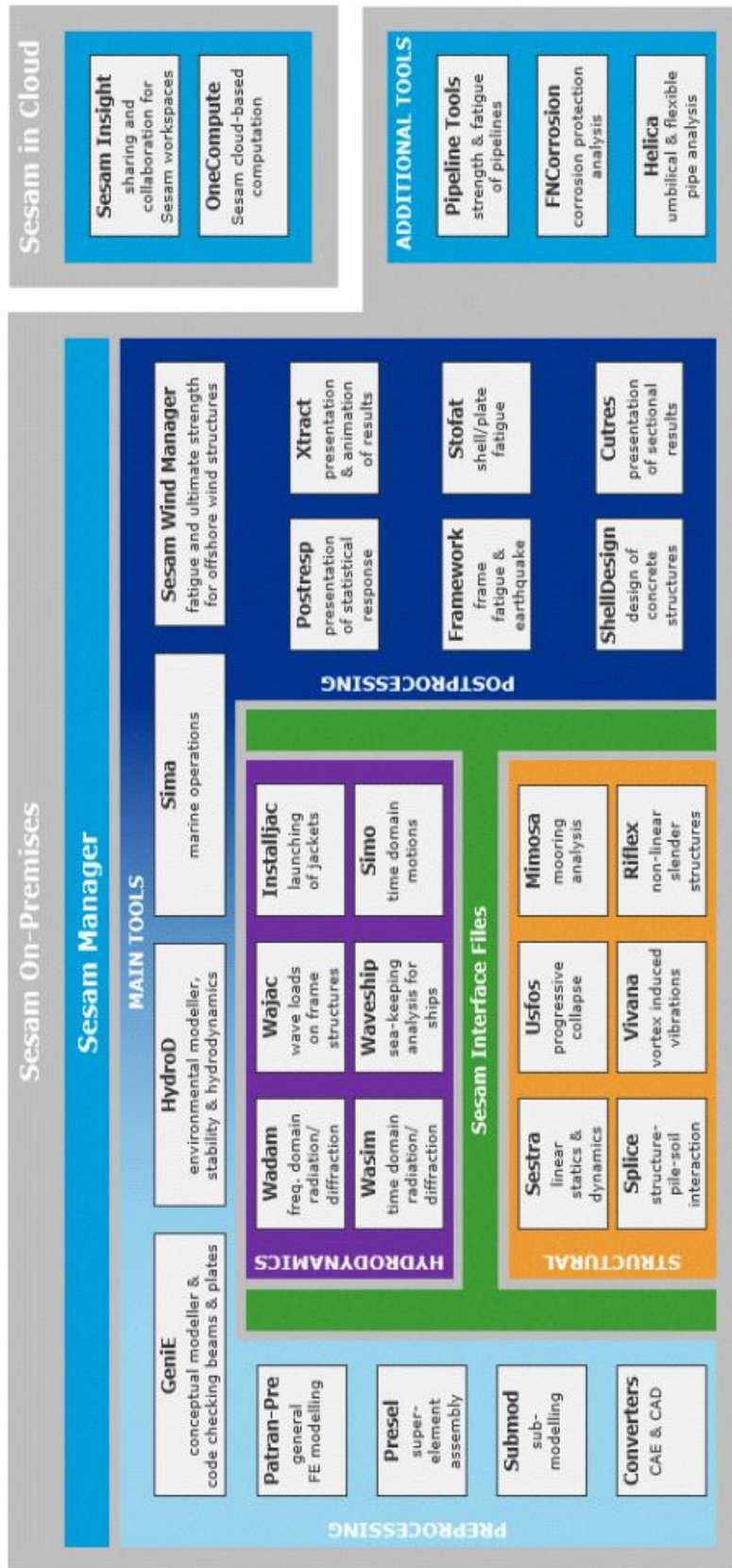
Figure 2.21: Overview of the Sesam package [18].

Chapter 3

The Case Scenario

3.1 Reference Wind Turbine

The investigations in this thesis focus on the UMaine VolturnUS-S Reference Platform [4], developed for use with the IEA Wind 15-Megawatt Offshore Reference Wind Turbine [7]. The IEA 15-MW wind turbine, designed by the University of Maine (UMaine), is representative of the larger offshore machines currently in use in the wind industry [7]. The platform itself is a semi-submersible design consisting of four steel columns stabilized by buoyancy and mooring lines. The tower is constructed from a highly stiff isotropic steel tube, and its bending frequencies are outside of the 1P and 3P frequencies, where the cross sections and thickness of the tower vary along its length. The National Renewable Energy Laboratory (NREL) Reference Open Source Controller (ROSCO) is used with the wind turbine, with a minimum rotor speed of 5 rpm and a rated rotor speed of 7.55 rpm. When operating in the design tip speed ratio (TSR = 9.0) in region 2, the blade pitch angle is zero, illustrated in Figure 2.7. The wind turbine is illustrated in Figure 3.1.

Figure 3.1: Visual presentation of the floating offshore wind turbine reference [4].

3.1.1 Substructure Properties

This section introduces the properties of the UMaine VolturnUS-S substructure. Figure 3.2 illustrates the top and side views of the entire wind turbine with the main dimensions. The floater consists of a submerged star-shaped pontoon made of steel. The arrangement of the hull comprises three buoyant columns spaced 51.75 m from the center of a fourth buoyant column. The central column is connected to the three outer columns with three 15.5x7.0 m^2 rectangular pontoons at the

bottom and three struts with a diameter of 0.9 m attached at the bottom and top of the buoyant columns. The interface between the floater and the tower is positioned on top of a fourth buoyant column located in the center of the surge-sway plane. The draft of the substructure is 20 m.

The total mass of the platform (on station) is 17,854 tons, where 3,914 tons is structural steel, 2,540 tons is fixed iron-ore-concrete ballast placed at the bottom of the three outer columns, and 11,300 tons is seawater ballast that floods the submerged pontoons. The properties are listed in Table 3.1. The design parameters for the floater have not been specified, and have been calculated with regard to the given parameters in the report of Umaine VolturnUS-S [4], also given in Table 3.1. The thickness and mass density of the floater has been in particular important for the thesis. Through calculations, the thickness was determined to be 44 mm, and the mass per unit length was found to be 67,884 kg/m. However, this weight includes the weight of stiffeners and welds. A further investigation was necessary to choose the thickness and mass density. The pontoons of the OC4 semi-submersible floater [74] have a thickness of 17.5 mm. A comparison of the decay test and fatigue analysis was performed to observe the influence of the different thicknesses, and it was concluded that a thickness of 17.5 mm is sufficient.

Parameter	Unit	Value
Hull displacement	[m^3]	20,206
Hull steel mass	[ton]	3,915
Tower Interface Mass	[ton]	100
Ballast mass (Fixed/fluid)	[ton]	2,540/11,300
Draft	[m]	20
Freeboard	[m]	15
Vertical Center of Gravity (VCG) from SWL	[m]	-14.94
Vertical Center of Buoyancy (VCB) from SWL	[m]	-13.63

Table 3.1: Semi-submersible platform properties [4]

(a) Top view　　　　　(b) Side view
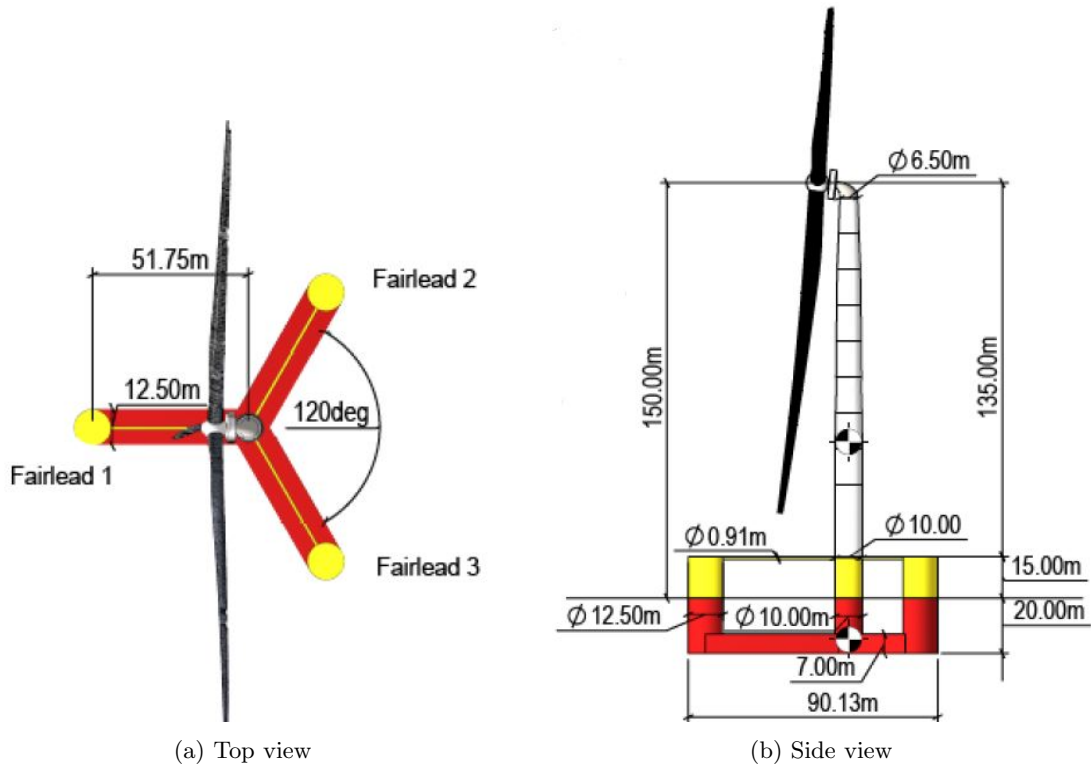
Figure 3.2: Top and side views of the reference wind turbine [4].

3.1.2 Mooring System Properties

This section will introduce the properties of the UMaine VolturnUS-S mooring system. The mooring system consists of three chain catenary lines with a length of 850 m. Each catenary line is connected to the fairlead at 14 m below sea water level (SWL) on one of the three columns on the floater. The lines use a studless R3 chain with a nominal diameter of 185 mm and are evenly spaced at 120 degrees in the surge-sway plane. The mooring line drag and added mass are selected with reference to DNV-RP-C203 [22] and DNV-OS-301 [75]. The properties of the mooring system are given in Table 3.2, and the layout of the mooring system is illustrated in Figure 3.3.

Parameter	Unit	Value
Mooring system type	[-]	Chain Catenary
Line type	[-]	R3 Studless mooring chain
Line breaking strength	[kN]	22,286
Anchor depth (from SWL)	[m]	200
Fairlead Depth (from SWL)	[m]	14
Anchor radial spacing	[m]	837.6
Fairlead radial spacing	[m]	58
Nominal chain diameter	[mm]	185
Extensional stiffness	[MN]	3270
Line unstreched length	[m]	850
Fairlead pretension	[kN]	2,437

Table 3.2: Mooring system properties [4]

(a) Top view
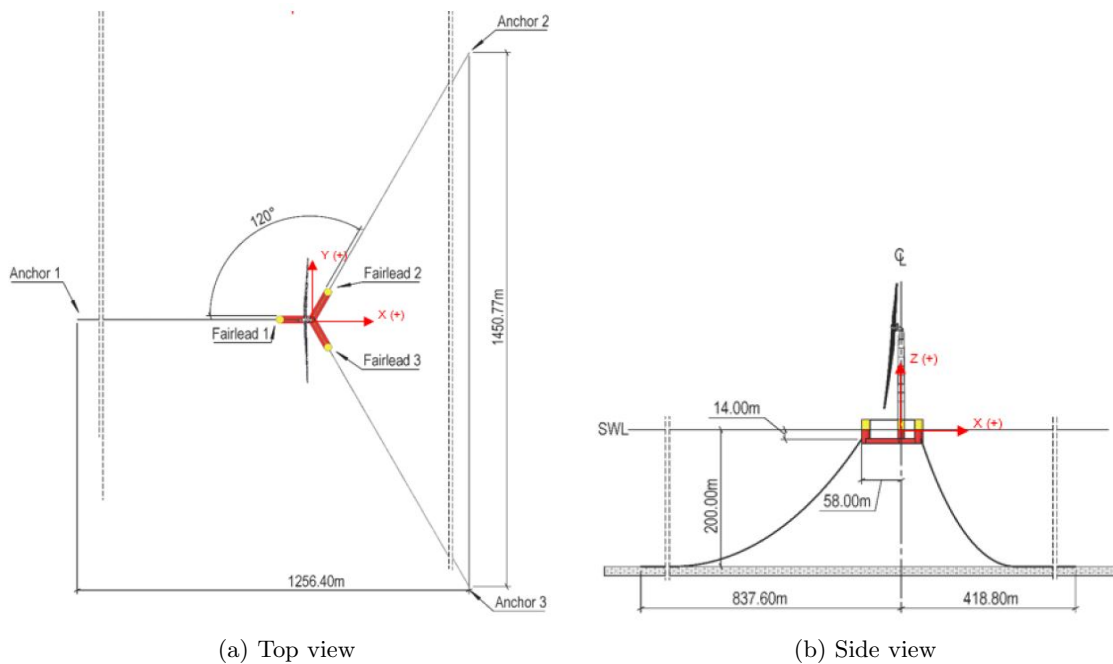
(b) Side view

Figure 3.3: Top view and side view of the mooring system [4].

3.1.3   Tower Properties

This section will introduce the UMaine VolturnUS-S tower properties. The tower is designed as an isotropic steel tube with free-free boundary conditions. The most important design constraints on the tower are the frequencies. To avoid potential tower resonance, the fore-aft and side-side natural frequencies must be outside rotation speed (1P) and blade passing (3P) ranges. The tower is designed to have a maximum outer diameter of 10 m and a 6.5 m tower-top diameter, interfacing with the existing nacelle bedplate design. The properties of the floating wind turbine tower are given in Table 3.3, and the dimensions of the tower vary as a function of height, presented in Table 3.4.

Parameter	Unit	Value
Mass	[ton]	1,263
Length	[m]	129.495
Base outer diameter	[m]	10
Top outer diameter	[m]	6.5
1st fore-aft bending mode	[Hz]	0.496
1st side-side bending mode	[Hz]	0.483
Youngs modulus	[Pa]	200e11
Shear modulus	[Pa]	793e10
Density	[kg/m^3]	785e3

Table 3.3: Floating Tower Properties [4]

Height [m]	Outer diameter [m]	Thickness [mm]
15.000	10.000	82.954
28.000	9.964	82.954
28.001	9.964	83.073
41.000	9.967	83.073
41.001	9.967	82.799
54.000	9.927	82.799
54.001	9.927	29.900
67.000	9.528	29.900
67.001	9.528	27.842
80.000	9.149	27.842
80.001	9.149	25.567
93.000	8.945	25.567
93.001	8.945	22.854
106.000	8.735	22.854
106.001	8.735	20.250
119.000	8.405	20.250
119.001	8.405	18.339
132.000	7.321	18.339
132.001	7.321	21.211
144.582	6.500	21.211

Table 3.4: Tower dimensions [4]

3.2 Environmental Condition

The met-ocean conditions and seabed characteristics influence the design of marine structures. Their definition is an essential part of analyzing the performance of the wind turbine in a realistic range of operating parameters. In the Lifes50+ project, three sets of environmental parameters for moderate, medium, and severe met-ocean conditions are provided for analysis [21]. The selected areas are as follows:

- Site A (moderate met-ocean conditions), offshore of Golfe de Fos, France

- Site B (medium met-ocean conditions), the Gulf of Maine, United States of America

- Site C (severe met-ocean conditions), West of the Isle of Barra, Scotland

Table 3.5 summarizes the proposed 50-year return period met-ocean conditions for the three sites. The chosen site in this thesis is the medium met-ocean conditions at the Gulf of Maine outside the U.S.

	Wind hub height	H_s	T_p	Current	Extreme water level	Soil
Site A	37	7.5	8-11	0.9	1.13	Sand/clay
Site B	44	10.9	9-16	1.13	4.3	Sand/clay
Site C	50	15.6	12-18	1.82	4.2	Basalt

Table 3.5: 50-year return period met-ocean conditions [21]
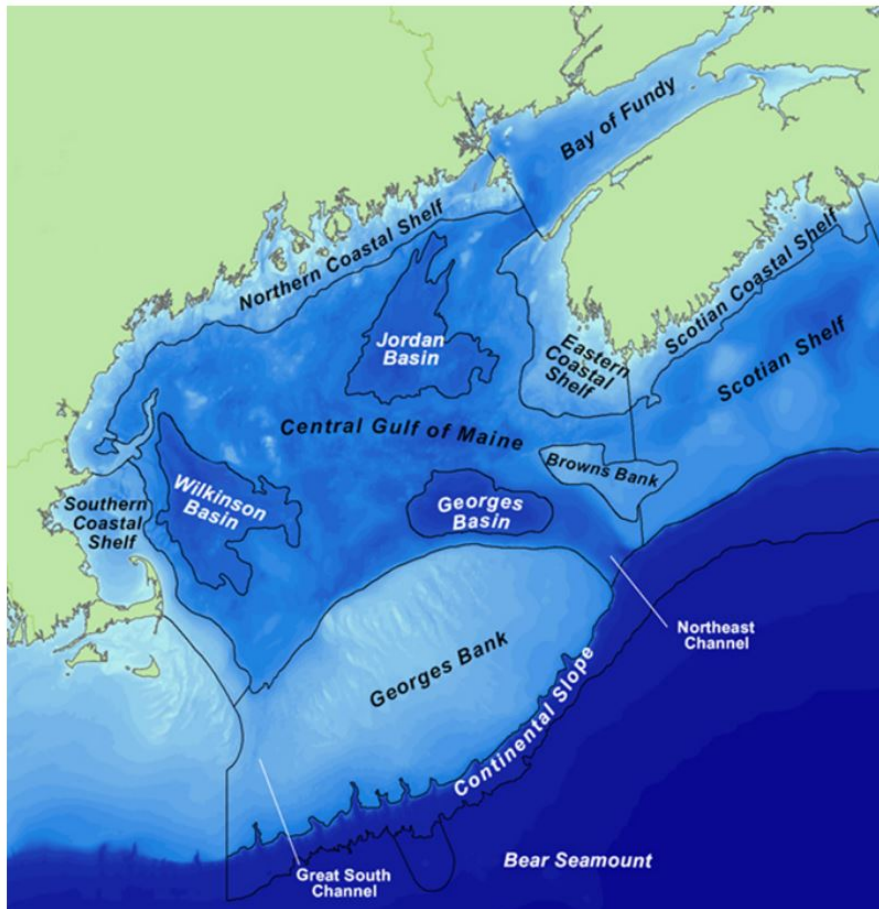
Figure 3.4: Map presentation of the Gulf of Maine site location [19]

The applied site for this thesis is site B: The Gulf of Maine, United States of America. The location of the site is observed in Figure 3.4. The site was selected as a part of a project to investigate the market of renewable energies in the U.S. [21]. There are three measurement buoys close to the site. The mean water depth is 130 m, with a maximum of 150 m. There are no data on wind velocity, but a power law profile with a power law coefficient of 0.14 has been found to be adequate for the site.

The wind environment can be categorized as 'normal' under the IEC 6400-1 standard. The wind speed profile follows a typical profile for standard wind turbine classes, and it is modeled using a power law. The power-law exponent is assumed to be 0.14. A normal turbulence model (NTM) is assumed for the wind turbine, whereas the standard deviation and turbulence intensity is illustrated for the wind speed at the hub height in Figure 3.5. The three classes A, B, and C, are further explained in Section 3.3.

For fatigue analysis, a smaller range of peak periods (T_p) and significant wave heights (H_s) in Figure 3.6 was chosen for the analysis in this project. The peak period varies from 4.5 s to 9.5 s, and the significant wave height varies from 0.5 m to 2.5 m. This has been chosen as these are the most probable conditions that are more likely to contribute to fatigue damage with time. The mean wind speeds have been selected from Figure 3.7, with the same mindset. For the same significant wave heights, the wind velocity varies from 4 m/s to 12 m/s. For all cases, the waves and wind are coming from a 0° direction, with no current.

(a) Turbulence standard deviation   (b) Turbulence intensity
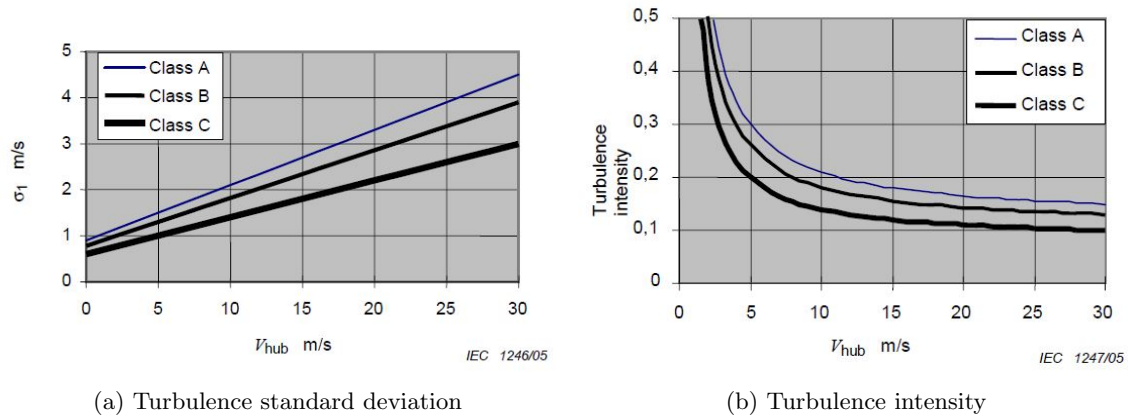
Figure 3.5: Standard deviation and turbulence intensity for the normal turbulence model (NTM) [20]

	Tp (s)								
	1<Tp<2	2<Tp<3	3<Tp<4	4<Tp<5	5<Tp<6	6<Tp<7	7<Tp<9	9<Tp<11	Tp>11
<1	0,03%	4,69%	7,29%	7,02%	3,91%	5,91%	13,49%	6,27%	0,08%
1< Hs <2		0,00%	0,92%	6,64%	6,85%	7,32%	7,90%	8,36%	0,16%
2< Hs <3			0,00%	0,09%	0,55%	2,71%	2,91%	3,31%	0,15%
3< Hs <4				0,00%	0,01%	0,12%	1,11%	1,04%	0,08%
4< Hs <5						0,00%	0,19%	0,47%	0,04%
5< Hs <6							0,02%	0,21%	0,01%
6< Hs <7								0,08%	0,01%
7< Hs <8								0,02%	0,01%
Hs >8								0,00%	0,00%

Significant Wave Height [m] (row header, left side)

Figure 3.6: Significant wave height - peak period distribution [21]

	Significant Wave Height [m]								
	Hs <1	1< Hs <2	2< Hs <3	3< Hs <4	4< Hs <5	5< Hs <6	6< Hs <7	7< Hs <8	Hs >8
u₁₀<1	681	410	59	14	8				
1< u₁₀<2	3174	2291	401	84	24	6	5	1	
2< u₁₀<3	5501	4003	726	162	73	7	4		
3< u₁₀<4	6043	4515	851	197	79	26	3		1
4< u₁₀<5	5887	4867	894	260	101	36	8	1	
5< u₁₀<6	5376	5073	1057	256	110	48	19	9	
6< u₁₀<7	4094	4633	1147	339	130	43	10	5	4
7< u₁₀<8	2945	5064	1276	500	147	38	17	4	3
8< u₁₀<9	1694	4745	1623	496	163	63	9	3	2
9< u₁₀<10	1121	4120	1843	506	162	47	31		1
10< u₁₀<11	687	3216	1956	570	151	47	33	5	2
11< u₁₀<12	441	2018	1933	564	142	51	24	6	
12< u₁₀<13	321	1181	1762	680	185	69	18	6	
13< u₁₀<14	189	617	1311	706	196	53	11	2	2
14< u₁₀<15	142	310	676	625	187	53	23	5	1
15< u₁₀<16	90	187	381	507	209	76	28	8	3
16< u₁₀<17	67	92	132	332	207	70	19	8	5
17< u₁₀<18	51	68	55	157	188	72	20	5	
18< u₁₀<19	43	34	26	52	97	53	28	8	8
19< u₁₀<20	12	22	7	15	31	44	19	9	4
20< u₁₀ᵢₙ <21	4	3	2	3	18	23	15	13	8
21< u₁₀<22	4	3			6	11	7	4	1
u₁₀>22	4	5	1		2	6	9	4	12

Wind Speed at 10m [m/s] (row header, left side)

Figure 3.7: The distribution of 10-minute wind speeds at a 10-meter significant wave height [21]

3.3 Design Standards for FOWT

This section provides an overview of the relevant design standards for offshore wind turbines. Det Norske Veritas (DNV) organization has published several design standards for offshore wind turbines, including DNV-OS-J101 (Design of Offshore Wind Turbine Structures) [68] and DNV-OS-J103 (Design of Floating Wind Turbine System) [76]. These standards provide guidance, technical requirements, and principles for the design, construction, and in-service inspection of the support structures and station-keeping systems of offshore and floating wind turbines. DNV-OS-J103 covers the structural design of floating wind turbine structures, including transportation, installation, and inspection. While DNV-OS-J101 is the design standard for bottom fixed wind turbines, DNV-OS-J103 is the corresponding standard for floating offshore wind turbines. DNV-ST-0119 covers the structural design of the floater motion control system and the control system for the wind turbine [77].

Other relevant design standards include DNV-RP-C203 (Fatigue design of offshore steel structures) [22] and DNV-RP-C205 (Environmental conditions and environmental loads) [64]. DNV-RP-C203 provides recommendations for conducting fatigue analyses based on fatigue tests and fracture mechanics. These recommendations aim to ensure an adequate fatigue life for a structure, taking into account efficient inspection programs during fabrication and operational life. Each structure member subjected to detailed fatigue assessment should be evaluated to ensure the structure can fulfill its intended function. DNV-RP-C205 provides guidance for modeling, analyzing, and predicting environmental conditions and calculating the environmental loads acting on a structure, limited to wave, wind, and current loads.

IEC 61400 is a series of international standards developed by the International Electrotechnical Commission (IEC) that provide guidelines and requirements for designing, manufacturing, and testing wind turbines. The standards cover various aspects of wind turbines, including structural design, electrical systems, safety, and performance.

The IEC 61400 series includes several parts, each addressing different aspects of wind turbine design and operation. Some of the important parts of the standard include:

- IEC 61400-1: General requirements: This part specifies general requirements for wind turbines, including design load cases, safety requirements, and performance tests [20].

- IEC 61400-2: Design requirements for small wind turbines: This part provides specific design requirements for small wind turbines with a rotor-swept area less than or equal to 200 m^2 [78].

- IEC 61400-3: Design requirements for offshore wind turbines: This part provides specific design requirements for wind turbines installed offshore [79].

The IEC 61400-1 standard was used to generate wind files in TurbSim alongside DNV-RP-C205. The IEC is specified by DNV to be used if there are no other DNV standards that apply to the situation [76]. Figure 3.8 illustrates the three classes of wind turbines according to the IEC 61400-1 standard [20].

Wind turbine class		I	II	III	S
V_{ref}	(m/s)	50	42,5	37,5	Values
A	I_{ref} (-)		0,16		specified
B	I_{ref} (-)		0,14		by the
C	I_{ref} (-)		0,12		designer

Figure 3.8: Basic parameters for wind turbine classes according to the IEC 61400-1 standard [20]

3.3.1 Parameters for Calculation of Accumulated Fatigue Damage

The fatigue damage of the tower base is calculated using the method outlined in the DNV-RP-C203 standard. Welds in the tower base have been assigned a detail category of D, as described in the Appendix of the standard. The S-N curve and the corresponding fatigue parameters used in the analysis are also taken from the standard. The corresponding values for the tower base are found in Table 3.6. Meanwhile, the corresponding values for the pontoon are found in Table 3.7. The related S-N curves are illustrated in Figure 3.9 and Figure 3.10. Since the tower base is located in an air environment, the S-N curve for that environment is used, and an S-N curve in seawater with cathodic protection is used for the pontoons. This method allows for a consistent and standardized calculation of fatigue damage in the tower base using established guidelines and parameters.

N $\leq 10^7$ Cycles		N $> 10^7$ Cycles		Fatigue limit at 10^7 cycles	k	t_{ref}	S-N curve [22]
m	$\log(\bar{a})$	m	$\log(\bar{a})$	[MPa]	[-]	[m]	
3.0	12.164	5.0	15.606	52.63	0.2	0.025	2-1, D

Table 3.6: S-N curve parameters of the tower base cross section [22].

N $\leq 10^6$ Cycles		N $> 10^6$ Cycles		Fatigue limit at 10^7 cycles	k	t_{ref}	S-N curve [22]
m	$\log(\bar{a})$	m	$\log(\bar{a})$	[MPa]	[-]	[m]	
3.0	11.764	5.0	15.606	52.63	0.2	0.025	2-2, D

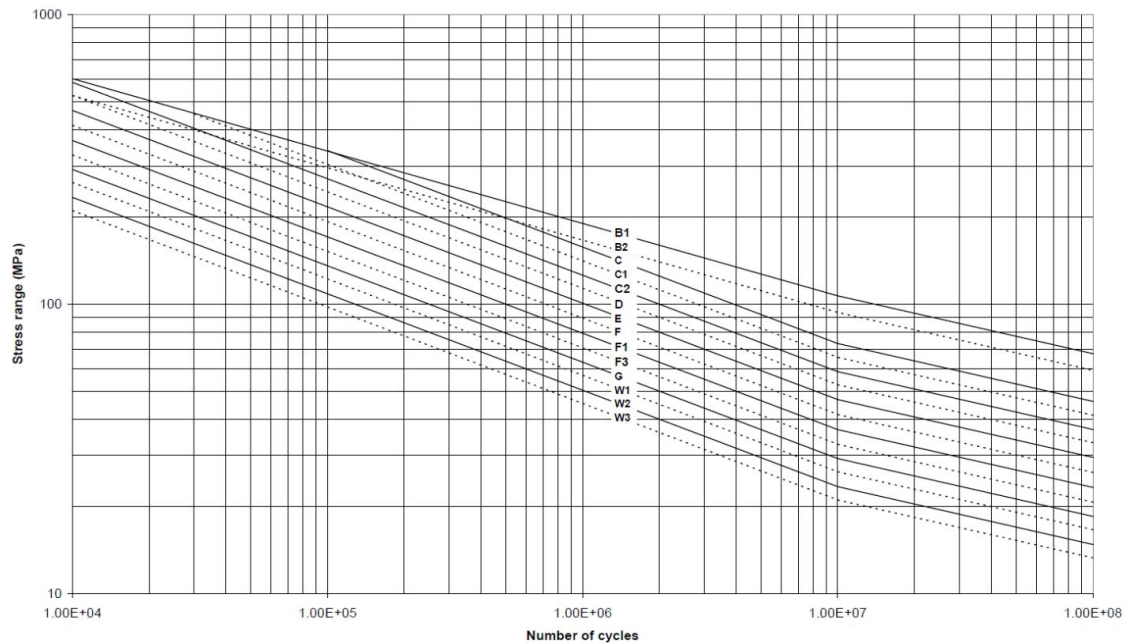Table 3.7: S-N curve parameters of the pontoon cross sections [22].

Figure 3.9: S-N curves in for structures in air-environments [22]

46
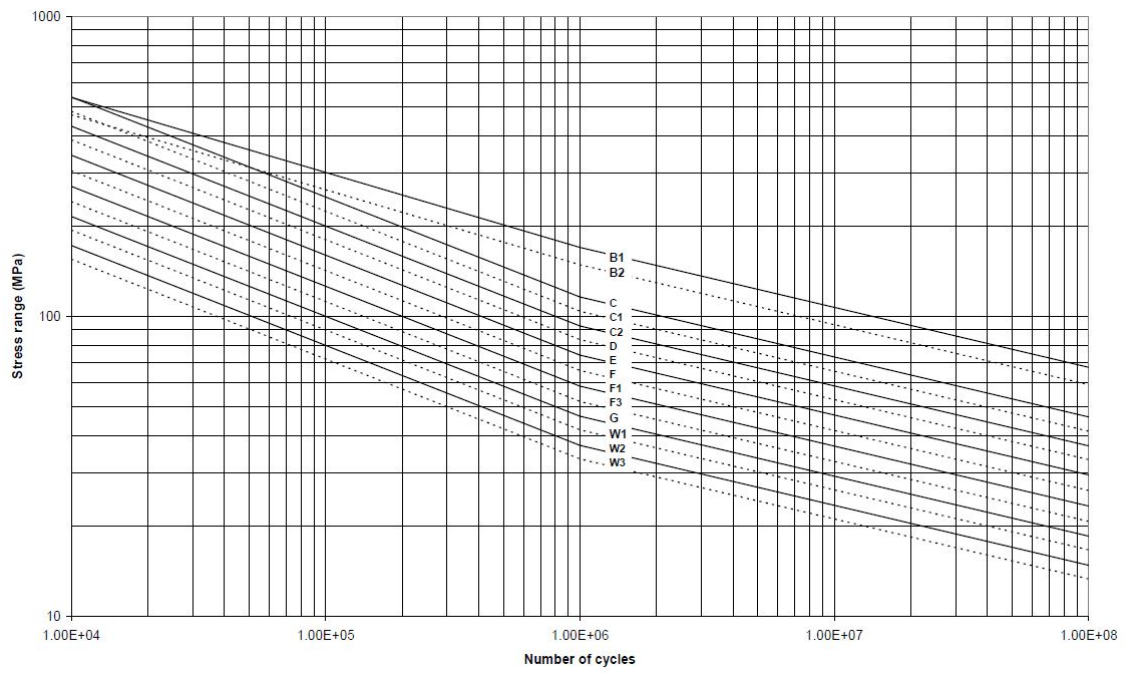
Figure 3.10: S-N curves in for structures with cathodic protection in seawater-environment [22]

Chapter 4

Modeling and Analysis Method

This thesis investigates the response due to waves and wind actions for a combined fully coupled analysis. This chapter will explain the method in detail and how different software is implemented. The model presented is based on the 15 MW UMaine VolturnUS reference wind turbine introduced in chapter 3. The environmental conditions are based on the Lifes50+ project [21].

4.1   Method Overview

In this project, a fully coupled analysis is performed to investigate the effect of waves and wind on a wind turbine. The SIMA computer program is applied in order to investigate these studies. Fully coupled analysis refers to an analysis that takes into account hydro-aero-servo-elastic coupling. This means that the entire structure, including the mooring lines, the floater, the tower, and the rotor-nacelle assembly (RNA), is considered in the analysis. SIMA calculates global floating motions, global floating loads, and aerodynamic loads.

The mooring lines are modeled as SIMO catenary lines or RIFLEX elements for different analyses, which is further explained in Section 4.4. The cross sections in the tower are modeled as RIFLEX finite elements. The floater is modeled as a SIMO body, which means that it is treated as a six-degree-of-freedom (6DOF) body with 6x6 matrices of hydrodynamic coefficients. However, a modified wind turbine model is also implemented. This uses the slender system theory for the pontoon, with rigid body mechanics. This still includes the 6DOF hydrodynamic coefficients.

The substructure is first modeled as a rigid body, and the time domain equation of motion can be solved. By using the potential flow solver Wadam in HydroD, the mass matrix ($\mathbf{M}$), added mass matrix ($\mathbf{A}$), hydrostatic stiffness matrix ($\mathbf{C}$), wave radiation damping matrix ($\mathbf{B}$) and the excitation force vector ($\vec{F}$) is found. To obtain the correct hydrodynamic coefficients, these matrices are unchanged for the modified model in SIMA. The main changes are done to the structural properties, and the hydrodynamic effects stay the same. This is for SIMO to do the hydrodynamic calculations correctly and RIFLEX to do the structural loads and response calculations accurately.

Several types of models are needed to analyze using the DNV potential flow solver, Wadam. This includes a mass model for determining mass properties and generating the mass matrix $\mathbf{M}$ and a panel model representing the structure's outer surface. Panel methods are used to calculate the pressure on each panel, which is essential for obtaining the hydrodynamic pressure distribution across the structure. Integration of this distribution yields hydrodynamic coefficients used in the equation of motion. Other models, such as structural, Morison, and compartment models, can also be utilized.

The DNV Software GeniE was used to create models for analysis in Wadam. The models include panel, mass, Morison, and compartment, which are explained in detail in subsequent sections. The data files for these hydro models are typically named T-files, following the convention T*.FEM,

where the * is a unique number for each hydro model.

An attempt was made to use the DNV Sesam Wind Manager to do a local analysis. A Wasim file from HydroD was necessary to use this software, which required a .pln-file. However, this turned out to be more time-consuming than expected. The attempt and further discussions are in Section A.1.

The workflow of this thesis is presented in Figure 4.1. The first step involves obtaining wind and wave data for the wind-sea conditions. Further, the wind conditions are utilized in SIMA to generate a turbulent wind file, which is then combined with the wind turbine module. The RIFLEX-elements can be directly modeled in SIMA using the model information. The model information is also used to create a model in GeniE, which is further implemented into HydroD. These models and the wave spectrum are implemented in the SIMO module of SIMA. The simulations in SIMA provide outputs of forces and moments acting on the structure. These outputs are post-processed to determine the nominal stress, and the fatigue damage is found using the DNV standard.
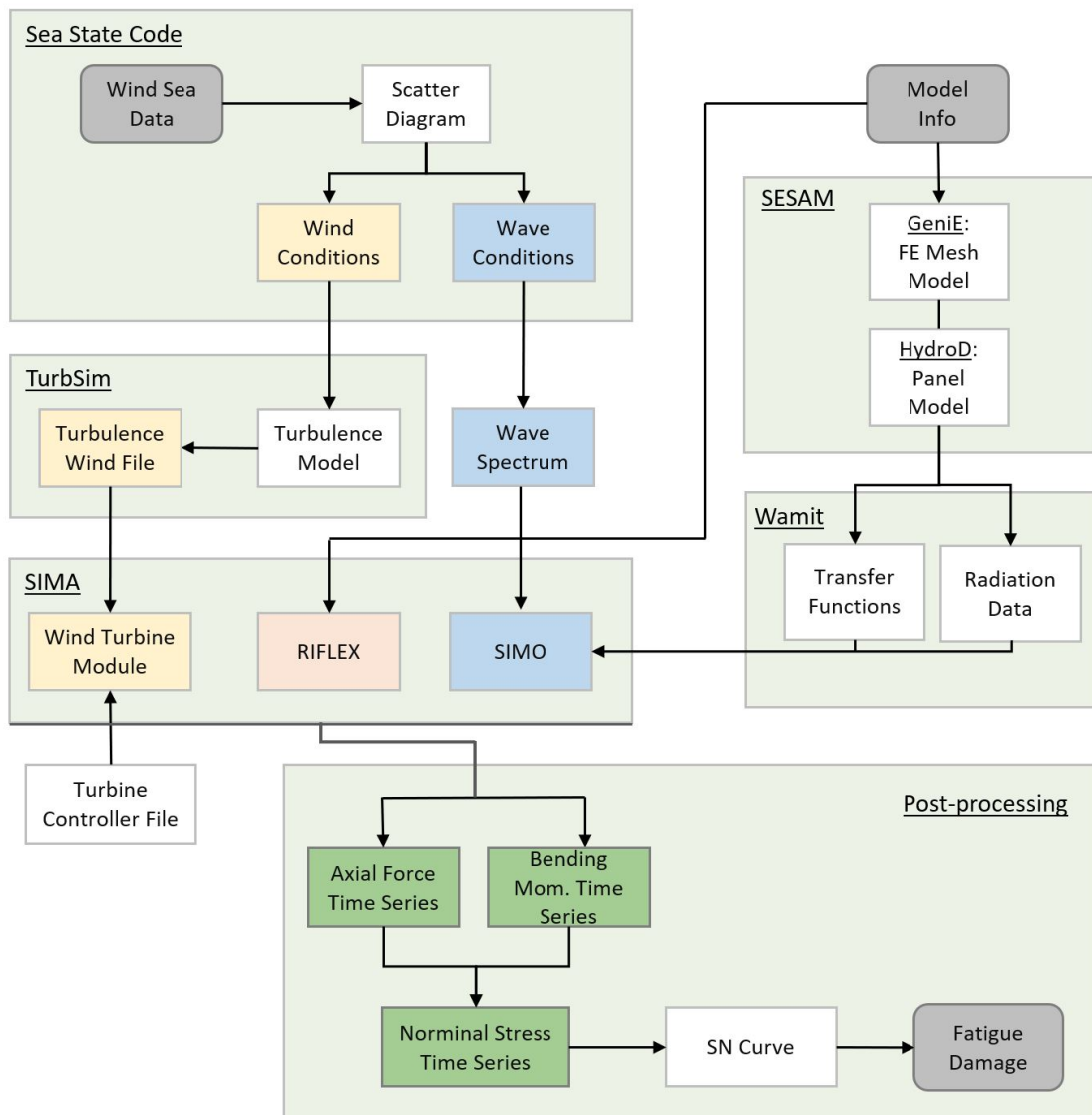
Figure 4.1: Methodology flowchart used in this thesis

4.2 GeniE

The DNV Software GeniE was used to create models for Wadam analysis in HydroD. This includes panel-, mass-, compartment- and Morison models. These models are created and meshed directly in SIMA. The structure is modeled according to the parameters given in the NREL technical report [4] and the parameters found analytically in chapter 3. The floater is simplified and modeled using a thickness to include stiffeners and flanges, with the weight specified in the report. The model contains compartments, simplified with a compartment for each segment.

The GeniE models are meshed using the meshing command, whereas the models have been meshed using a mesh density of 1m. A common rule is to require a minimum of six elements per wavelength [3]. Then, the models are exported as T*.FEM files. The meshed models for both the Rigid and Modified WT models can be found in Figure 4.2. A T*.FEM file is imported into HydroD to extract hydrodynamic and static parameters using the frequency domain analysis in Wadam. The Modified WT is found in Figure 4.2b, and illustrates how the SIMO-bodies are modeled. The flexible pontoons are modeled as RIFLEX-elements between each of these columns in SIMA.

(a) Meshed Rigid WT   (b) Meshed Modified WT
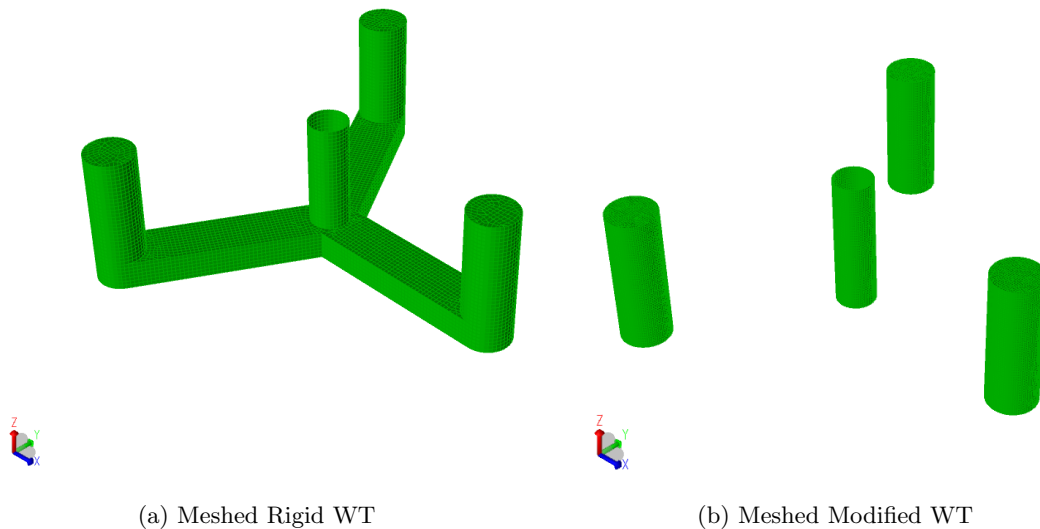
Figure 4.2: The models in GeniE meshed with a mesh size of 1 meter

4.2.1 Mass- and Compartment Models

The mass- and compartments models are created for analysis in HydroD. While these models can be made as separate entities, they could be represented in the same FEM file in this case. The mass model specifically represents the mass of the model without the influence of the compartments and represents the fixed weight of the structure. Contrary, the compartments model focuses on the ballast weight and does not consider the mass of the structure. Together they determine the balanced center of gravity COG and the draft of the system and compute the 6DOF mass matrix to be applied in the motion analysis. The compartments model is simplified, as illustrated in Figure 4.3b, and the weight of the rest of the wind turbine is modeled using a point mass as described in Figure 4.3a. However, the complete mass model combining the ballast and fixed weight is modeled using two approaches in HydroD. The first approach is to use the mass and compartment models and to use the balance option in HydroD to find the COG. The other approach is to use the 'User defined' option to create a mass model. This is further explained in Section 4.3.

The properties used to model the mass models are listed in Table 4.1. It is important to note that the equivalent thickness in the table includes the total fixed steel mass of the plates, flanges, stiffeners, etc., while the actual thickness is found to be 17.5 mm.

Property	Unit	Value
Density, steel	[kg/m^3]	7850
Density, ballast water	[kg/m^3]	1025
Thickness	[mm]	44
Mesh size	[m]	1
Point mass	[tons]	2254

Table 4.1: Important properties for the modeling of mass models

(a) Mass model with a point mass

(b) Compartment model
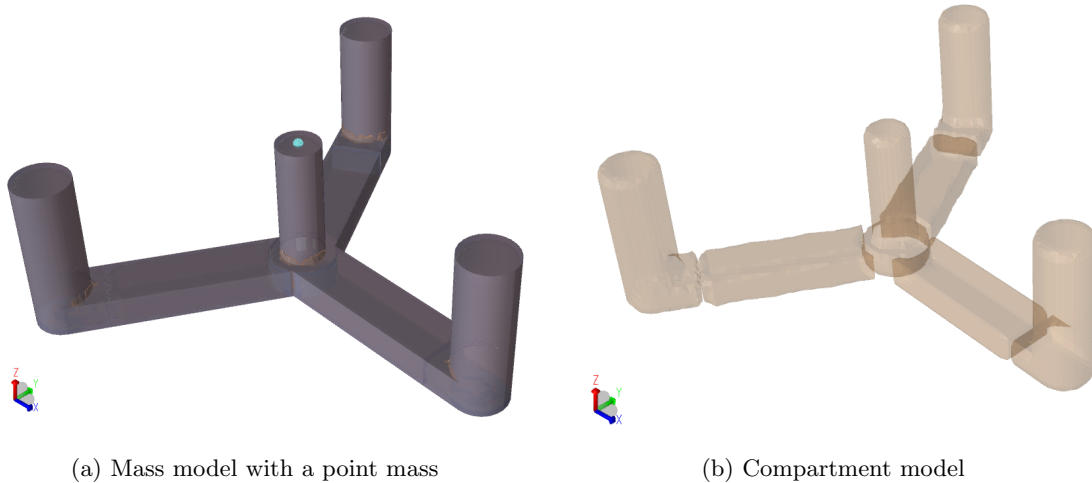
Figure 4.3: Mass- and compartment models in GeniE

4.2.2 The Morison Model

To simulate the drag loads on the structure, a Morison model is required. The Morison model is created using the '*Sections*' tool in GeniE. Here, the columns are represented as pipes and the pontoons as boxes. The model represents the submerged part of the floater. In HydroD, the Morison model corresponds to the slender system formulation utilized in SIMA. The Morison model in GeniE with the corresponding model in HydroD is illustrated in Figure 4.4.

(a) Morison model in GeniE

(b) Morison model in HydroD
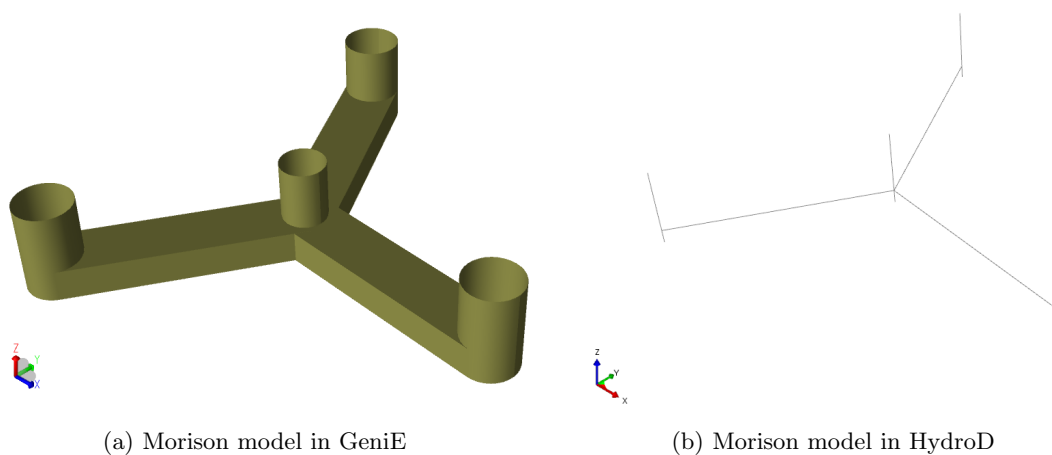
Figure 4.4: Morison models, both from GeniE and HydroD

4.3 HydroD

HydroD is used for linear frequency domain analysis in Wadam. It is utilized to find the mass matrix $\mathbf{M}$, the hydrostatic stiffness matrix $\mathbf{C}$, the added mass dependent on frequency $\mathbf{A}(\omega)$, the damping of frequency-dependent waves radiation $\mathbf{B}(\omega)$ and the excitation forces $\vec{F}_{exc}(\omega)$. In order to obtain these parameters, the mass-, panel- and Morison model created in GeniE was imported. The extended mass model combining the compartment model with the mass model gave unsatisfying results, likely due to inaccurate implementations of the COG of the mass of the RNA and tower. As a solution, three separate mass models were created using the '*User defined*' option in HydroD. The user-defined mass models include both steel mass and potentially ballast weight. They accurately represent the contribution of the mass and compartments model, providing an adequate means of modeling their effects. The results obtained from these models were satisfactory and were subsequently used for further implementation in SIMA and for validating the overall model. The complete model in HydroD with the panel model, the Morison model, the loading condition, and the mass models are illustrated in Figure 4.5.

The parameters found from the HydroD analysis were given as input to the floater representation in SIMA. The results were also used to plot RAOs in the frequency domain and compare them with the time domain as validation, and to observe other effects, such as added mass and excitation forces.
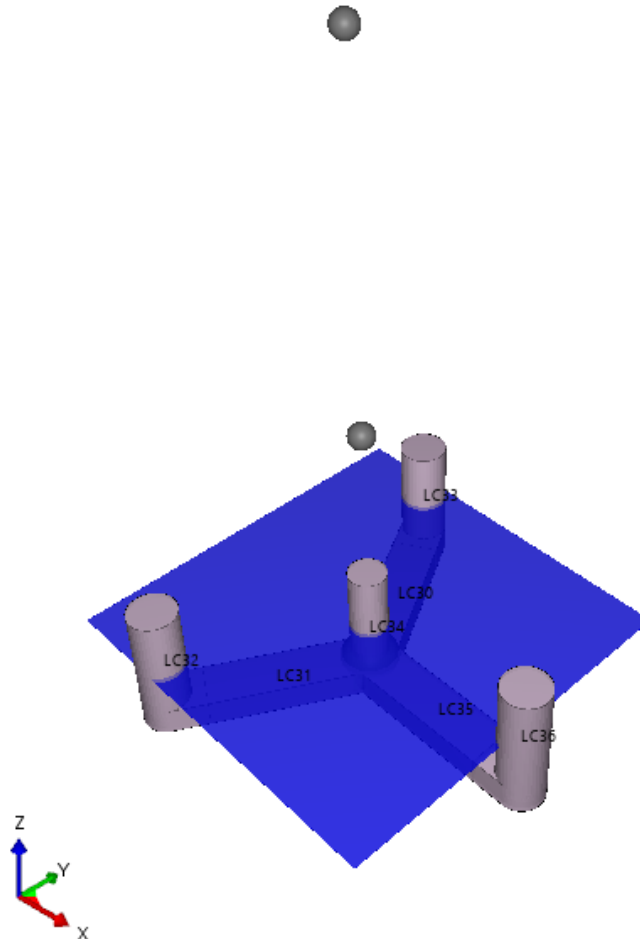
Figure 4.5: Complete model in HydroD, with loading condition, mass-, compartment- and panel model

4.4 SIMA and TurbSim

This project uses the SIMA software to conduct a fully coupled analysis of the effect of waves and wind on a wind turbine. The analysis considers the interaction between the hydrodynamic, aerodynamic, and structural behavior of the system. The SIMA model is made with a combination of SIMO bodies and RIFLEX-elements. The RIFLEX-elements use finite elements and consider the Morison loads. On the other hand, SIMO bodies are rigid bodies, and this is where the 6DOF hydrodynamic coefficients are implemented.

SIMA uses the Master-Slave method to reduce the degrees of freedom in the analysis. This involves connecting SIMO bodies with RIFLEX elements by implementing a slender system connection between the rigid SIMO bodies and dummy transitions.
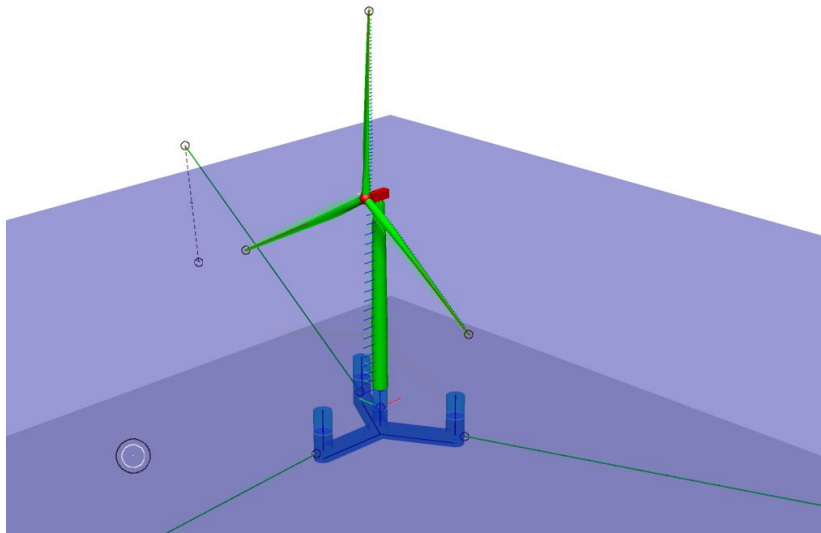
Figure 4.6: The Rigid WT modeled in SIMA
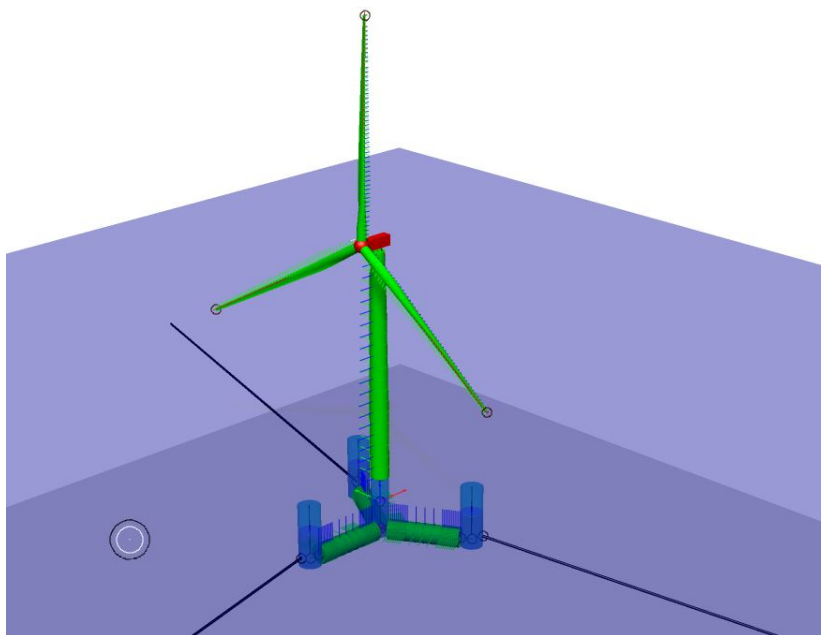
Figure 4.7: The Modified WT modeled in SIMA

The reference wind turbine is modeled using a single SIMO body for the floater [4], and is further referred to as Rigid WT. The hub and nacelle are also modeled using SIMO bodies. However, the blade lines, the blade eccentricities, the tower, shaft, and mooring lines are modeled as RIFLEX bodies. The shaft is represented as a two-segment line, with one segment representing the low-speed shaft and the other representing the high-speed shaft. The outline of how Rigid WT is modeled using different components is illustrated in Figure 4.8a, and the model in SIMA is found in Figure 4.6. The gray lines in the outline of the model represent the parts simulated as SIMO bodies, whereas the RIFLEX elements are black. Between the supernode 'sh_sn2' and 'towerup' there is a rigid supernode connection using the Master-Slave method. This applies to the 'towerlow' and 'dummy_transition' as well, with the last one being a Slave to the 'semi_loc'. Accordingly, the supernode follows the motions of the floater, establishing the connection between the SIMO and RIFLEX bodies.

(a) Rigid WT   (b) Modified WT
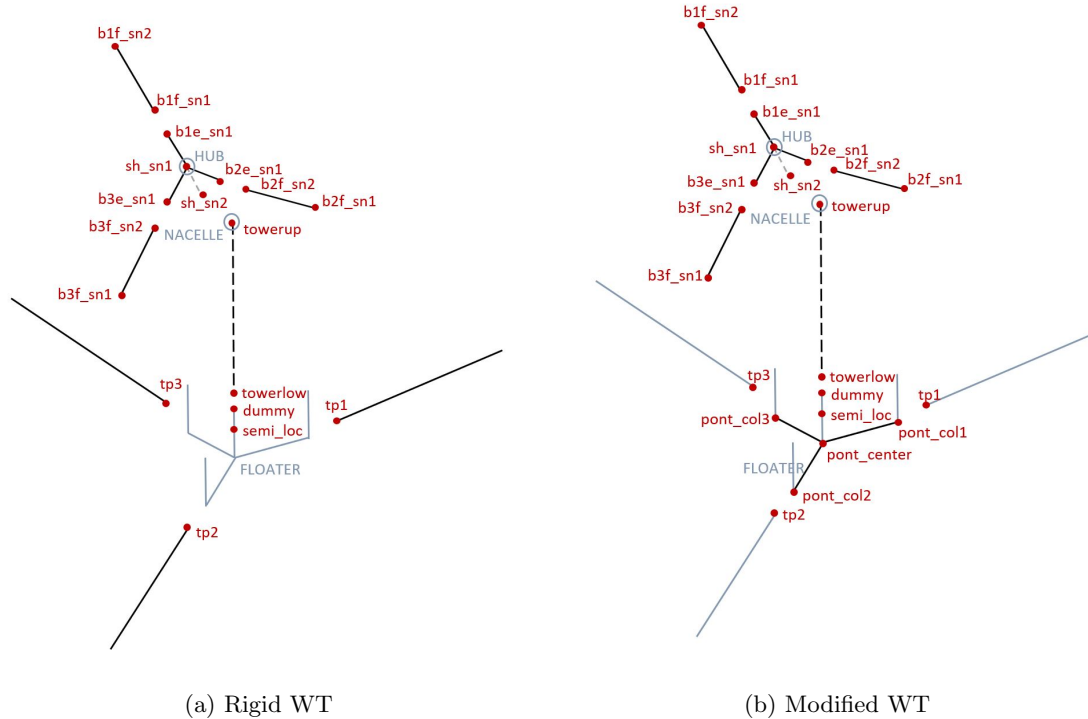
Figure 4.8: Schematic representation of wind turbine models in SIMA, inspired by Kvittem [13]

Modifications have been made to the model in order to create a more realistic representation of the wind turbine system, and this model is further referred to as Modified WT. These modifications include the use of RIFLEX elements for the pontoons on the floater, which allows for more accurate capturing of bending moments and forces in the pontoons. Additionally, SIMO bodies have been used for the mooring lines to reduce the simulation time and avoid additional dynamic effects from the lines. The software calculates a larger number of elements by simulating mooring lines using RIFLEX elements, which is time-consuming. SIMO bodies can be simulated using the catenary method, which treats the lines as quasi-static. The floater still contains the same hydrodynamic values as the Rigid WT with a floater entirely of a single SIMO body.

The Modified WT model is illustrated in Figure 4.7, and the adjustments made to the floater are illustrated in Figure 4.8b. It should be noted that the modifications to the floater are more significant than what is shown in the figure. To connect the SIMO and RIFLEX elements, dummy transitions have been implemented in all columns. Each column includes a center supernode and a supernode on the outer columns, which serve as connection points for the RIFLEX elements. The dummy transitions are connected through these supernodes and the center ones. Similar to the reference wind turbine model shown in Figure 4.6, Master-Slave connections are present. To maintain the floater as a unified body after the modifications, the new supernodes are configured as Slaves to 'semi_loc'. This ensures that the floater remains unified and the motions of the system

are accurately represented.

The floater is modeled using multiple rigid bodies for the columns connected by flexible beams for the pontoons. The hydrostatic and hydrodynamic loads on each body are calculated assuming one-body hydrodynamics for the entire floater. These external, gravitational, and inertial loads are integrated into a beam-based finite element model of the floater to perform a time-domain analysis. Each pontoon is modeled using four segments, whereas the two segments closest to the columns contain ten elements, and the segments in the middle use two elements. The forces are gathered from the second elements from both sides to avoid immense bending moments that can occur with a rigid/flexible body interaction. This number of elements was found to give good results. The distribution of elements and segments is illustrated in Figure 4.9. In this figure, each line is a new element.
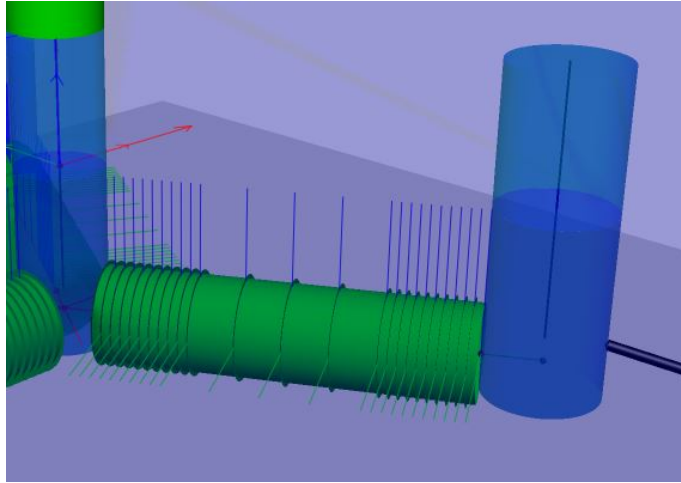
Figure 4.9: Distribution of elements on the pontoons of the Modified WT

There are several ways to include the buoyancy of the floater in the analysis accurately. This depends on if the 'Gravity Included' is checked off. If this option is checked off, SIMA assumes that the buoyancy forces are equal to the mass of the floater [3]. This results in incorrect results, as the buoyancy must also account for the tower, RNA, and vertical pretension at the fairlead and the substructure. In this study, the 'Gravity Included' option is disabled, and an external force is included to achieve a correct buoyancy force. The total buoyancy force is compensated by force with a magnitude of 2.041e8 N. This is equal to the buoyancy of the floater and the rest of the structure. The mass of the RNA and the tower is given. Meanwhile, the mass of the mooring lines must be found. The vertical pretension of the mooring lines is found using the method introduced by Fredrik Haaland in his Master Thesis [3]. It was found that the pretension could be found by running a static analysis, finding the length of the mooring lines touching the ground, and multiplying the mass coefficient with the respective length.

To calculate the fatigue damage accumulated during 1 hour, simulations were performed for a duration of 5500 s with a time step of 0.05 s. The first 1900s were excluded in the post-processing to minimize the impact of potential errors from the start-up conditions. The time step is chosen to include smaller variations in the bending moments and get more accurate results. The simulations are conducted using one wave seed and one wind seed, referring to the findings in the Master thesis of Yu Ma [54]. It was found that one seed is enough to get good results for FLS. A more significant number of seeds is required to analyze the response corresponding to the ULS limit state. The turbulent wind simulated using TurbSim contains 50 seeds. This is done to create an adequate representation of the turbulent wind. Further investigation of the sensitivity of timestep, elements in the pontoon, and seeds are discussed in Section 5.7.

4.4.1 System Identification

Decay tests are a method to observe the 6DOF motions of the structure and can present relevant information on the damping of the structure. The decay test is a good approach for coupled models but works best for rigid body motions. It is not able to capture all frequencies, such as tower frequencies and other motions, as the eigenvalue analysis is capable of capturing. The environmental values are set to a high period and low wind speed and wave height to perform the decay test. This ensures that the wind turbine is not affected by environmental conditions during decay tests. Additionally, the wind turbine is parked with the twist angle of the blades set to feather. The BEMT method in SIMA is not suitable for parked wind turbines, so the induction factor is turned off in SIMA for these tests [15]. The decay tests are conducted with a ramp-up time of 100 s, followed by a constant force for 100 s, after which the structure can freely evolve. This is illustrated in Figure 4.10.
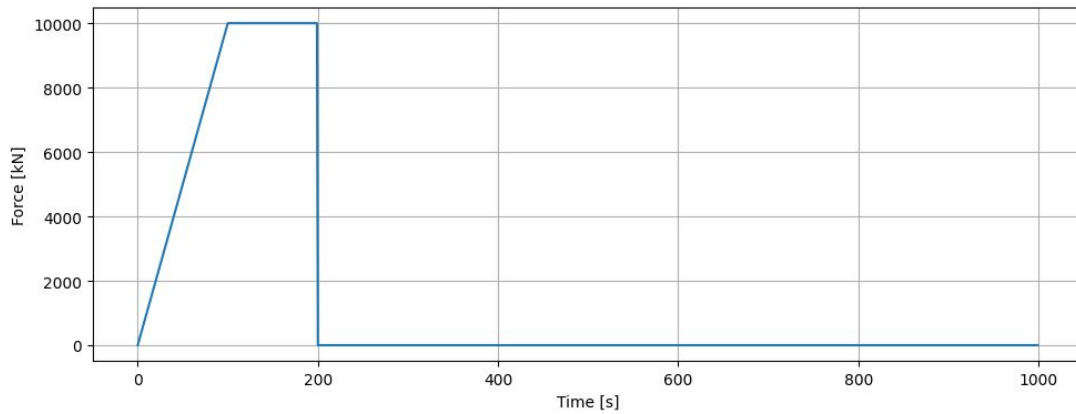
Figure 4.10: An illustration of ramp-up time and constant force as a series of time

By conducting an eigenvalue analysis, the flexibility of the model is observable. To conduct an eigenvalue analysis, the blades, shaft, and nacelle are removed and replaced with mass in the floater, as the eigenvalue analysis is not recommended with coupled models. Removing parts of the structure without any interest decreases the influence of the coupled model. The mass kinetics of the floater is increased to achieve the correct COG and motions of the Modified WT. The eigenvalue model in SIMA is illustrated in Figure 4.11
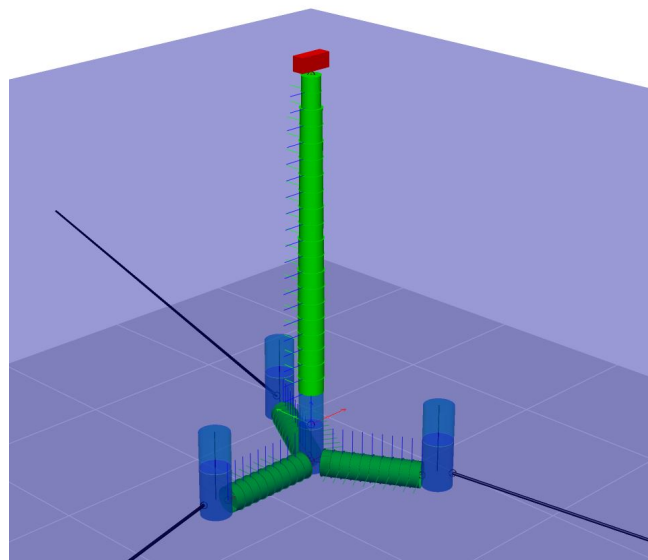
Figure 4.11: Modified WT model for eigenvalue analysis

White noise simulations are another method to observe the dynamic behavior and response of the structure. The white noise wave spectrum is created for small waves for a wide range of frequencies. The response can be analyzed to determine characteristics, such as power specter density and transfer functions. In this thesis, 100 different simulations have been conducted with a wave height of 0.1 m and periods from 3 s to 50 s. The mean of the peaks is found and normalized on the wave heights, which together provide the RAOs of the structure. This makes it possible to compare time- and frequency domain models.

4.4.2 TurbSim

The wind fields for the simulations are made using 64-bit TurbSim for 5500 s. This corresponds to one hour with startup time. Turbulent winds are modeled as a "turbulence box" according to the Kaimal spectrum, with corresponding turbulence intensities of 5%, 15%, and 25%. A normal turbulence model for class C of the IEC 61400-1 standard is modeled. This follows the TI according to Figure 3.5 illustrating the TI with increasing wind velocities.

In this thesis, the grid has dimensions of 250 m by 250 m and consists of 48x48 grid points. The grid size is this size as the diameter of the rotor is 240 m, and a larger grid size is an unnecessary computational cost. The time step for wind generation in TurbSim is 0.05 s. The mean wind above the sea varies with the height of the tower, as described in Section 2.7.2. The variation of the mean wind velocity is calculated using the power law formulation in Equation 2.37. The reference wind velocity is located at 150 m, and a power law exponent of 0.14 is used. This is illustrated in Figure 4.12.
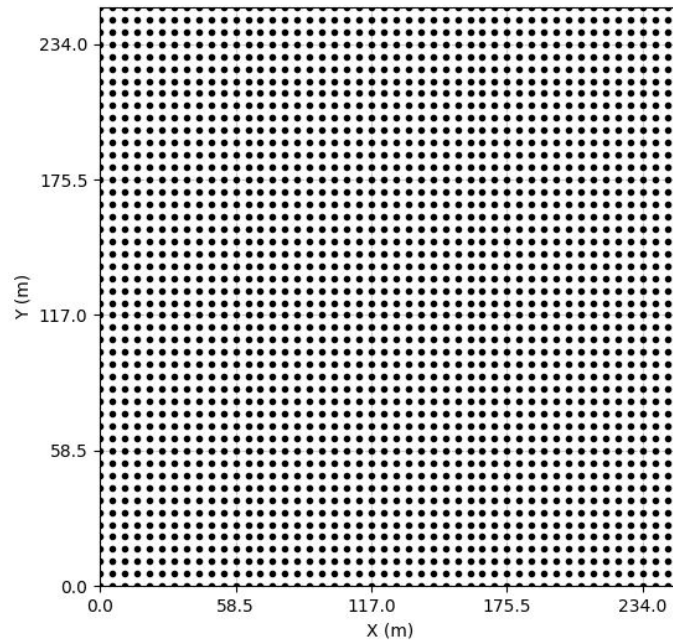
Figure 4.12: Illustration of grid size in TurbSim

Chapter 5

Validations of Models

This chapter presents tests conducted to validate the performance of the modified wind turbine installed in SIMA. The tests include decay tests, PQ analysis, and constant wind tests, aimed at assessing the capabilities and limitations of the Modified WT model. The Modified WT model is compared to the Rigid WT, which has a fully rigid floater, while the Modified WT incorporates RIFLEX elements for the pontoons and SIMO-body mooring lines. The Modified WT is also validated with regard to the frequency-domain and analytical results.

A third model, where the columns are modeled as RIFLEX elements, is investigated but yielded unsatisfactory results in roll and pitch. A similar flexible model by Li et al. at NTNU, published in late May 2023, exhibited similar eigenfrequencies to the Flexible WT model in this thesis. Nonetheless, the Modified WT is used for further investigations. Detailed findings and discussions on the Flexible WT model can be found in Appendix A and Section A.2. Also, an attempt to do a local analysis can be found in Section A.1.

5.1 Decay Tests Results

Decay test analyses are performed to find the natural periods and damping of a structure. Decay tests have been conducted to compare the Modified WT with the Rigid WT and the results of NREL. If the Modified WT model moves similarly to the Rigid WT and NREL, it is a good indication the model provides sufficient results.

	Rigid WT		Modified WT		NREL	
	Period [s]	Frequency [Hz]	Period [s]	Frequency [Hz]	Period [s]	Frequency [Hz]
Surge	135.87	0.0074	135.7	0.0074	142.9	0.007
Sway	136.47	0.0073	138.9	0.0072	142.9	0.007
Heave	20.18	0.0496	20.89	0.0479	20.4	0.049
Roll	27.86	0.0356	26.29	0.0380	27.8	0.036
Pitch	28.55	0.0350	28.81	0.0347	27.8	0.036
Yaw	91.1	0.0110	93.1	0.0107	90.9	0.011

Table 5.1: Eigenvalues from decay tests compared to the results of NREL [4]

The eigenvalues in Table 5.1 correspond similarly to those obtained of the Rigid WT and NREL. however, the eigenvalues are slightly higher, suggesting increased flexibility in the floater. The motion analysis in Figure 5.1 illustrates the response of the Modified WT to applied forces and moments compared to the Rigid WT. The lines are dashed until the release at 200 s, and the motions after are the free-body motions. The Modified WT displays longer surge and sway motions, indicating slower movement. This is possibly due to the quasi-static nature of the SIMO-mooring lines or the increased flexibility of the pontoons. Similar behavior is observed in yaw motion. The
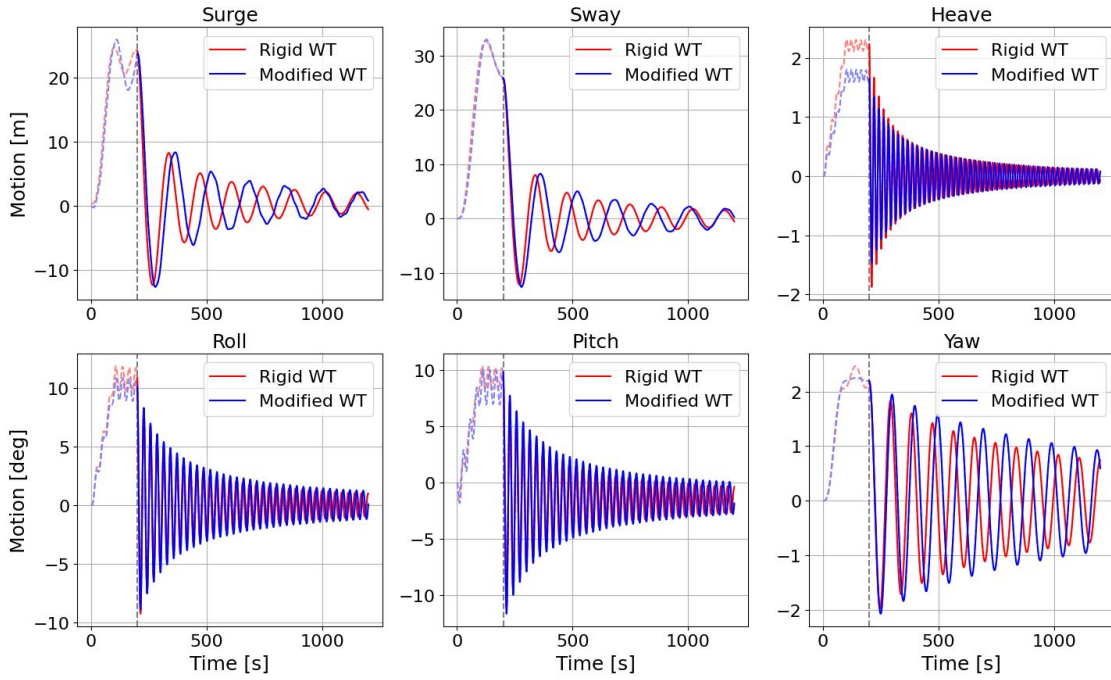
Figure 5.1: Motions of the Rigid WT and the Modified WT

heave, roll, and pitch motions closely resemble the Rigid WT and NREL results. The differences in motion can be attributed to the more realistic representation provided by the flexible model compared to the idealized rigid body model. Nevertheless, the impact of modeling the floater more flexible is more apparent in other tests.

Comparing eigenvalues and response spectra of bending moments, it is observable that the Modified WT generally experiences higher motion levels than the Rigid WT, consistent with the hypothesis that increased flexibility leads to greater motion. The response spectrum in Figure 5.2 shows small peaks in the modified model, indicating slight interference with other wind turbine motions. Specifically, roll and pitch eigenfrequencies give rise to peaks in surge and sway motions, respectively.
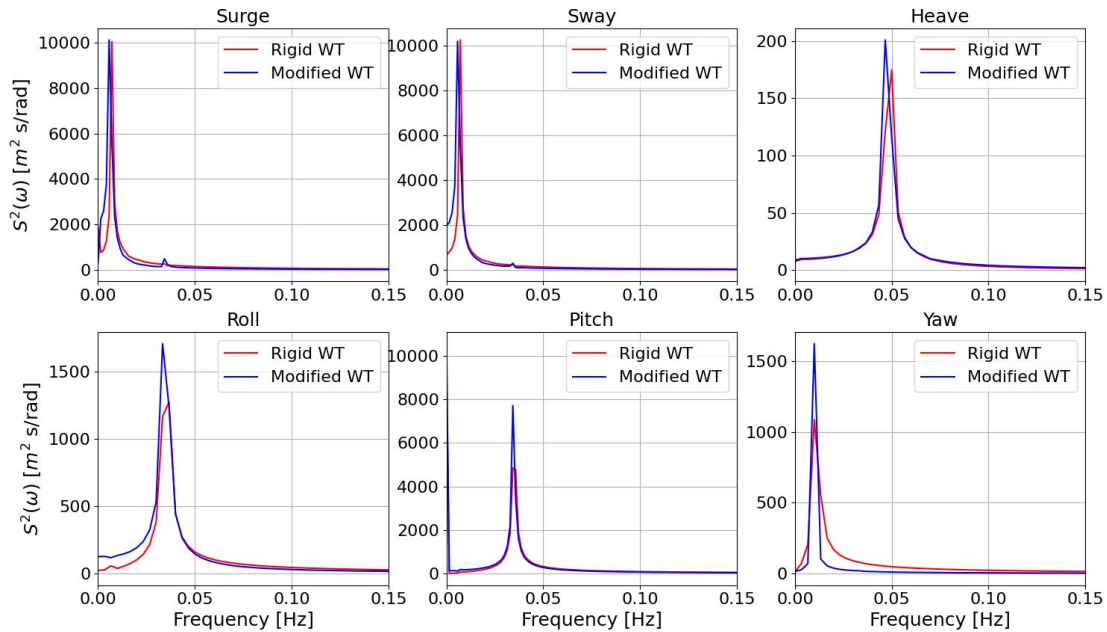
Figure 5.2: Response spectrum of the Rigid WT and Modified WT models

5.2 Response Amplitude Operator

In this thesis, the focus is on the heave and pitch motion, where the Roll Amplitude Operators (RAO) perform as an indicator of consistent results between the SIMA time domain models and the HydroD frequency domain model. To confirm that the model in HydroD is valid, the results have been compared with the open-source results from the NREL with respect to the added mass coefficients. The panel model created in GeniE is implemented in HydroD, with the results further implemented in SIMA.

The results and comparison for frequency-dependent added mass are illustrated in Figure 5.3. It can be observed A_{11} and A_{22} are equal to each other. This is to be expected, as there are four columns working in both directions. A_{44} and A_{55} are also equal, which is due to symmetry as both contain an equal amount of oscillating columns.

(a) Added mass in translational motions   (b) Added mass in rotational motions
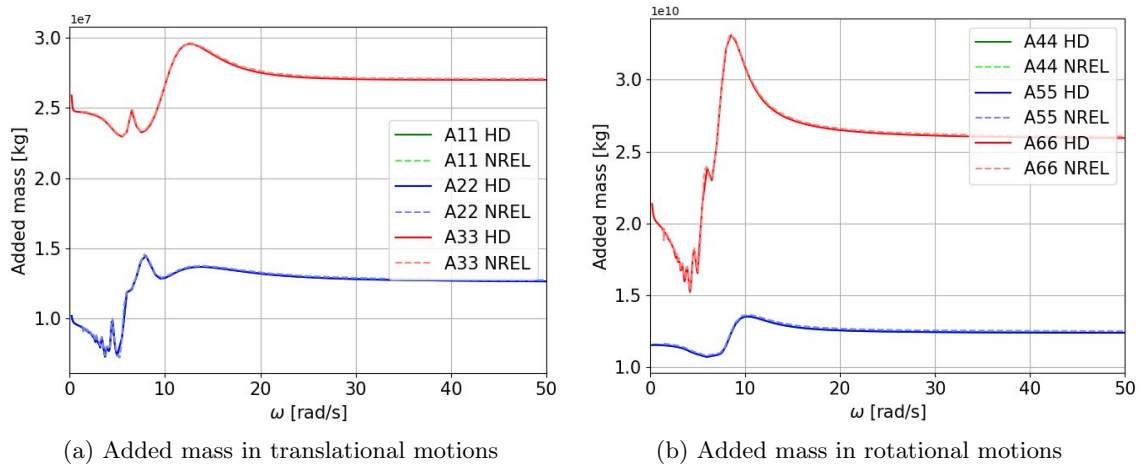
Figure 5.3: Added mass comparisons between HydroD and NREL

Upon observing the comparison, it is apparent the model in HydroD an acceptable representation of the floater, comparing it to the results from NREL. For all six degrees of freedom (6DOF), the outputs from the HydroD simulations align with NREL. This exhibits the satisfactory performance of the HydroD simulations and verifies the reliability of implementing the coefficients in SIMA. Consequently, this implies that the model employed in GeniE is accurate in terms of geometry and utilizes a sufficiently fine mesh size.

Since the results from HydroD align with those from NREL, it is reasonable to proceed with the implementation in SIMA. The Response Amplitude Operators (RAOs) can be derived from HydroD and compared with the RAOs obtained through white noise simulations in SIMA. The comparison of the RAOs is illustrated in Figure 5.4.

The heave RAO for the Rigid WT models exhibits a peak at 20.2 s, while the Modified WT model shows a peak at 20.3 s. This aligns with the findings of the decay test. The time step employed in the white noise is relatively coarse, with a value of 0.475 s. Achieving a more accurate representation would require conducting additional simulations. However, due to their large file size, this would entail significant computational costs. Regardless, the results were found to be close enough to the results of the decay tests. The peak of the HydroD simulations is at 20.75 s, slightly differing from the eigenperiod in the heave of 20.20 s obtained directly from the WADAM.LIS-file, which consists of direct results from the analysis. Furthermore, the pitch RAO displays a peak at 27.9 s for both models, consistent with the decay test results. The results of the HydroD simulations display a peak at 27 s. These observations indicate a strong similarity between the time- and frequency domains of the simulations, further validating the findings of the decay test.

Nevertheless, differences in the magnitude of the RAO peaks are apparent, specifically between the Rigid WT and Modified WT models. In RAO for heave, the Rigid WT closely aligns with the magnitude of the HydroD result, while the Modified WT exhibits a larger magnitude at the

eigenperiod. Contrarily, in the pitch RAO, the opposite trend arises. The Modified WT is more comparable to the HydroD results, whereas the Rigid WT yields larger magnitudes. These distinctions can be attributed to the relative flexibility of the SIMA model. The influence of damping on the RAO magnitudes is further discussed in Section 5.3.
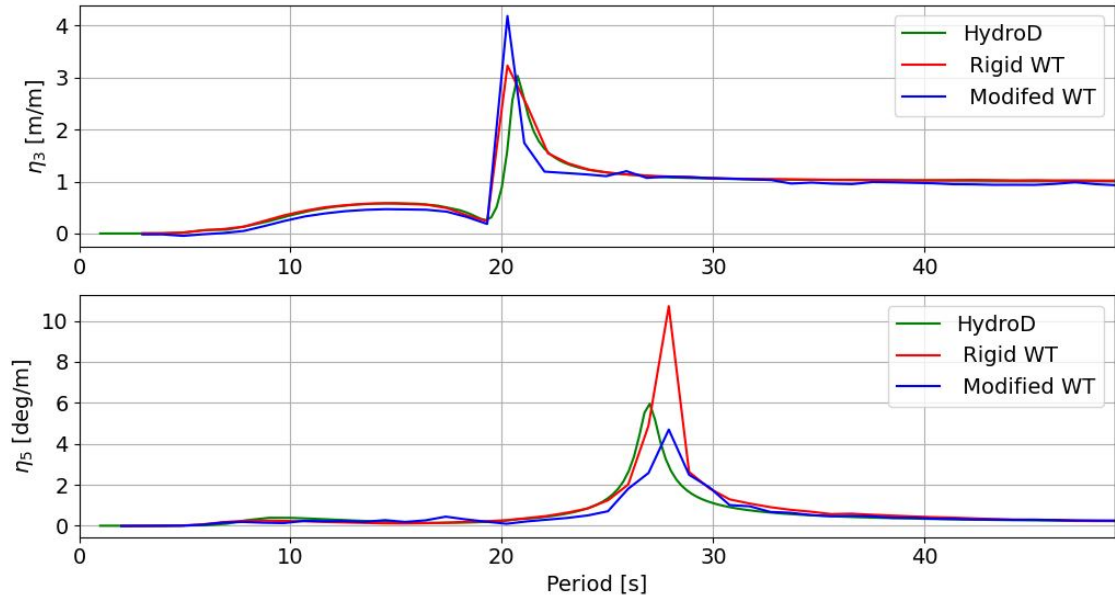
Figure 5.4: Response amplitude operator from HydroD and SIMA

5.3 Damping of The System

Observing the damping of a system is important to provide valuable insights into various aspects, such as stability, performance, and the impact of external loads on the structure. This section focuses on investigating the differences between the Modified WT and the Rigid WT, specifically referring to the findings presented in Section 5.2. By analyzing the damping differences between these two models, a deeper understanding of their distinct behaviors and responses to dynamic loads can be acquired.

5.3.1 PQ Damping Analysis

The PQ analysis is extracted using the results from the decay test in Section 5.1, and it provides an understanding of the damping of the system. The present focus is on heave and pitch damping, as these are essential in analyzing wind turbines. The total work of the damping force is equal to the total loss of the kinetic energy of the system. With P and Q, the linear and quadratic damping can be estimated. In Figure 5.5 and Figure 5.6 is the P-value the point of intercept between the fitted line of point and the y-axis. The Q-value is the slope of the line.

The damping coefficients of the Rigid WT and Modified WT are presented in Table 5.2. The table of hydrodynamic damping is presented in Table 5.3 [4]. Upon observing the quadratic damping coefficient for both cases and the hydrodynamic coefficients, it is evident that there is a presence of structural damping. This implies there is damping originating from other components of the structure, such as the mooring system and tower.

As apparent in the in Figure 5.4 comparing RAO of the Modified WT in the time domain with the frequency domain RAO, there is a difference in the magnitude. The same difference is apparent for the Rigid WT, comparing it with the Modified WT. In Table 5.2 and the illustration of damping in Figure 5.5 and Figure 5.6, there is a difference between the two models. Comparing the damping

	Rigid WT		Modified WT	
	Viscous	**Radiation**	**Viscous**	**Radiation**
Heave	1.714e+04 [kg/s^2]	9.281e+06[kg/m]	4.276+04 [kg/s^2]	8.226e+06 [kg/m]
Pitch	2.314e+08 [kgm^2/s^2]	8.518e+08 [kgm]	1.438+08 [kgm^2/s^2]	8.949e+08 [kgm]

Table 5.2: Damping coefficients extracted from decay tests

	Hydrodynamic damping	
	Viscous	**Radiation**
Heave	- [kg/s^2]	2.296e+06 [kg/m]
Pitch	- [kgm^2/s^2]	4.249e+08 [kgm]

Table 5.3: Hydrodynamic damping of the floater [4]

coefficient between the two models, the linear radiation coefficient (b_1) is increased in heave motion but decreased in pitch motion. For the quadratic viscous damping coefficients (b_2), the value decreased in heave and increased in pitch. It is evident for the difference in the RAOs. For the heave motion, the viscous damping coefficient is increased for the Modified WT compared to the Rigid WT, and the radiation damping coefficient is decreased. However, the radiation is of higher order, and dominant, and the damping is generally found to be decreased, evident in Figure 5.5. The Rigid WT motion is evidently more damped than the Modified WT. The higher radiation damping implies that the Rigid WT is more efficient in dissipating energy through wave generation and reduces its motion more effectively compared to the Modified WT. This reflects the higher magnitude in the RAO for the time-domain Modified WT model.

However, observing the damping coefficients in pitch, there is a decrease from Modified to Rigid WT in the viscous damping and an increase in the radiation damping. Here, the viscous and radiation damping are in the same order and contribute equally to the total damping of the structure. For both models, the radiation damping is the largest, meaning the energy loss due to the generation of waves is larger than the viscous effect of the water. As for the heave motion, the larger radiation damping is apparent in the RAO as the magnitude is lower for the time-domain Modified WT model. The higher viscous damping implies that the Rigid WT experiences more significant energy losses due to the viscosity of the water, leading to a more pronounced deceleration compared to the Modified WT.
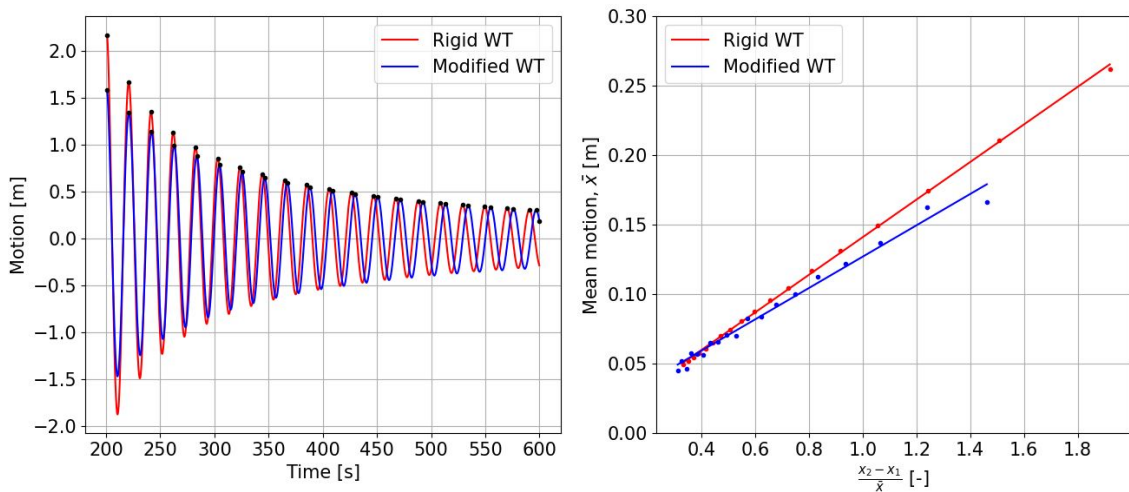
Figure 5.5: Motions and damping results from PQ-analysis in heave
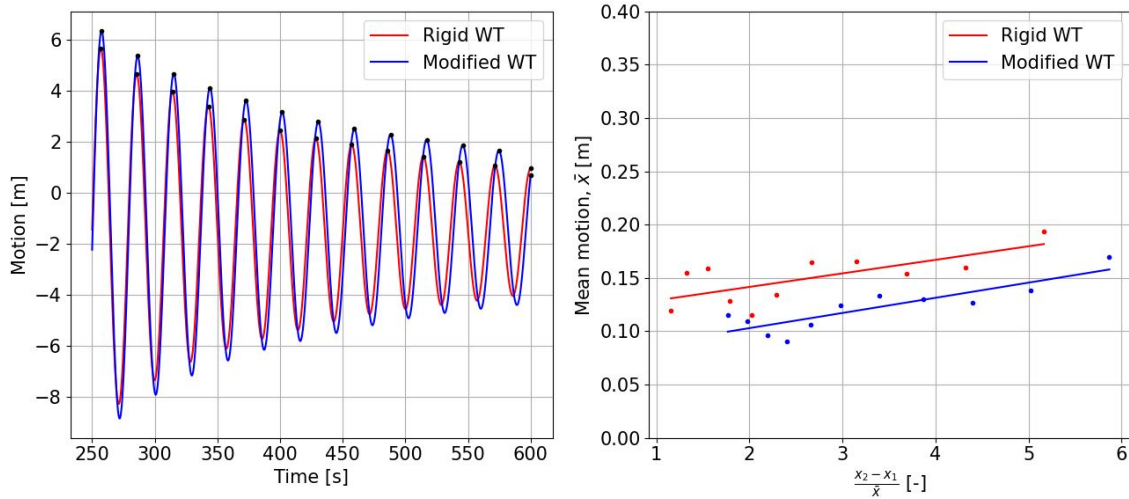
Figure 5.6: Motions and damping results from PQ-analysis in pitch

5.3.2 Dynamic Amplification Factor

The dynamic amplification factor (DAF) is a method to determine the response of the structure due to an external input force. In the case of heave motion, the DAF is determined based on the results obtained from SIMA. By evaluating the absolute value of the transfer function, the dynamic response can be quantified, and dividing it by the static component provides the DAF. To simplify the analysis, the DAF is calculated based on a simplified single-degree-of-freedom system, taking into account mechanical properties such as stiffness, mass, and damping. Figure 5.7 presents both the numerical and analytical DAF results.

Similarly to the observations made for the Response Amplitude Operator (RAO) and PQ-analysis, agreeing tendencies can be identified in the DAF. The magnitude of the peak for the Modified WT is larger than for the HydroD and Rigid WT results. This further confirms the theory of the flexible model performing in a different way than the Rigid WT model. Additionally, comparing the models to the analytical DAF, a distinct characteristic appears. The numerical models display narrower peaks, indicating reduced damping values in close proximity to the natural period.
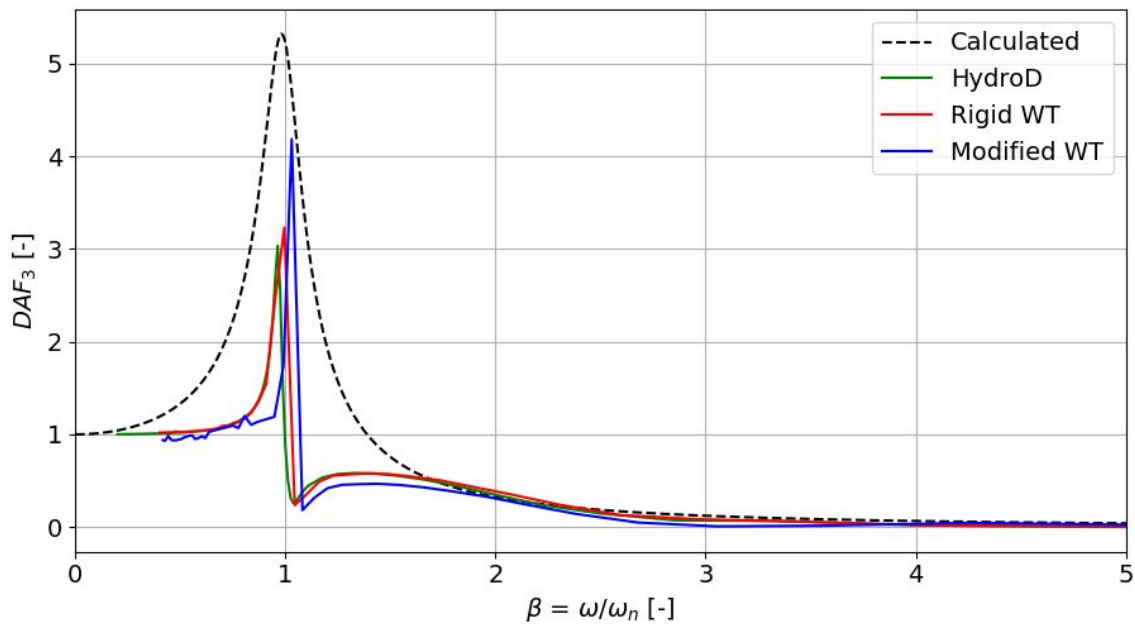
Figure 5.7: Dynamic amplification factor comparison of HydroD, SIMA, and analytical solution

5.4 Constant Wind Tests

A constant wind test is a good test to indicate whether the controller works as it should. Comparing the performance of the Modified WT with both the Rigid WT and the results obtained from NREL in Figure 5.8, it is evident that the modified wind turbine performs as desired. The comparison indicates that the modified wind turbine is capable of producing results similar to those of the Rigid WT and the NREL test results. Especially, for higher wind speeds, the results are equal for all three models. These findings provide a strong indication that the modifications have produced positive results.

The results from both models in SIMA depict the same results with negligible differences. However, in the operating region (Region 2), both models have differences compared to the results from NREL. The largest differences from the NREL results are the blade pitch angle and the thrust forces. The reason for the differences in thrust force may be peak shaving. Peak shaving in terms of thrust force in wind turbines refers to the practice of limiting the maximum thrust force that the wind turbine experiences in the operation region. This is done to reduce the stress on the blades of the wind turbine. This is also exhibited in the generated power. The difference between the models in SIMA and the results from NREL begins at the same wind speed at which the peak shaving begins and ends at the same wind speed. This leads to the maximum generated power at 15MW being reached at a higher wind speed and not at the rated wind speed.

For the blade pitch angle, it is possible the higher blade pitch angle in Region 1 is due to the pitch movement increasing noticeably more than the simulations done by NREL. NREL has conducted the simulations in OpenFAST, which is built on both BEMT and GDW for the aerodynamic model. In comparison, SIMA is built on BEMT. The difference in blade pitch angle is reflected in the RPM for the wind speed close to the rated wind speed. This may also be related to peak shaving as well.
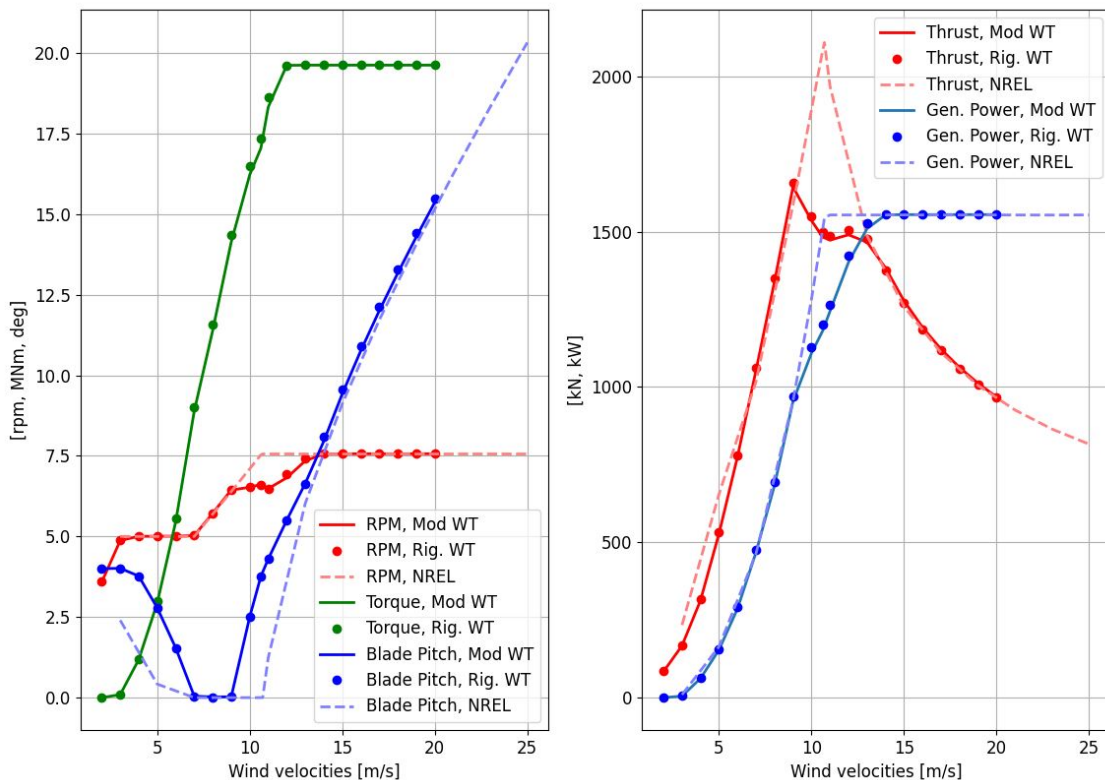
Figure 5.8: RPM, torque, blade pitch, thrust force, generated power results from constant wind tests

5.5 Fatigue Damage Analysis

The tests in the previous sections validate Modified WT and provide satisfactory results comparing it to results from NREL, the Rigid WT, and the frequency domain. Though the RAO and damping have the model has been proven flexible. However, the flexibility is additionally reflected in the fatigue results. A selected range of environmental conditions is presented in Table 5.4.

Condition	Wave height [m]	Wave period [s]
1	2.5	4.5
2	2.5	5.5
3	2.5	6.5
4	2.5	7.5
5	2.5	8.5
6	2.5	9.5

Table 5.4: Conditions to validate flexibility of the SIMA model

The fatigue damage is found in the tower in the transition between the tower and the floater. This transition is also the transition from SIMO-bodies to the RIFLEX-elements in the tower. A difference between the two models will be reflected in this section of the model. This is illustrated in Figure 5.9, where each point is one of the conditions in Table 5.4. Consistently larger fatigue damage can be observed for the Modified compared to the Rigid WT. This confirms a more flexible model. It also depicts how a rigid body is an idealization, and changing the pontoons to beam elements increases fatigue damage in the tower.
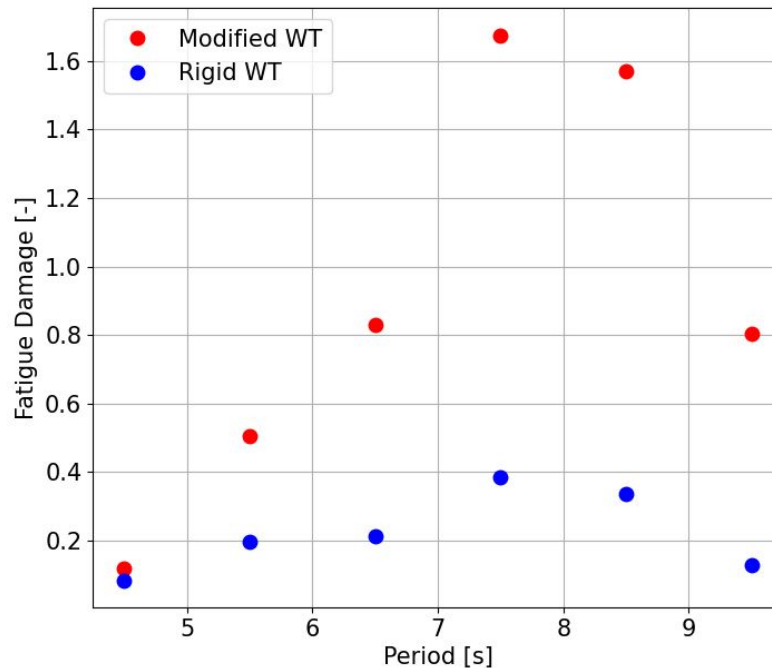
Figure 5.9: Differences in fatigue damages in Rigid WT and Modified WT due to irregular waves

5.6   Eigenvalue Analysis

Eigenvalue analyses were conducted for the Modified WT to observe the mode shapes of the pontoons. The mode shapes are illustrated in Figure 5.10 and Figure 5.11, exaggerated by a thousand to enhance the visual observation of the mode shapes. The first mode shape has an eigenvalue of 2.587 s and the second 0.942 s. The eigenvalue analyses reveal the significant flexibility of the Modified WT. The eigenperiods of the tower are 2.02 s in the fore-aft (FA) bending motion and 2.07 s in the side-side (SS) motion. The first mode shape is close to the tower eigenperiods, and the interaction of these two may lead to increased fatigue damage. Such low eigenvalues for the mode shapes can contribute to noise and potentially also increase fatigue damage.
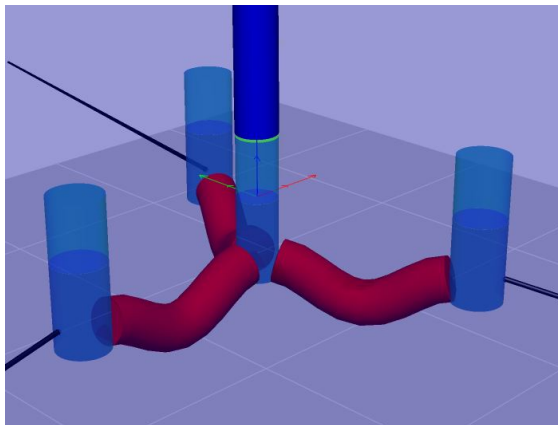
(a) Mode shape 1, SIMA
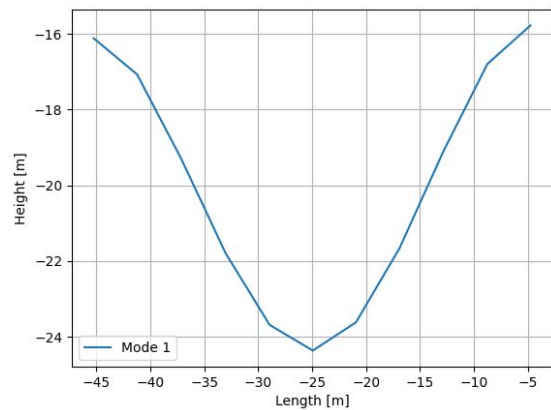
(b) Mode shape 1, plot

Figure 5.10: Visual presentation of mode shape 1 of the pontoons
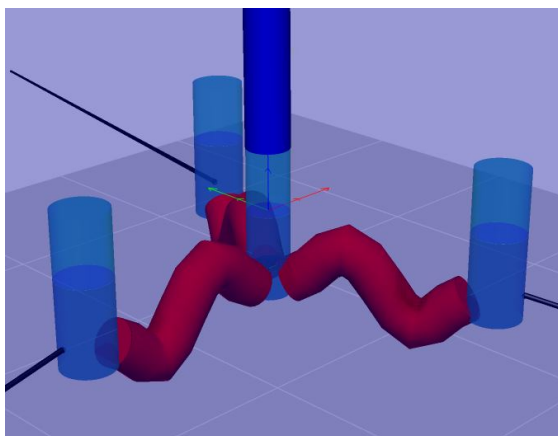
(a) Mode shape 2, SIMA
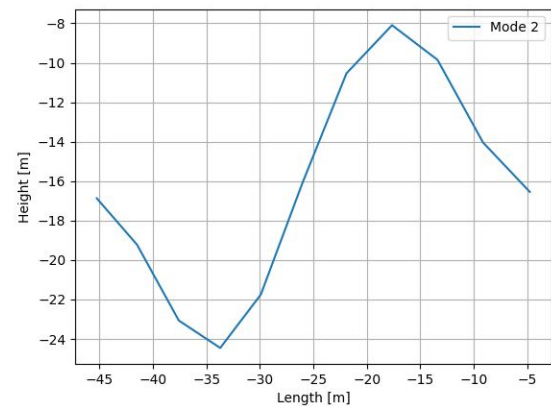
(b) Mode shape 2, plot

Figure 5.11: Visual presentation of mode shape 2 of the pontoons

An investigation of the tower bending natural frequencies found the frequencies to be lower than the rigid body. NREL found the first FA tower bending frequency to be at 0.496 HZ, and the first SS tower bending frequency to be at 0.483 Hz. However, in the case of the Modified WT, the FA tower bending frequency is found to be 0.370, and the SS frequency is 0.375 Hz. This corresponds to the findings of the flexible model by Li et al. [23]. In this paper, the eigenfrequency of the tower is found to be 0.38 Hz. This further validates the Modified WT model.

5.7 Sensitivity Study

There are several choices to be made while modeling the wind turbine in SIMA. This section aims to discuss and justify the different choices made in this thesis. The choice of elements to represent the mooring lines, the time step used in simulations, how many elements were used for the modifications done on the floater, and lastly, the number of wind and wave seeds.

5.7.1 Mooring Line Modeling

Due to computational cost and time-consuming simulations, the mooring lines for the Modified WT are modeled using SIMO elements. The mooring lines are out of interest in this master thesis, and simplifications are preferable. However, this modification introduces potential differences from the RIFLEX-elements. This includes different theories for each element type. RIFLEX-elements are built on slender system theory, and the SIMO-elements are built on rigid body theory. The SIMO catenary system includes all catenary mooring lines connected to one body and is less time-consuming.

To observe the differences in the two types of mooring liners, a rigid SIMO-body for the floater is best for comparisons. This reduces the potential noise of other RIFLEX elements. In Figure 5.12 are the bending moments in the y-direction and the corresponding response spectra illustrated for three environmental conditions. All cases have been simulated using a significant wave height of 2.5 m and different peak periods. Case 1 represents simulations done for a peak period of 5.5 s, Case 2 with 7.5 s and Case 3 with 9.5 s. Here, the difference between the modeling using SIMO-elements is adequately similar to using RIFLEX-elements. They dispute negligible differences. The slight differences are noticeable, but the results validate the SIMO-catenary system instead of the slender system RIFLEX-elements for modeling mooring lines.
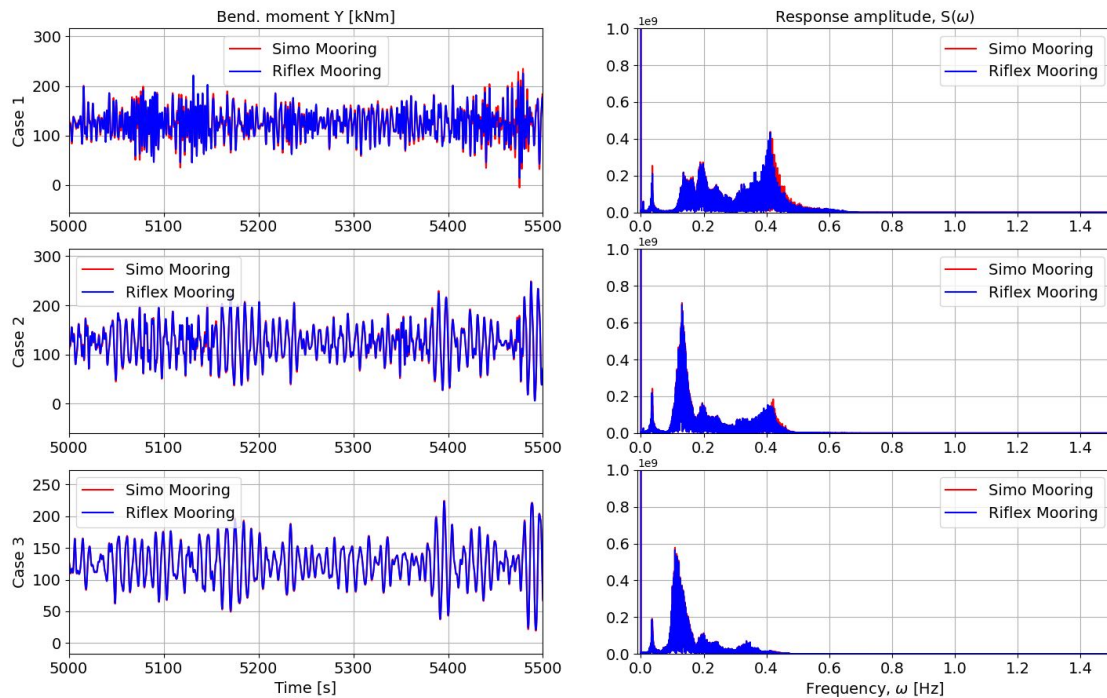
Figure 5.12: Sensitivity study of modeling mooring lines, bending moments, and corresponding response spectra

5.7.2 Time Steps in Simulations

The time step of the simulations is crucial to capture all possible effects on the wind turbine. However, a smaller time step equals a higher computational cost and a longer duration of simulations. This section aims to justify the choice of the time step for further simulations. The simulations are conducted for a time length of 5500 s and different time steps. Figure 5.13 illustrates how the different time step provides information about the bending moments in the y-direction in the tower base cross-section. It is noticeable a finer time step results in better capturing of the response on the structure. The difference is insignificant when comparing a time step of 0.025 s with a time step of 0.05 s. With a time step of 0.05 s, most of the response of the structure is captured, but for half the time it takes to run simulations with a time step of 0.025 s. For this reason, the time step of 0.05 s is found to be a good enough value.
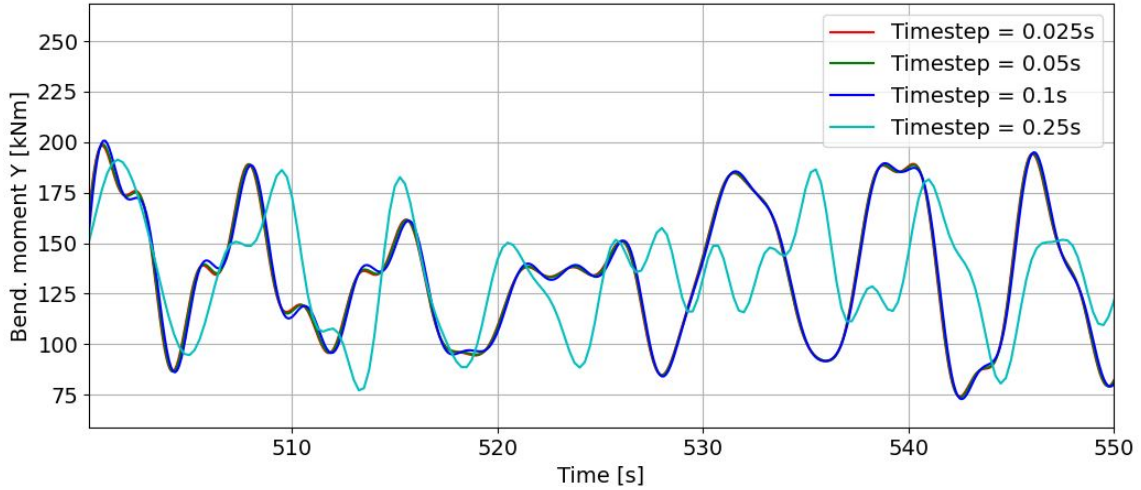
Figure 5.13: Bending moments for different time steps in the tower base

Moreover, observing the differences in fatigue damage in Table 5.6, there are slight differences for the different timestep. It is also apparent the fatigue damage is increasing for smaller timesteps, which makes sense as the simulation captures smaller differences. However, the difference of a timestep of 0.05 s compared to a timestep of 0.025, is acceptable regarding time saved.

Time step [s]	Fatigue damage [-]
0.025	1.898e-03
0.05	1.895e-03
0.1	1.888e-03
0.25	1.778e-03

Table 5.5: Fatigue damage due to different time steps

5.7.3 Elements in The Pontoons

This section investigates the sensitivity of the number of elements in the RIFLEX elements modeled for the pontoons on the Modified WT. To examine the sensitivity of the number of elements, the different cases are illustrated in Figure 5.14. The simulations have been done for a simulation time of 5500 s, and a time step of 0.05 s, as proven to be adequately accurate. No wind is present, and the irregular waves have a significant wave height of 2.5 m and a peak period of 7.5 s. In this thesis, the forces and moments in the structure are extracted close to each column, and the middle part of the pontoon is modeled using two elements. This is done to save computational time but still be able to capture possible effects on the pontoon. However, the parts closer to the columns are modeled with a higher number of elements to capture the loads on the structure better.

(a) Number of elements is 2

(b) Number of elements is 5

(c) Number of elements is 10

(d) Number of elements is 20
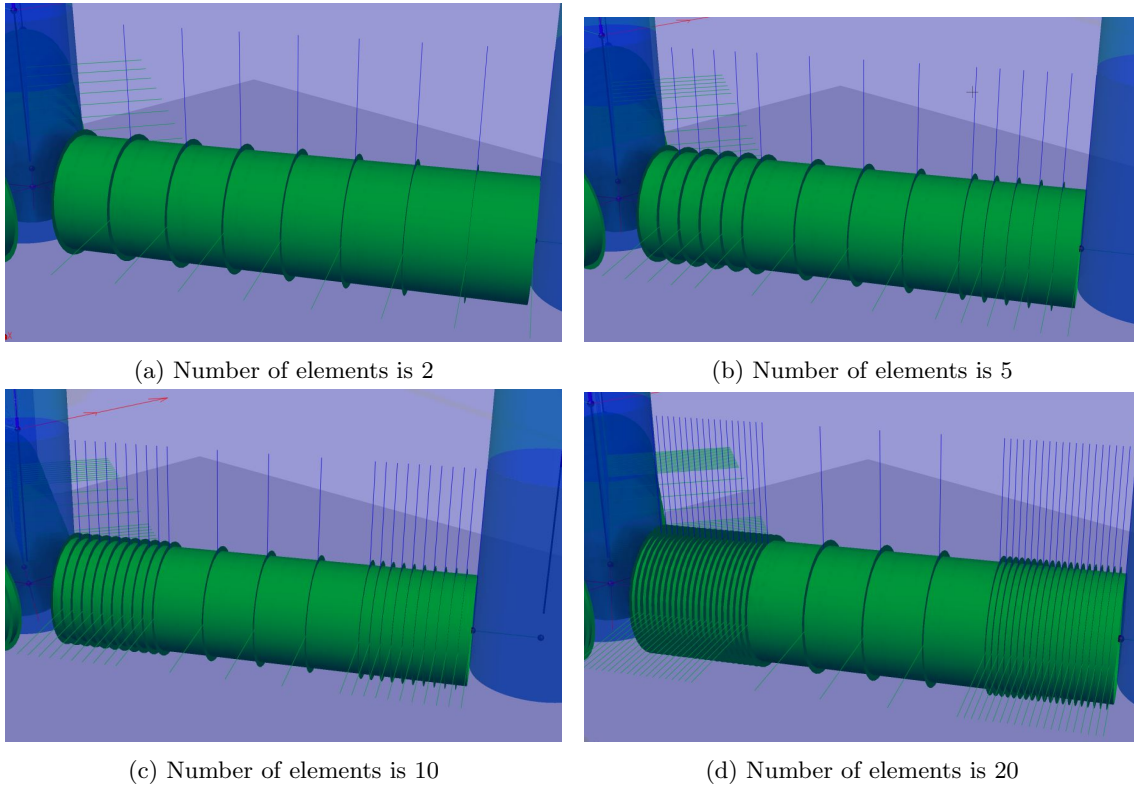
Figure 5.14: Visual presentation of different number of elements to represent the pontoons

Figure 5.15 illustrates the bending moments in the y-direction in the cross-section closest to the tower, namely P1.2. It can be observed that numbers equal to or higher than five give negligible differences. With a number of elements of five, the bending moment is found to be lower than for the higher numbers. Also, investigating the differences in fatigue damage for one hour, in Table 5.6, reveals minor differences. Especially the difference in using twenty and ten elements is close to none. This proves that ten elements are a sufficient choice of elements.
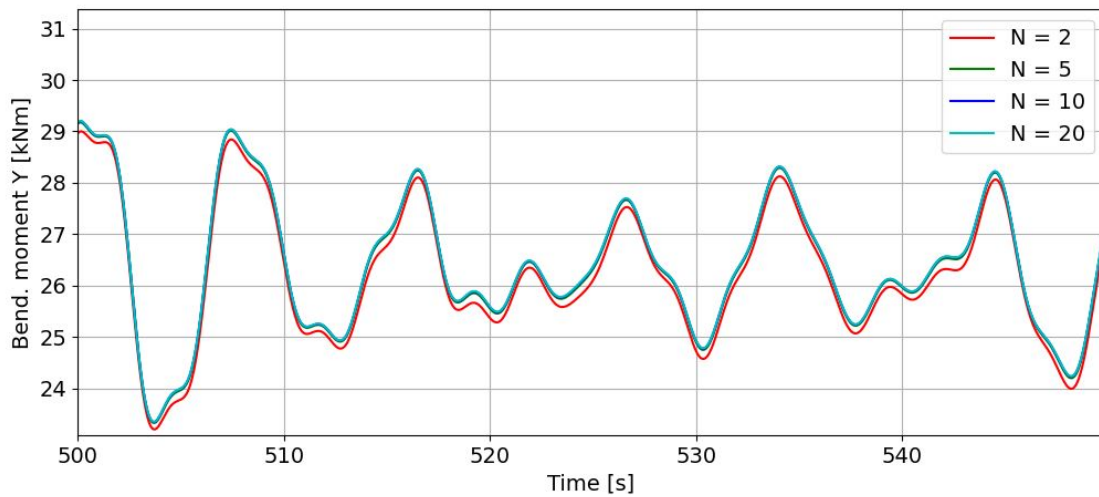
Figure 5.15: Bending moments for different numbers of elements in the pontoon

Number of elements	Fatigue damage [-]
2	5.563e-09
5	5.491e-09
10	5.449e-09
20	5.446e-09

Table 5.6: Fatigue damage due to different number of elements

5.7.4   Number of Seeds

A seed for the generation of random phase angles must be specified. Different seed numbers will generate different time series of wind and waves. To observe the significance of the number of wave and wind seeds, a simulation length of 10,800 s with a timestep of 0.05 s was implemented for the investigation to capture the 3-hours fatigue damage. Further irregular waves with a significant wave height of 2 m, a peak period of 7 s, and a constant wind of 8 m/s are used to find the importance of wave and wind seeds for long-term fatigue damage analysis.

The master thesis written by Ma found that fewer random seeds are also applicable for long-term analysis [54]. Kvittem found a number of seeds of ten to be sufficient [41] for general analysis. The fatigue damage for a different number of seeds for both wind and wave are presented in Figure 5.16. Observing the figure, it is evident the number of seeds provides slight differences. Specifically, the number of seeds seems significant for peak periods 7.5 s and 8.5 s. However, the results are found to be adequate and similar to each other, and for further long-term fatigue damage investigations, the number of seeds for wind and waves is set to be equal to one. Simulations with one random seed can be suitable at the early stage of fatigue analysis, reducing the workload immensely.
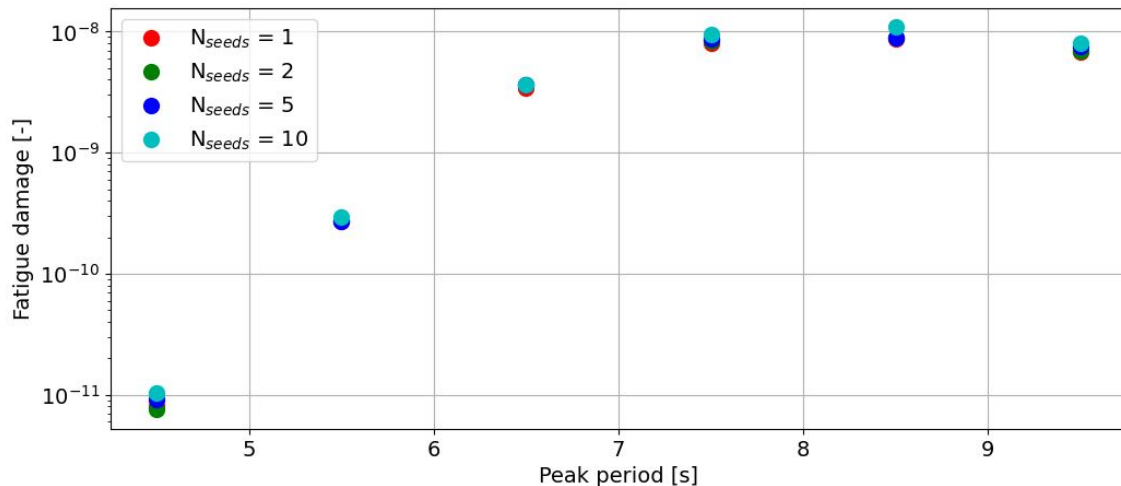
Figure 5.16: Comparison of fatigue damage for different numbers of wind and wave seeds

A

This chapter aims to observe the influence of environmental conditions on fatigue damage for different cross-sections of the wind turbine. Simulations have been done for wind alone and waves alone, both with the wind turbine operating and parked. In the end, combined wind and wave conditions are observed.

The fatigue damage is presented as 20-year damage, as this is the design life of wind turbines. These results are, however, not corrected for the probability of the environmental condition. This is to observe the direct influence of the load, and to have the opportunity to compare the results. A presentation of how fatigue damage evolves when the probability is considered can be found in Appendix B.

A range of environmental values has been selected for these simulations, presented in Table 5.7.

Wave height values, peak periods, and mean wind velocities are considered the most likely and crucial factors that affect fatigue damage according to the Lifes50+ report [21]. To identify any patterns, three particular values of turbulence intensity were selected. However, fatigue damage using TI following the IEC 6400-1 standard is presented in Appendix C.

Parameter	Acronym	Unit	Values
Mean wind velocity	Uw	[m/s]	4-14
Turbulence intensity	TI	[%]	5, 15, 25
Peak period	Tp	[s]	4.5-9.5
Significant wave height	Hs	[m]	0.5, 1.5, 2.5

Table 5.7: Parameters for fatigue damage simulations

5.8 Categorization of Sections to Be Analyzed

In order to get a better insight into the influence of environmental conditions, different cross-sections of the wind turbine are investigated, which allows for a wider range of measurement points. The cross-sections are the transition between the SIMO- and RIFLEX-bodies in the modeled wind turbine in SIMA. These transitional areas are significant for a complete understanding of the behavior of the wind turbine. Multiple cross-sections were selected for both the tower and the floater, as depicted in Figure 5.17. It is important to note that these cross-sections function as interactions between different theories. The SIMO bodies represent rigid bodies, while the RIFLEX-elements are modeled as slender systems using beam elements.

The explanation behind the selection of the areas follows below. This thesis focuses especially on three sections: T0.1 (transition in the tower), P1.1 (transition from pontoon to the first outer column), and P1.2 (transition from pontoon to the center column). Further details concerning the disregarded cross-sections can be found in Appendix D.

T0.1 - This section represents the transition between the tower and the center column, providing insight into the forces exerted by waves and wind. It enables observation of potential effects caused by the blade passing frequency (3P), tower frequency, and tower shadow.

P1.2 - This section represents the transition between pontoon 1 and the center column, and it is the section most likely to be affected by the 3P-frequency during the operation of a floating offshore wind turbine FOWT.

P1.1 - This section represents the transition between pontoon 1 and column 1, which is the first column to interact with waves. In headsea conditions, interactions with the center column can be observed. Additionally, it is interesting to examine the effect of wind-only conditions in this section.

P2.2 and **P3.2** - These sections represent the transitions between the angled pontoons and the center column. They are likely to exhibit effects acting on the tower.

P2.1 and **P3.1** - These sections represent the transitions between the angled pontoons and their corresponding columns. They can be influenced by tower effects, wave wake, and interactions with the center column.
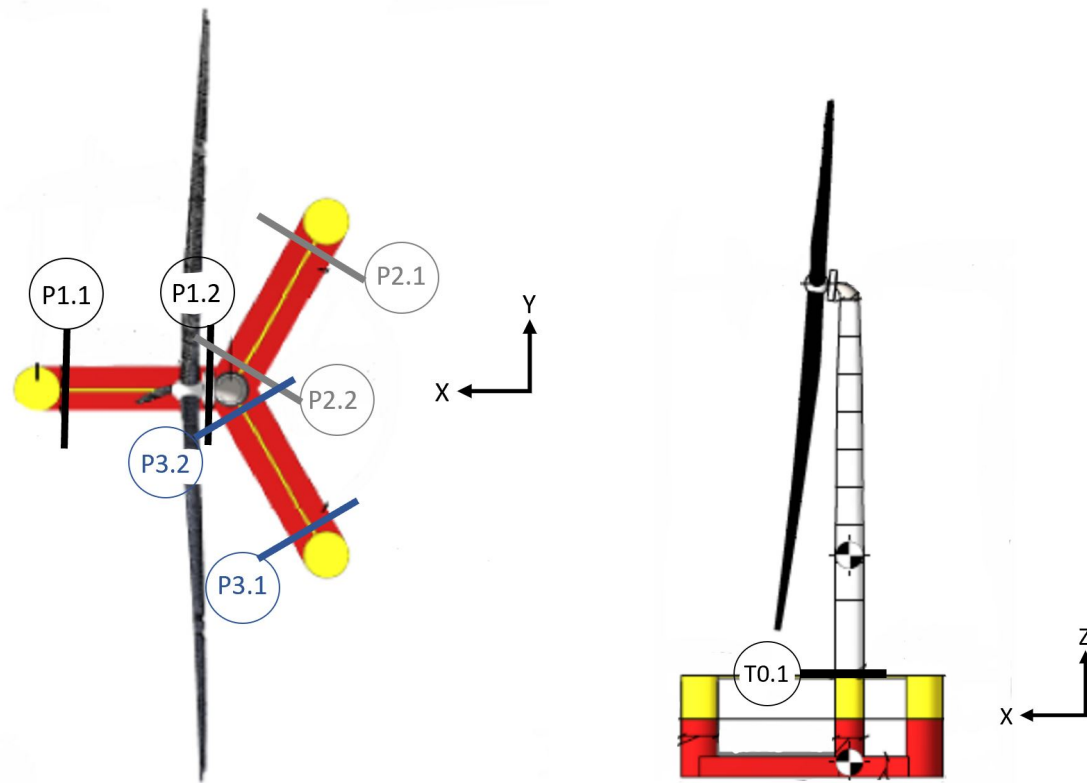
(a) Bird view with the cross-section names   (b) Side view with the cross-section names

Figure 5.17: Categorization of cross-sections to be analyzed in this thesis

5.9   Analysis of Wave Loads Acting Alone

This section investigates how wave loads contribute to fatigue damage (FD) in the floater and tower base. The simulations have been conducted using a one-peak JONSWAP spectrum, and a further discussion between the one-peak and two-peak JONSWAP spectrum is found in Appendix E. The influence of the waves is analyzed for a wide range of wave heights and peak periods. This provides insights into the evolving nature of the FD due to the wave loads acting on the three selected sections of the wind turbine.

5.9.1   Regular and Irregular Wave Loads

Investigating wind turbine responses to regular and irregular waves provides valuable insights into their behavior under different wave conditions. Regular waves help understand fundamental dynamics, while irregular waves simulate real-world scenarios with nonlinear effects. By comparing responses from both analyses, a wider understanding of wind turbine performance can be achieved. Further details and observations can be found Appendix F. However, the main observations are listed below:

- Fatigue damage in the tower base is 100 times larger than the section close to the tower (P1.2), and 1,000 times larger than the cross-section located furthest from the tower (P1.1). And an initial decrease in tower base.

- The peak of the 20-year fatigue damage of the operating WT in the tower base is with a value of 42.7, for Hs = 2.5 m and Tp = 7.5 s. Similarly, the fatigue damage for the parked WT is 39.4.

The response spectrum of the bending stress in the y-direction, as shown in Figure 5.18, captures the impact of waves on the tower base of the structure. Specifically, this spectrum pertains to an operational wind turbine under wave conditions characterized by a significant wave height (Hs) of 0.5 m and a peak period (Tp) of 4.5 s. The figure highlights the phenomenon where regular waves generate considerably higher responses at frequencies corresponding to the peak period. This outcome is expected because regular waves exert loads with the same frequency consistently over a specific time period, resulting in larger responses compared to irregular waves. In contrast, the responses to irregular waves are spread across a broader frequency range.
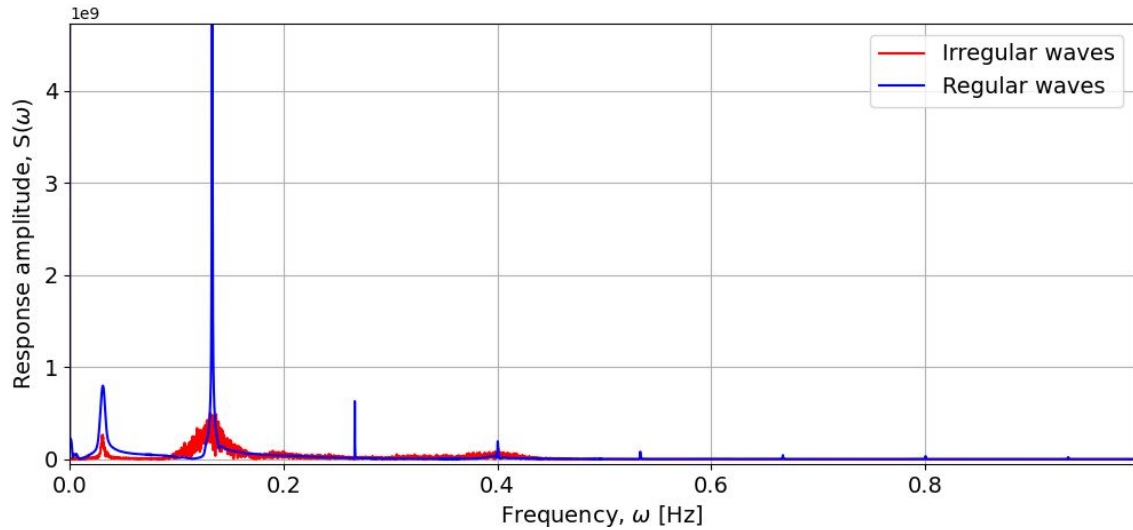

Figure 5.18: Response spectrum of regular vs. irregular waves, large waves

5.9.2 Fatigue Damage in the Tower Base Due to Wave Loads

This section represents the transition between the floater and tower base and is located in the sea water level (SWL). This is a critical section of the WT as the section is in the boundary between air and water. The wave energy is largest at the SWL, and the density difference between air and water can lead to higher fatigue damage.

The fatigue damages (FD) at the tower base, denoted as T0.1, are listed in Table 5.8 and Table 5.9. An explicit correlation between increasing wave height and larger FD values can be observed. The largest FDs are achieved for a wave height of 2.5 m, and the lowest for a wave height of 0.5 m. This observation applies to both the parked and operating WT.

FD [-]		Hs [m]		
		0.5	1.5	2.5
	4.5	0.00138	0.0286	0.87945
	5.5	0.001548	0.07039	3.4886
Tp	6.5	0.00219	0.10321	2.44724
[s]	7.5	0.003148	0.174453	2.6393
	8.5	0.003255	0.16821	1.9148
	9.5	0.00224	0.07057	0.85152

FD [-]		Hs [m]		
		0.5	1.5	2.5
	4.5	1.05e-05	0.00454	0.11748
	5.5	2.366e-05	0.01520	0.50633
Tp	6.5	0.00013	0.04383	0.8282
[s]	7.5	0.00050	0.13131	1.67533
	8.5	0.00055	0.1375	1.569
	9.5	0.000256	0.06191	0.8045

Table 5.8: 20-year FD results in the tower base waves alone for parked wind turbine

Table 5.9: 20-year FD results in the tower base waves alone for operating wind turbine

(a) Parked wind turbine

(b) Operating wind turbine
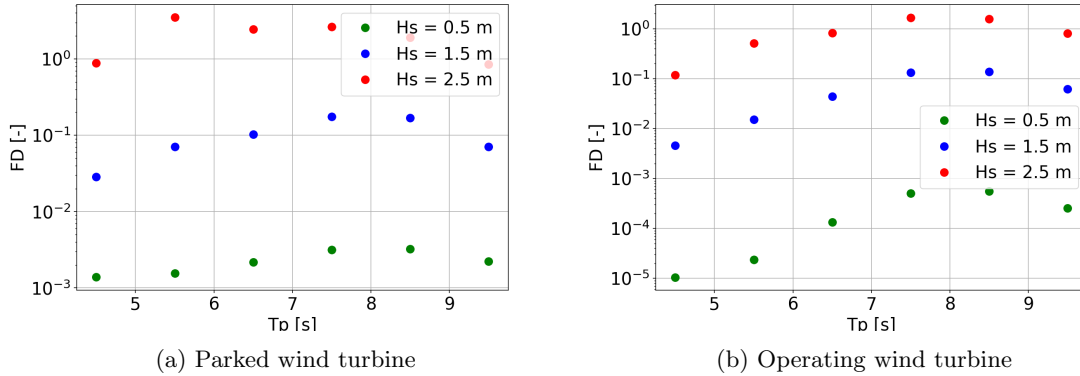
Figure 5.19: 20-year fatigue damage results in the tower base due to waves alone

A more interesting observation can be observed in the illustration of the fatigue damage development in Figure 5.19. In this figure, the x-axis represents the peak periods, and the y-axis represents the fatigue damage on a log scale. The development of FDs with increasing wave peak period. Initially, the FD increases, followed by a blunted peak during wave periods of 7.5 m and 8.5 m. The occurrence of the higher response for these peak periods could potentially be connected to the interaction between the center column and the first column. When the bottom of a wave impacts one column, and the top of the wave hits the center column, it creates opposite-directed forces. This interaction can result in substantial excitation forces due to the contrasting pressures exerted on the columns. According to analytical calculations, considering the distance of 40.5 m between the column and the tower base, this corresponds to a wave period of 10.2 s, which could indeed result in significant excitation forces. However, this explanation does not fully account for the elevated response observed specifically within the 7.5 s to 8.5 s period range. Interestingly, examining the pitch excitation force (F_5) obtained from HydroD, a peak at 9 s becomes apparent, as shown in Figure 5.20. Notably, the pitch excitation force exhibits a peak at 8 s. These findings imply that the increased fatigue damage experienced during the 7.5 s to 8.5 s period range may be due to these excitation forces. It can also be observed that the graph goes toward zero, which is due to the infinite long wave being flat.
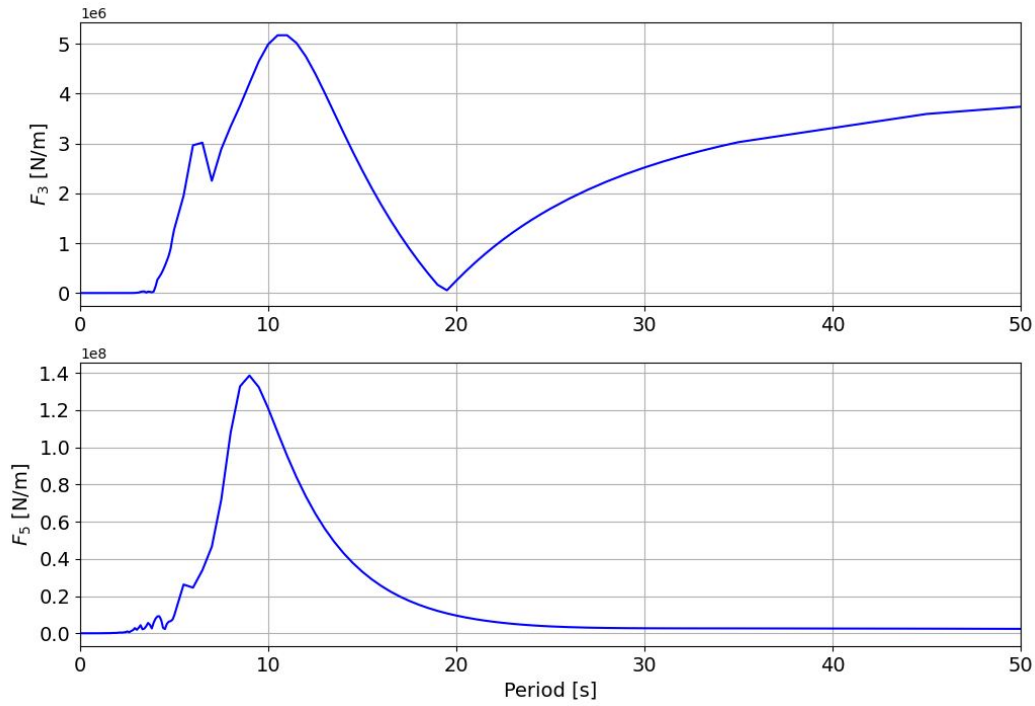
Figure 5.20: Excitation forces acting on the floater

The excitation force in heave (F_3) in Figure 5.20 illustrates a commonly known phenomenon for semi-submersible. It appears to be some cancellation at 19 s, which is close to the natural period in heave. Moreover, a peak can be observed at 10.5 s. This can be connected to the discussion of the interaction between the column discussed previously. For a wave period of 10.2 s, there is a wave top at the first column and a wave bottom at the center column. Also, there can be observed a smaller peak at 6 s. This can also be related to the wavelengths.

Observing the tables of the parked WT Table 5.8 and operating WT Table 5.9, there are minor differences between the two wind turbines. In general, the values of the parked wind turbine tend to be greater than those of the operating wind turbine. This is logical as the wind turbines are not actively functioning in the absence of wind. Nevertheless, subtle contrasts occur, potentially arising due to blade pitching for stability purposes, which alters the center of gravity (COG). Another contributing aspect could be the feathering of the blades when they are parked. The operating wind turbine's blades are angled to optimize thrust for maximum power generation.
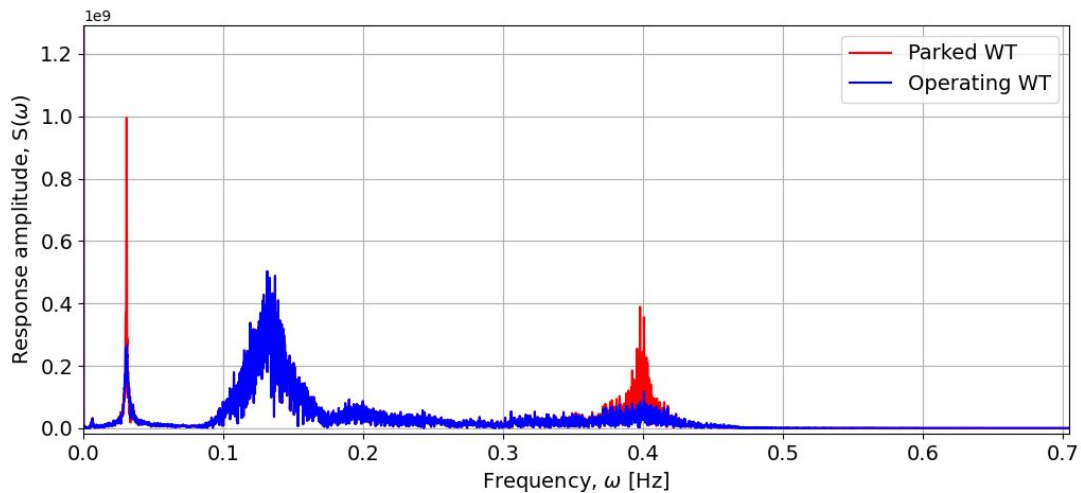
Figure 5.21: Response spectra of bending moments on parked and operating WT

The power spectra for the parked and operating wind turbines with respect to the bending moments for Hs = 2.5m and Tp = 7.5s are illustrated in Figure 5.21. This illustrates how there is a larger response for the parked wind turbine than for the operating wind turbine. In Figure 5.22, the pitch motions fluctuate more in the case of parked WT. There is a peak at 0.033 Hz in the response spectrum. This is the eigenvalue in pitch, which is confirmed to be larger. There is also a larger response around the eigenvalue of the tower. In Figure 5.22 are the bending moments in the local y-direction for the two wind turbine cases illustrated as well. The bending moments in the tower represent the reason why the response at tower frequency is larger. This demonstrates how the wind turbine controller responds when the pitch angle of the turbine experiences significant variations.

Figure 5.22 illustrates greatly how the pitch controller acts when the wind turbine is pitching beyond the wanted range. For the operating WT where the controller is active, the fluctuations in the pitch angles are rapidly reduced compared to the parked, non-operating wind turbine. The parked WT takes nearly 3000 s to stabilize, whereas the operating WT achieves stability within 300 s. The pitch angle fluctuations experienced by the parked WT can lead to negative damping, thereby increasing fatigue damage.
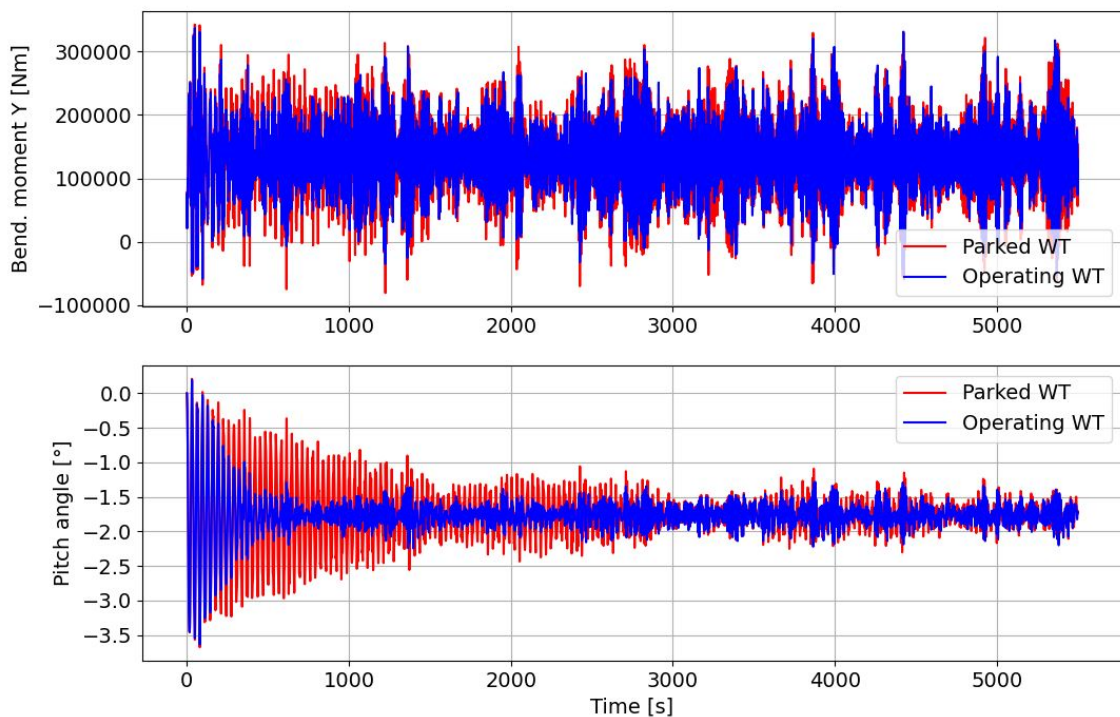
Figure 5.22: Bending moments in the y-direction and pitch motions of the parked and operating wind turbines for waves-only condition

5.9.3   Fatigue Damage in the Pontoon Due to Wave Loads

In this section, the focus is on the cross-sections within the pontoons of the floater. These cross-sections are positioned 16.5 m below the SWL, where the wave energy is reduced. Investigating these sections provides valuable insights into the variations between the SWL and the subsurface. Additionally, comparing the cross-section located near the tower (denoted P1.2) with the cross-section situated farther from the tower (denoted P1.1) offers crucial insights into the factors influencing the floater and underscores the important considerations during the design phase of the wind turbine.

FD [-]		Hs [m]		
		0.5	1.5	2.5
	4.5	4.23e-10	6.42e-08	3.82e-06
	5.5	4.12e-09	1.48e-06	5.63e-05
Tp	6.5	4.48e-08	1.17e-05	0.00021
[s]	7.5	1.02e-07	2.32e-05	0.00033
	8.5	1.07e-07	2.36e-05	0.00031
	9.5	7.61e-08	1.57e-05	0.00019

Table 5.10: 20-year FD results in pontoon (P1.2), waves alone parked wind turbine

FD [-]		Hs [m]		
		0.5	1.5	2.5
	4.5	4.03e-11	1.83e-08	4.90e-07
	5.5	2.24e-09	7.71e-07	1.451e-05
Tp	6.5	3.66e-08	9.52e-06	0.00013
[s]	7.5	9.25e-08	2.27e-05	0.00030
	8.5	9.30e-08	2.24e-05	0.00029
	9.5	6.39e-08	1.52e-05	0.00019

Table 5.11: 20-year FD results in pontoon (P1.2), waves alone operating wind turbine
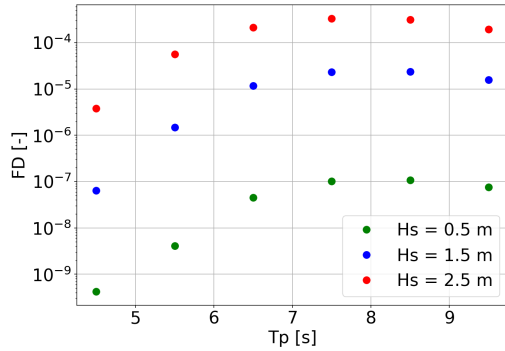
(a) Parked wind turbine
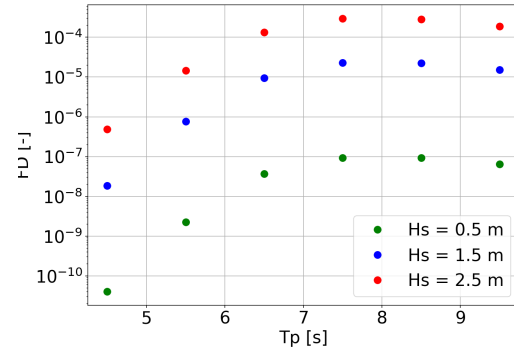
(b) Operating wind turbine

Figure 5.23: 20-year fatigue damage results in the pontoon (P1.2) due to waves alone

The results of the fatigue damage of the cross-section close to the tower (P1.2) are listed in Table 5.10 and Table 5.11, and the tendencies are illustrated in Figure 5.23. Same as for the tower, the cross-section is analyzed for both parked and operating wind turbines. Analyzing Figure 5.23, the FD with increasing wave heights and periods follows a matching trend as for the tower base. It increases with higher wave heights, while also revealing peak values at 8.5 s and 7.5 s.
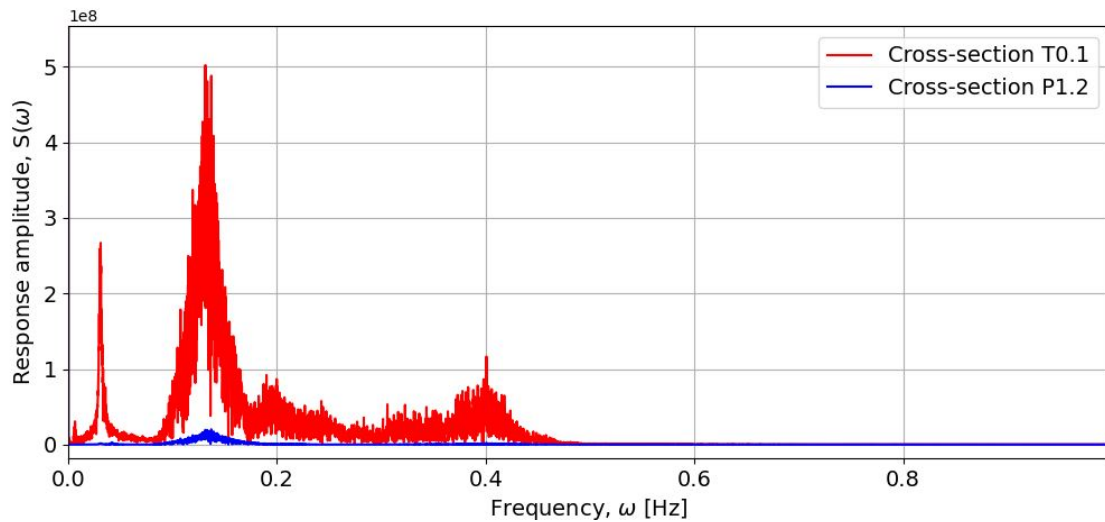
Figure 5.24: Comparison of response spectrum in cross-sections P1.2 and T0.1

Further, comparing the FD results of the pontoon with the damage of the tower base, there is a tremendous reduction in the values. The FD results in the tower base exceed those in the pontoon by a factor of 10,000. Moreover, the initial fatigue damage increases significantly more for increasing peak periods than in the tower base. This demonstrates how the energy of the waves is decreased

at greater depths, a characteristic reflected in the obtained results. The tremendous difference is apparent in the response spectra of the bending moments in the y-direction in Figure 5.24.

The fatigue damage results for the parked and operating WT, in the cross-section located further away from the tower (P1.1), are listed in Table 5.12 and Table 5.13, and illustrated in Figure 5.25. The same tendencies can be observed for the cross-sections in the tower base and close to the tower. The initial fatigue damage increases for increasing peak periods, with a blunt peak at periods from 6.5 s to 8.5 s.

FD [-]		Hs [m]		
		0.5	1.5	2.5
	4.5	6.74e-10	3.77e-08	1.08e-06
	5.5	7.79e-09	1.61e-06	3.44e-05
Tp	6.5	5.58e-08	1.21e-05	0.00018
[s]	7.5	8.40e-08	1.76e-05	0.00024
	8.5	6.69e-08	1.36e-05	0.00018
	9.5	3.92e-08	7.42e-06	9.27e-05

FD [-]		Hs [m]		
		0.5	1.5	2.5
	4.5	5.221e-11	1.63e-08	2.93e-07
	5.5	4.28e-09	1.17e-06	1.75e-05
Tp	6.5	4.37e-08	1.09e-05	0.00015
[s]	7.5	7.11e-08	1.73e-05	0.00023
	8.5	5.31e-08	1.29e-05	0.00017
	9.5	2.92e-08	6.99e-06	8.80e-05

Table 5.12: 20-year FD results in pontoon (P1.1), wave alone for parked wind turbine

Table 5.13: 20-year FD results in pontoon (P1.1), wave alone for operating wind turbine
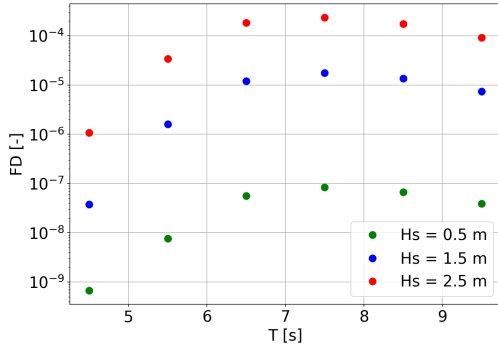
(a) Parked wind turbine
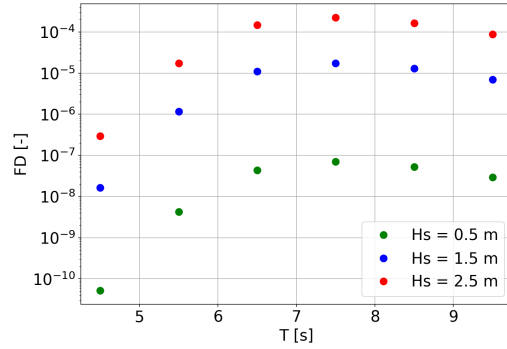
(b) Operating wind turbine

Figure 5.25: 20-year fatigue damage results in the pontoon (P1.1) due to waves alone

Moreover, fatigue damage is slightly lower than the fatigue damage found in P1.2. This indicates that there are neglectable differences between the two cross-sections. However, in Figure 5.26 is the response spectrum of the bending moments in the y-direction for Hs = 2.5 m and Tp = 7.5 s for the cross-sections P1.2 and P1.1 illustrated. The main peak can be observed at the wave frequency 0.13 Hz, corresponding to a period of 7.5 s, but also a major peak at around 0.4 Hz, which is the tower eigenfrequency. The cross-section is, in both cases, affected by the tower. However, it is apparent that P1.2 respond with a higher response than P1.1. The two smaller peaks, in the beginning, represent the eigenfrequencies for heave and pitch.
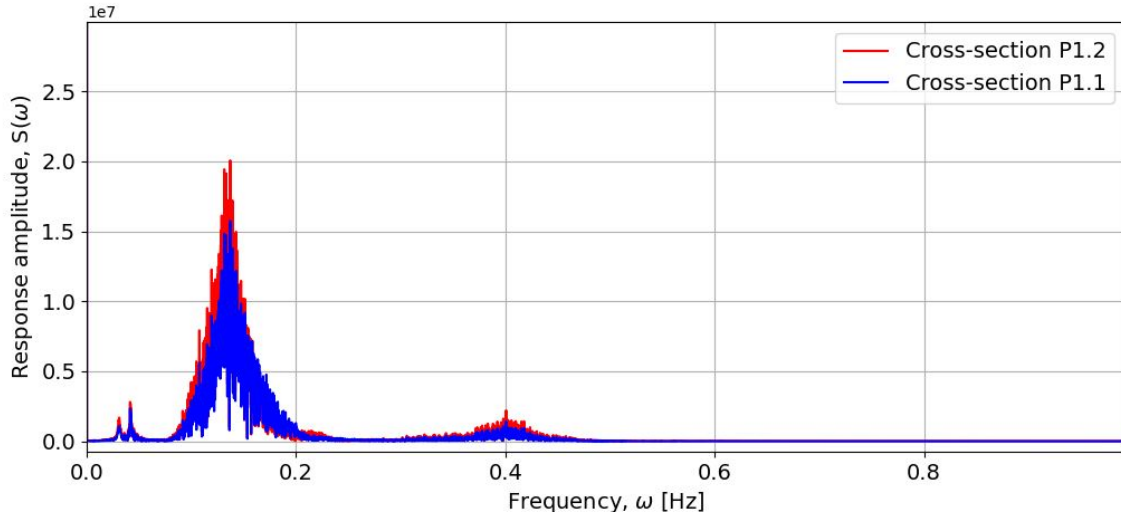
Figure 5.26: Comparison of response spectrum due to waves in cross-sections P1.2 and P1.1

5.10 Analysis of Wind Loads Acting Alone

This section investigates how wind loads contribute to fatigue damage (FD) in the floater and tower base. The influence of the wind loads is analyzed for a wide range of mean wind velocities and turbulence intensity (TI). This provides insights into the evolving nature of the FD due to the wind loads acting on the three selected sections of the wind turbine.

5.10.1 Fatigue Damage in the Tower Base Due to Wind Loads

This section represents the transition between the floater and tower base and is located in the SWL. It is a crucial section of the WT as the section is in the boundary between air and water, and the rotor passes by close to this section. The fore-aft (FA) and side-side (SS) eigenvalues potentially have a large influence on this section as well as the 1P- and 3P-frequency. The Fatigue Damage (FD) results for the parked and operating wind turbines are presented in Table 5.14 and Table 5.15. It can be observed there is a consistent increase in variations as the values increase. Higher turbulence intensities lead to greater fatigue damage.

FD [-]		TI [%]		
		5	15	25
	4	4.33e-6	4.54e-6	4.40e-6
	6	3.97e-7	6.06e-7	1.41e-6
Uw	8	5.03e-8	8.28e-7	8.56e-6
[m/s]	10	1.15e-7	1.82e-5	0.00023
	12	4.65e-7	8.91e-5	0.00097
	14	5.37e-7	0.00011	0.00137

FD [-]		TI [%]		
		5	15	25
	4	1.38e-6	0.00029	0.0037
	6	9.96e-5	0.0133	0.1238
Uw	8	0.00070	0.0749	0.3907
[m/s]	10	0.00570	0.2314	1.1494
	12	0.00134	0.4680	3.2210
	14	0.0068	0.9940	8.4965

Table 5.14: 20-year FD results in tower base, wind alone parked wind turbine

Table 5.15: 20-year FD results in tower base, wind alone operating wind turbine

For the parked wind turbine, FD is observed to be influenced by the TI similar to the blade pitch angles, presented in the constant wind tests Section 5.4. Initially, the FD decreases until reaching a wind velocity in Region 2, whereas the FD increases. As the TI increases, the FD starts to increase at a lower average wind velocity while still following a similar trend. Moreover, as the wind velocities increase, the differences in FDs become more prominent. At lower velocities, the FD values are relatively closer to each other, whereas, at higher velocities, the differences in fatigue damages become significantly larger. This trend is illustrated in Figure 5.27.

(a) Parked wind turbine

(b) Operating wind turbine

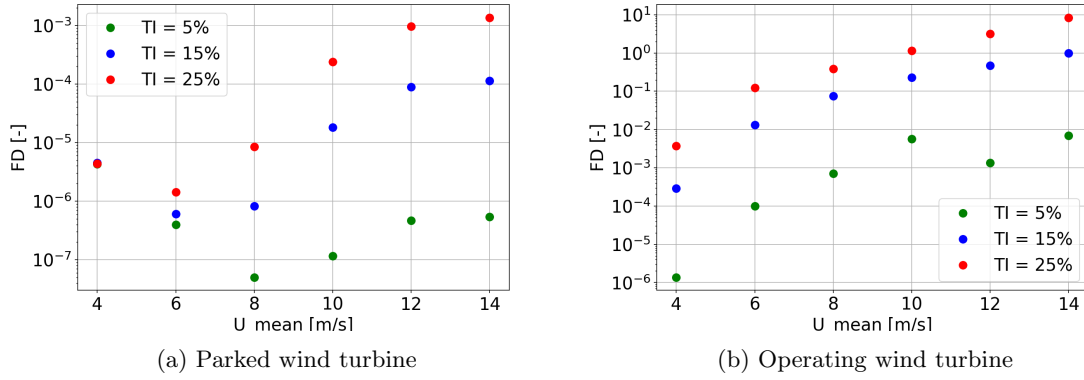Figure 5.27: 20-year fatigue damage in the tower base due to wind loads alone

Higher TI results in more severe FD, and increasing wind speed also contributes to higher FD. Comparing different TI at the same wind speed shows that higher TIs are associated with greater FD, highlighting the influence of TI on the severity of the damage. Similarly, comparing different wind speeds at the same TI reveals that higher wind speeds lead to higher FD, emphasizing the impact of wind speed on the magnitude of damage. In summary, both TI and wind speed significantly determine the level of fatigue damage in stationary wind turbines, with higher values of both factors generally leading to increased damages.

Similarly, in the case of an operating wind turbine, there is also an overall upward trend in FDs as TI increases. Higher TI values result in more significant levels of FD. However, unlike the parked wind turbine, the magnitude of fatigue damages for the operating wind turbine is particularly larger. This difference implies that the forces acting on the wind turbine during operation contribute to more severe fatigue damage compared to parked WT. Furthermore, as the wind speed increases for each TI value, the fatigue damages also tend to rise, signifying that higher wind speeds contribute to increased fatigue damage during turbine operation.

Moreover, it is important to observe the impact of the rotating rotor on the fatigue damage. When the rotor is in motion, it interacts with turbulent wind conditions, resulting in varying stress patterns on the turbine components. This interaction between rotor rotation and turbulent wind can amplify the fatigue damage experienced by the wind turbine. Therefore, when evaluating fatigue damage, it is necessary to consider the combined effects of turbulence intensity, wind speed, and the rotational dynamics of the rotor. Additionally, the tower eigenvalue can interfere with fatigue damage.

Figure 5.29 illustrated the response spectra of the bending moment in the local y-direction for both parked and operating wind turbines. These results were obtained for the condition of a wind speed of 14 m/s and a turbulence intensity of 25%. It shows the immense difference between parked and operating wind turbines. The parked turbine exhibits a peak at a frequency of 0.033 Hz, corresponding to a period of 30 s, which represents the eigenperiod in pitch motions. However, when observing the operating turbine, it becomes evident that the structure is distinctly influenced by turbulent wind acting in co-occurrence with the rotating rotor.

By comparing the response spectrum to the power spectrum from NREL [4], Figure 5.28, it is observed that the response for low frequency aligns with the Kaimal spectrum in Figure 5.29. At the pitch motion frequency, the response appears to be increased instead of following the Kaimal spectrum. Furthermore, there is a general increase in the response within the range of 0.3 Hz to 0.5 Hz. Observing the RPM of the simulation, the minimum and maximum are found to be 4.5215 rpm and 8.825 rpm. This gives 3P-frequencies of 0.226 Hz and 0.441 Hz, respectively. The peak of this increase occurs at approximately 0.41 Hz, equivalent to a period of 2.43 s, which is the tower eigenfrequency. This observation highlights the influence of the coherence of the 3P frequency and the tower eigenfrequency on fatigue damage.
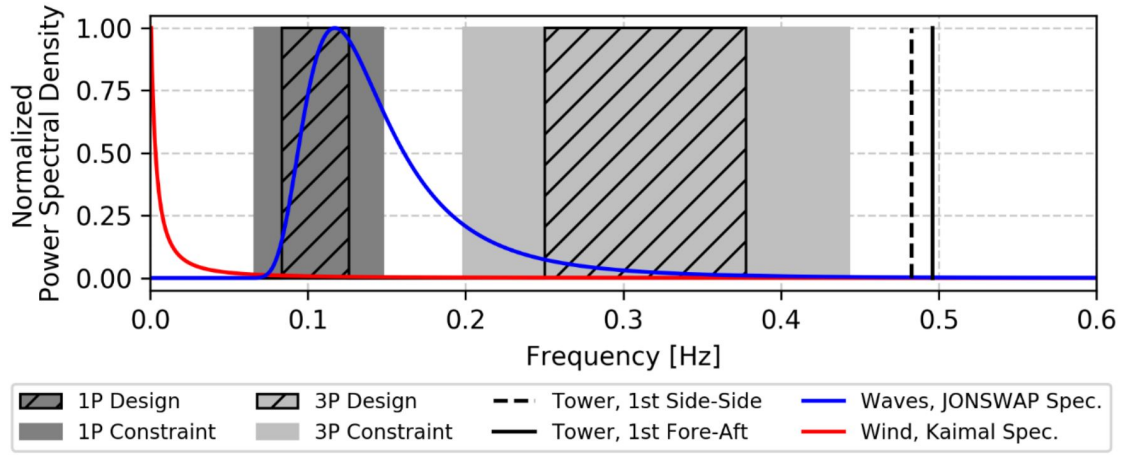
Figure 5.28: Normalized power spectrum [4]
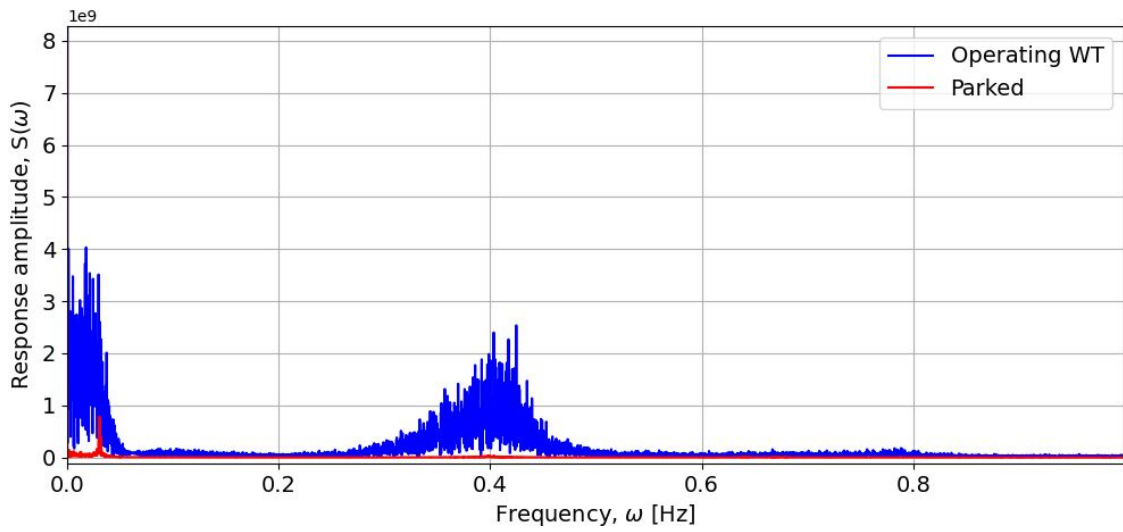
Figure 5.29: Response spectrum of bending moments in the tower base for the parked and operating WT

5.10.2 Fatigue Damage in the Pontoon Due to Wind Loads

In this section, the focus is on the cross-sections within the pontoons of the floater. Investigating these sections provides valuable insights into the variations between the SWL and the subsurface. Additionally, comparing the cross-section located near the tower (denoted P1.2) with the cross-section situated farther from the tower (denoted P1.1) offers crucial insights into the factors influencing the floater.

FD [-]		TI [%]		
		5	15	25
	4	1.412e-14	1.54e-14	5.11e-13
	6	1.81e-15	5.81e-15	6.50e-12
Uw	8	5.41e-16	9.27e-14	6.54e-09
[m/s]	10	2.89e-15	4.55e-12	8.53e-07
	12	1.02e-14	5.31e-11	2.55e-05
	14	3.79e-14	4.15e-10	0.00014

FD [-]		TI [%]		
		5	15	25
	4	3.01e-13	1.35e-10	4.82e-09
	6	1.14e-11	1.34e-07	1.98e-05
Uw	8	7.96e-09	1.76e-05	0.0104
[m/s]	10	8.48e-08	0.0003	0.0140
	12	2.94e-07	0.0049	0.9383
	14	2.75e-06	0.0685	3.4019

Table 5.16: 20-year FD results in the pontoon (P1.2), wind alone for parked wind turbine

Table 5.17: 20-year FD results in the pontoon (P1.2), wind alone for parked wind turbine

(a) Parked wind turbine   (b) Operating wind turbine
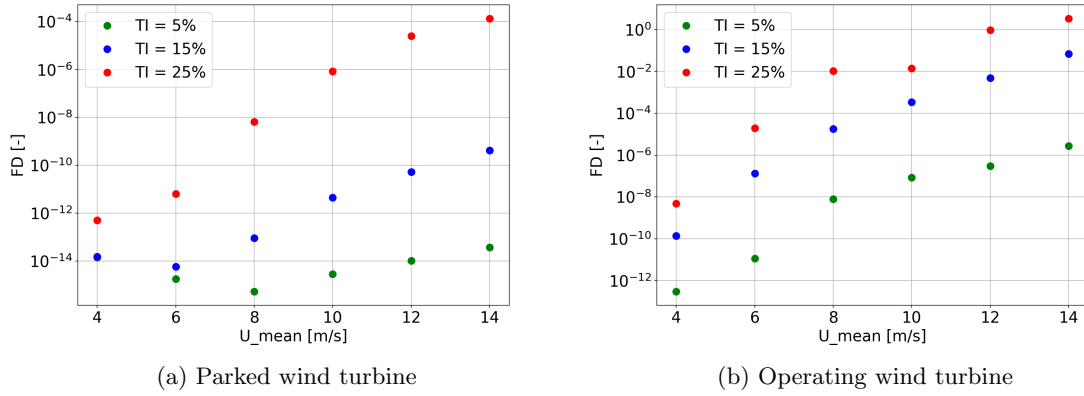
Figure 5.30: 20-year fatigue damage results in the pontoon (P1.2) due to wind loads alone

Table 5.16 and Table 5.17 provide insights into the fatigue damage values for both operating and parked wind turbines, where the tendencies are illustrated in Figure 5.30. In Table 5.16, the fatigue damage values exhibit relatively low values for all turbulence intensity levels, indicating reduced stress and fatigue at lower wind speeds. However, as wind speed increases, fatigue damage values increases significantly, particularly in the presence of higher turbulence intensity.

The rotating wind turbine encounters higher levels of stress and fatigue in contrast to the parked wind turbine scenario, even when subjected to the same wind speed and turbulence intensity combinations. Similar to the parked wind turbine, the fatigue damage values for the operating wind turbine generally increase with increasing wind speed and turbulence intensity. Notably, the influence of turbulence intensity on fatigue damage becomes more pronounced in the rotating wind turbine scenario. This underscores the crucial importance of considering wind conditions and turbulence intensity during wind turbine design and operation to mitigate fatigue damage effectively.
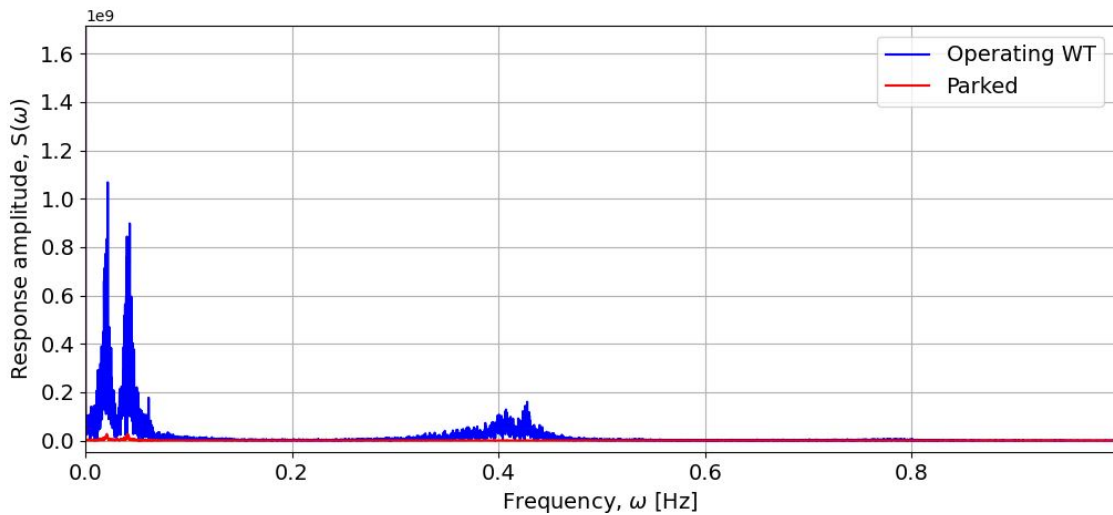
Figure 5.31: Response spectrum of bending moments for parked and operating WT in the pontoon

Interestingly, comparing the response spectrum of the most extreme condition (TI = 25% and Uw = 14 m/s) for the parked and operating WT in the pontoon, Figure 5.30, with the response spectrum in the tower base, Figure 5.31, it is evident the wind spectrum contributes immensely to the tower base. The response due to 3P-frequency and tower eigenfrequency is present, however, smaller than in the tower base. Contrary to the response spectrum of the tower base, the spectrum does not follow the Kaimal spectrum, confirming that the wind velocity itself does not affect as much in the pontoon as in tower base. However, at lower frequencies, two peaks appear. The first

peak is at 0.021 Hz, and the second peak is at 0.042 Hz, or 47.6 s and 23.8 s, respectively. The second peak can be linked to rigid body motions, either in heave or roll and pitch. The first peak is due to the wind loads.

For both parked and operating WT, the fatigue damages in the pontoon are generally lower, particularly for lower turbulence intensity and mean velocities. Notably, for the highest wind condition (TI = 25% and Uw = 14 m/s), the fatigue damage is 3.4019 in the pontoon and 8.50 in the tower base for the operating wind turbine, while for the lowest wind condition (TI = 5% and Uw = 4 m/s), it is 3.01e-13 in the pontoon and 1.38e-6 in the tower base. This suggests that fatigue at lower velocities and turbulence intensities is more affected by the rotor in the tower base than in the pontoon. Furthermore, higher values of fatigue damage are primarily due to the wind and turbulence intensity, which contribute significantly to bending moments and fatigue damage. This observation is illustrated in Figure 5.30. The figure clearly shows that the differences in fatigue damage values are more noticeable in the parked wind turbine scenario, primarily for higher wind velocities. Meanwhile, the differences in fatigue damage for the same values are less prominent in the operating wind turbine case.

Comparing the two cross-sections in the pontoons, slight differences can be observed. The fatigue damage results in the cross-section furthest away from the tower (P1.1) are listed in Table 5.18 and Table 5.19, and illustrated in Figure 5.32. The fatigue damage results show a similar trend as the tower base and pontoon section close to the tower (P1.2). In the case of the parked WT, the initial fatigue damage decreases for low TI until a certain point, after which it increases. Additionally, the fatigue damage generally increases with increasing wind velocities. Similarly, as the TI increases, the fatigue damage also increases, which is more prominent for the parked WT than for the operating WT.

FD [-]		TI [%]		
		5	15	25
	4	8.36e-14	8.69e-14	9.00e-13
	6	8.93e-15	1.72e-14	7.40e-12
Uw	8	1.60e-15	1.15e-13	6.55e-09
[m/s]	10	5.98e-15	5.75e-12	8.43e-07
	12	2.02e-14	6.02e-11	2.53e-05
	14	4.95e-14	4.12e-10	0.00013

Table 5.18: 20-year FD results in the pontoon (P1.1), wind alone for parked wind turbine

FD [-]		TI [%]		
		5	15	25
	4	5.93e-14	4.76e-11	2.53e-09
	6	5.35e-12	1.12e-07	1.82e-05
Uw	8	6.69e-09	1.67e-05	0.01018
[m/s]	10	6.23e-08	0.00031	0.01340
	12	2.43e-07	0.00474	0.90614
	14	2.23e-06	0.06649	3.35284

Table 5.19: 20-year FD results in the pontoon (P1.1), wind alone for operating wind turbine
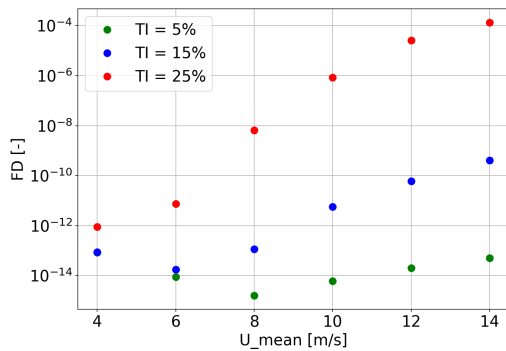
(a) Parked wind turbine
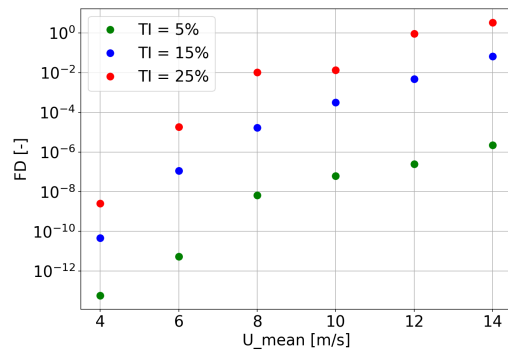
(b) Operating wind turbine

Figure 5.32: 20-year fatigue damage results in pontoon (P1.1) due to wind loads alone

The fatigue damage on the parked WT is higher for low velocities and TI compared to the column close to the tower, but lower for higher values of both parameters. This implies that environmental conditions create higher fatigue damage for the section close to the tower, as the bending moments affect that section more significantly.

By observing the difference in the two cross-sections of the pontoon, there is a slightly lower value for the cross-section furthest away from the tower. This further confirms that the 3P-frequency and tower eigenfrequency have an impact on fatigue damage, also in the pontoon. However, as the differences in the cross-sections are minor, it is evident that the differences between parked and operating wind turbines are crucial when simulating fatigue damage.

Moreover, fatigue damage is slightly lower than the fatigue damage found in P1.2. However, in Figure 5.33 is the response spectrum of the bending moments in the y-direction for Hs = 2.5m and Tp = 7.5 s for the cross-sections P1.2 and P1.1 illustrated. It can be observed close to no differences for the two main peaks at 0.021 Hz and 0.042 Hz, indicating both cross-sections are similarly affected by the wind loads. However, there are slightly noticeable differences in the frequency in the 3P-frequency and tower eigenfrequency range. This is evident that the cross-section closer to the tower is more affected by the tower effects than the section located further away.
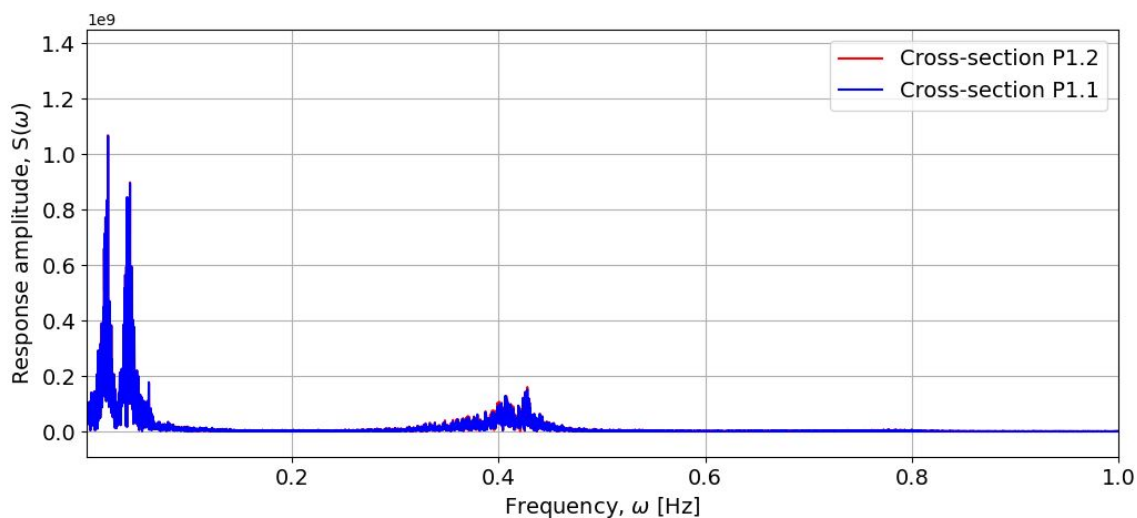
Figure 5.33: Comparison of the response of bending moments for spectrum due to wind in cross-sections P1.2 and P1.1

5.11 Analysis of Combined Wind and Wave Loads

This section investigates the combined contribution of wind and wave loads to the fatigue damage (FD) experienced by the floater and tower base. It compares the FD resulting from combined loads with that from individual wind and wave loads, providing insights into load interactions and their effects on specific sections of the turbine.

Environmental conditions used for the analyses, such as significant wave height, peak wave period, wind velocity, and turbulence intensity, are presented in Table 5.20. Simulations considering combined environmental loads are compared to results obtained from adding wave and wind loads separately. This allows for observation of distinct effects on fatigue damage experienced by different cross sections.

Condition	Wave height [m]	Wave period [s]	Wind velocity [m/s]	Turbulence Intensity [%]
1	0.5	4.5	4	5
2	0.5	4.5	14	25
3	2.5	9.5	4	5
4	2.5	9.5	14	25

Table 5.20: Environmental conditions for combined simulations

5.11.1 Fatigue Damage in the Tower Base Due to Combined Loads

The results of combining wind and waves for a parked wind turbine are presented in Table 5.21, while the results for an operating wind turbine are shown in Table 5.22. Similar observations are found for the simulations involving alone wind or wave loads. For a parked wind turbine, the waves contribute the most to fatigue damage. On the other hand, for an operating wind turbine, the wind contributes significantly as well. Observing the fatigue damage for the operating WT the influence of the rotor is tremendous.

Condition	Fatigue damage [-]	
	Combined simulations	Sum of Wind and Wave alone simulations
1	0.0002	0.0015
2	0.0042	0.0029
3	0.527	0.8780
4	1.004	0.8794

Table 5.21: 20-year fatigue damage results in the tower base due to combined wave and wind loads for the parked wind turbine

Condition	Fatigue damage [-]	
	Combined simulations	Sum of Wind and Wave alone simulations
1	1.61e-05	1.24e-05
2	5.679	8.591
3	0.747	0.827
4	7.598	9.418

Table 5.22: 20-year fatigue damage results in the tower base due to combined wave and wind loads for the operating wind turbine

Upon observing the fatigue damage results, it is evident that they generally follow similar trends as observed in simulations with exclusively wind or wave loads. In the case of low wind and small waves (condition 1), the fatigue damage decreases for the operating WT compared to the parked WT. This can be attributed to the response of the turbine controller, which adjusts the pitch angles and reduces structural damage. The differences between parked and operating wind turbines can also be observed for high wind conditions in conditions 2 and 4. The interaction between an operating wind turbine and the wind loads results in significantly higher fatigue damage, as seen in simulations considering wind loads alone.

The parked wind turbine exhibits a pronounced trend. For conditions with low wind values (conditions 1 and 3), the fatigue damage in combined simulations is lower than the sum of the loads considered separately. Contrarily, for high wind conditions, the fatigue damage is higher than the summation, particularly evident in conditions 3 and 4. This demonstrates how the wind turbine loads interact and counteract some of the effects of low wind values, while higher wind conditions enhance fatigue damage. The response spectrum of the bending moments in the y-direction in the tower base for conditions 3 and 4 is illustrated in Figure 5.34 and Figure 5.35, respectively. It is apparent that both cases are influenced by wave loads, with lower response compared to simulations considering wave loads alone. Additionally, the peak response at 0.03 Hz appears to be lower in the combined simulations for the parked wind turbine compared to both wind and wave-alone simulations. On the other hand, in the case of condition 4, the combined simulation results are noticeably influenced by wind loads acting on the structure. The response follows a similar pattern as wind-alone simulations for lower frequencies.
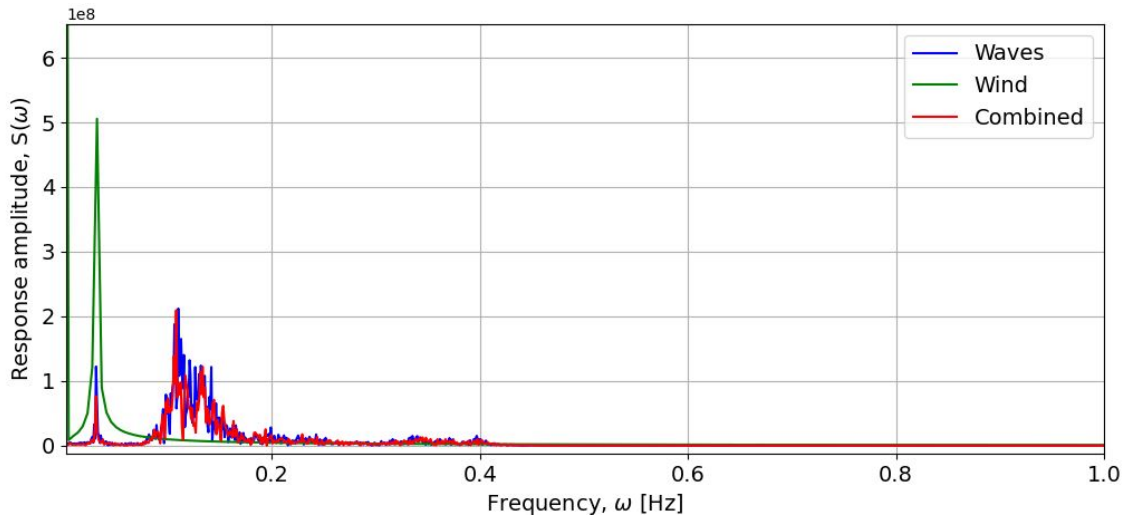
Figure 5.34: Comparison of response spectrum of bending moments for the parked wind turbine with environmental condition corresponding to condition 3
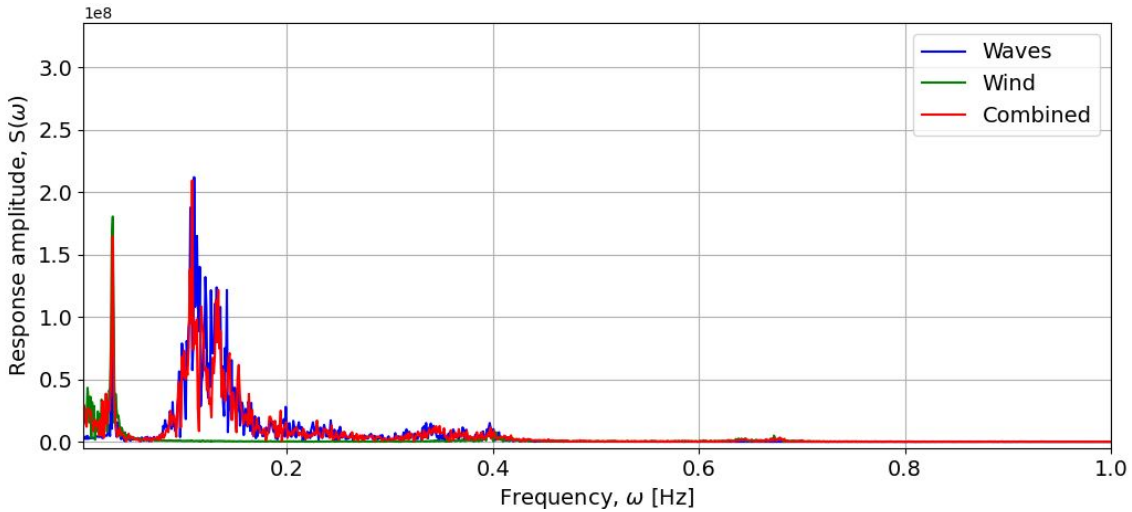

Figure 5.35: Comparison of response spectrum of bending moments for the parked wind turbine with environmental condition corresponding to condition 4

The fatigue damage values for the operating wind turbine generally exhibit higher values when considering the summation of wind and wave load simulations alone. This observation suggests the presence of cancellation effects resulting from the combination of loads. Figure 5.36 and Figure 5.37 show the differences between the wind and wave load simulations and the combined simulations for bending moments in the tower base for conditions 3 and 4, respectively. From these figures, it is evident that the bending moments in the combined simulations are generally lower compared to the responses from both wind and wave load simulations alone. This is particularly noticeable for frequencies where the wind-alone simulations exhibit a response, as the combined simulation responses are lower. The same trend can be observed for the wave-alone simulations as well. This further confirms the higher fatigue damage observed when considering the summation of wind and wave fatigue damage, as compared to the results obtained from the combined simulations.

Generally, the combined simulations result in lower fatigue damage, except for the parked wind turbine for high wind conditions in condition 3. A wind speed of 14 m/s is most likely a wind condition for the wind turbine to operate, as this is within Region 2, and the cut-out wind speed is at 25 m/s. However, with unrealistically high TI, the wind turbine is expected to experience larger responses. As discussed in Section 5.9.2, the difference between the parked and the operating wind turbine is evident in the pitch angle. The controller reacts due to the increasing pitch angle and

stabilizes the wind turbine. Without this controller operation, combined with large waves, the fatigue damage appears to enhance compared to the summation of the corresponding conditions of wave and wind alone.
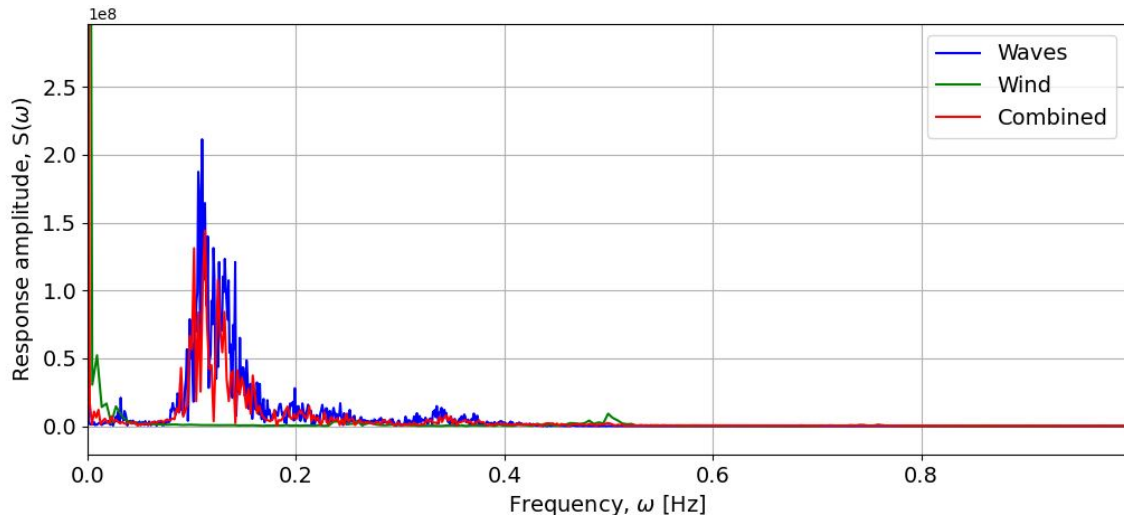
Figure 5.36: Comparison of response spectrum of bending moments for the operating wind turbine with environmental condition corresponding to condition 3
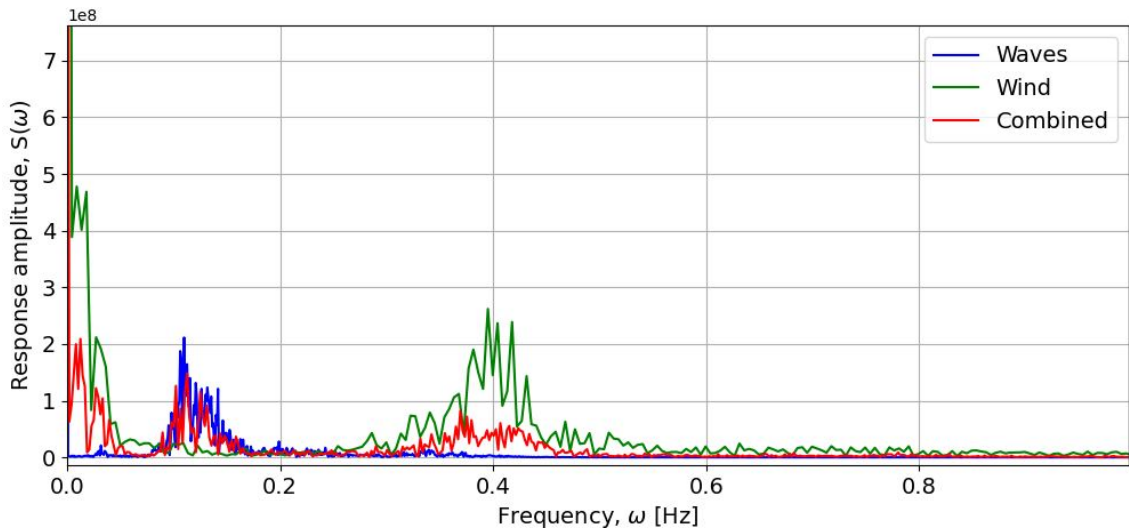
Figure 5.37: Comparison of response spectrum of bending moments for the operating wind turbine with environmental condition corresponding to condition 4

5.11.2 Fatigue Damage in the Pontoon Due to Combined Loads

In the case of the pontoon, the fatigue damage results generally depict the same trend as for wind and wave loads alone, presented in Table 5.23 and Table 5.24.

For conditions 1 and 3, the fatigue damage of the parked wind turbine is higher than for the operating wind turbine. This applies to both the combined simulations and the summation of the wind and wave simulations. This further confirms the findings of the tower base cross-section, and that for low wind conditions, the operating wind turbine regulates the pitch angle and reduces the damage to the structure.

Contrary to the tower base, it can be observed that the combined simulation fatigue damage are higher for both condition 3 and 4 for both the parked and operating wind turbine. It appears that

Condition	Fatigue damage [-]	
	Combined simulations	Sum of Wind and Wave alone simulations
1	2.72e-10	4.23e-10
2	1.14e-07	0.00015
3	0.00129	0.00020
4	0.00180	0.00106

Table 5.23: 20-year fatigue damage results in the pontoon cross-section P1.2 due to combined wave and wind loads for the parked wind turbine

Condition	Fatigue damage [-]	
	Combined simulations	Sum of Wind and Wave alone simulations
1	1.72e-10	4.06e-11
2	4.5558	3.40193
3	0.00111	0.00019
4	4.5778	3.4029

Table 5.24: 20-year fatigue damage results in the pontoon cross-section P1.2 due to combined wave and wind loads for the operating wind turbine

the combined simulation experience higher fatigue damage in the pontoon. The response spectrum of the parked and operating wind turbine for the bending moments in condition 4 is illustrated in Figure 5.38 and Figure 5.39. This goes to show how the combined simulations depict higher fatigue damage.
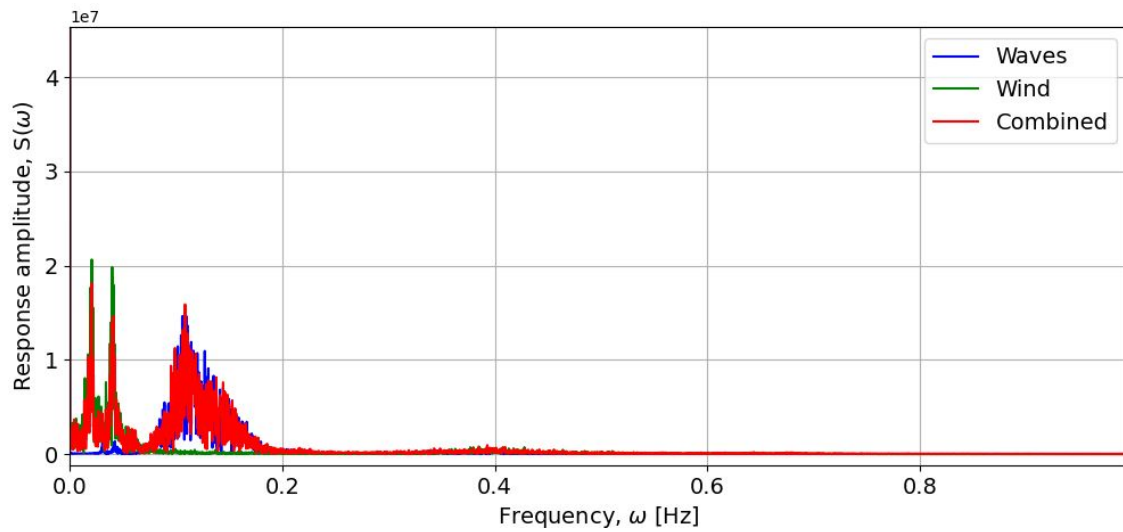

Figure 5.38: Response spectrum of bending moments in the pontoon cross-section P1.2, for parked wind turbine
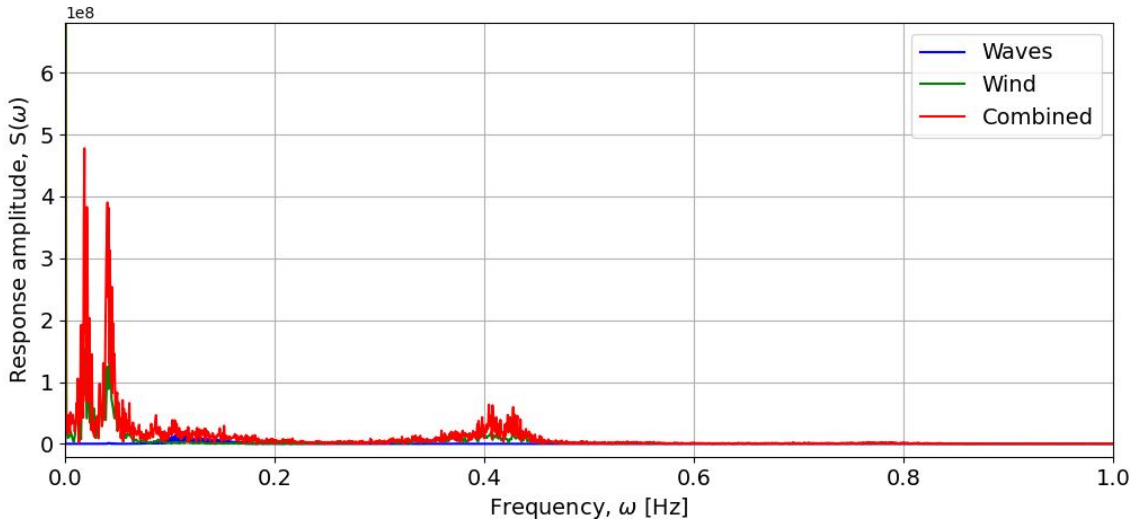
Figure 5.39: Response spectrum of bending moments in pontoon cross-section P1.2, for operating wind turbine

Further, the combined simulation can be compared to the results from the cross-section of the pontoon located furthest away from the tower, P1.1. Generally, the tendencies in this cross-section are the same as for the wind and wave load simulations, as illustrated in Table 5.25 and Table 5.26. However, adding the results, it is apparent that the results are higher than the combined wind and wave loads simulations for the operating wind turbine. The loads acting on the structure in a location further away from the tower appear to have a canceling effect, compared to the cross-section closer to the tower. In contrast, the results were higher for the combined simulations. As for the parked wind turbine, the fatigue damage results appear higher for the combined simulations than the direct summation of damage contributions due to wind and waves separately.

| Condition | Fatigue damage [-] | |
	Combined simulations	Sum of Wind and Wave alone simulations
1	7.55e-10	6.736e-10
2	4.048e-05	0.00013
3	0.00011	9.27e-05
4	0.00339	0.00023

Table 5.25: 20-year fatigue damage results in the pontoon cross-section P1.1 due to combined wave and wind loads for the parked wind turbine

| Condition | Fatigue damage [-] | |
	Combined simulations	Sum of Wind and Wave alone simulations
1	1.45e-10	5.22e-11
2	2.0963	3.3528
3	4.30e-05	8.80e-05
4	2.0241	3.3529

Table 5.26: 20-year fatigue damage results in the pontoon cross-section P1.1 due to combined wave and wind loads for the operating wind turbine

Chapter 6

Conclusion

This section aims to provide a summary and conclusion of the findings of the thesis. It contains the validation of the Modified wind turbine (WT) model compared to the Rigid WT model and the outcomes obtained from NREL, frequency-domain analysis, and analytical results. The conclusions from the fatigue damage analyses, considering wave loads alone, wind loads alone, and the combined loads, are also presented. Additionally, potential further work for future research is highlighted.

6.1   Validations of Models

This Master's thesis analyzed a Modified WT model, comparing it to the Rigid WT model and results from the National Renewable Energy Laboratory (NREL). Various tests evaluated the behavior and characteristics of the Modified WT model.

Results showed that the Modified WT model exhibited slight differences from the Rigid WT and NREL results, including damping effects in the response spectrum and motion plots. Nevertheless, the eigenvalues were found to be adequately similar to the result obtained from the Rigid WT model and NREL. The added mass obtained from HydroD simulations aligned well with NREL results, while the Response Amplitude Operator (RAO) showed similar frequency peaks for the Modified and Rigid WT models. However, there were noticeable differences in magnitude, suggesting potential variations in hydrodynamic forces. Examining the damping coefficients obtained from the PQ-analyses, revealed differences in hydrodynamic and structural damping coefficients, highlighting the role of structural damping.

Controller validation through wind tests confirmed desired performance in regulating the behavior of the Modified WT model under varying wind conditions, although some peak shaving occurred. Comparing the Rigid and Modified WT models in terms of fatigue damages revealed higher flexibility in the Modified WT model, which could affect component durability and longevity. Furthermore, the eigenvalue analysis investigated natural tower frequencies, indicating a lower eigenfrequency compared to NREL and Rigid WT model results, in correlation to a study by Li et al. and confirming the accuracy of the Modified WT model. Sensitivity tests validated modeling choices for various aspects, such as mooring line modeling, timesteps, pontoon elements, and seed numbers, verifying the accuracy of the Modified WT model and simulations.

In conclusion, this Master's thesis comprehensively evaluated the Modified WT model, demonstrating improved dynamic behavior, performance under different conditions, and flexibility. The findings were believed to contribute to achieving a better understanding of the model.

6.2 Fatigue Damage Analysis Results

The simulations in SIMA provided important insights into the impact of wave loads, wind loads, and their combination on wind turbine fatigue damage. When considering wave loads alone, higher wave heights increased the fatigue damages, particularly during peak periods of 7.5 s and 8.5 s, due to excitation forces. The tower base cross-section experienced significantly higher fatigue damage compared to the pontoons. This was found to be due to the wave energy being decreased at the depth of the pontoon cross-sections. Furthermore, the effect of an active controller was observed, as the fatigue damage for operating WT was lower than for the parked WT.

In the case of wind loads alone, the fatigue damages increased with higher wind speeds, especially when accompanied by high turbulence intensity. The influence of the rotor on fatigue damage was more pronounced for operating wind turbines than parked turbines. This revealed how significant the effect of a rotating rotor is on a wind turbine, as the passing of blades leads to larger fatigue damage. Unlike wave loads, the considerable difference in fatigue damage between the tower base and pontoons was not as present considering wind loads alone as for the waves alone. This demonstrated the significant impact of wind-induced bending moments on both the pontoons and the tower base.

Considering the combined effect of wind and wave loads, simulations showed higher fatigue damage for parked wind turbines under high environmental conditions compared to the sum of the individual fatigue contributions from wind and wave loads. However, the combined simulations exhibited lower fatigue damage for low environmental conditions. As for the operating wind turbine, the summation of loads showed generally higher fatigue damage than the combined simulations. Yet, this did not apply to the cross-section in the pontoon closest to the tower. Contrary to the two other cross-sections, this section experienced higher fatigue damage for the combined than the summation of loads. In this cross-section, the loads appeared to interact and enhance the total stress on the structure.

In summary, these simulations emphasized the importance of wave heights, wind speeds, turbulence intensity, and the operational status of the turbines concerning influencing fatigue damage. The findings generally suggested that finding the fatigue damage due to the summation of wind and wave loads was conservative. However, fatigue damage due to combined simulation was higher in several cases, indicating the need for coupled wave and wind simulations during the early stages of wind turbine design. Analyzing wave and wind loads individually contributed to more profound insights into their contributions.

6.3 Further Work

This thesis has presented the work done in doing fatigue damage analysis with respect to wind and wave loads. This has been done in the fully coupled analysis tool SIMA. To get a more comprehensive understanding of how fatigue damage develops due to wind and wave loads, many more investigations could be done if there were more time.

- **Further work on the flexible model with RIFLEX elements:** Further work on the flexible model, with RIFLEX elements of the columns as well as the pontoon, could provide more insights into the fatigue damage of the structure. This aims to improve the representation of a real-life flexible wind turbine by incorporating flexible elements into the model. By analyzing the fatigue damage of the structure with flexible columns and a pontoon, a more realistic understanding of the impact of flexibility on fatigue can be gained.

- **Investigation of the ultimate limit state (ULS) and structure flexibility:** Including ULS analysis in the research would allow for studying the behavior of the structure under extreme loading conditions. This would provide insights into how the flexibility of the structure affects its performance and durability in critical situations. This could be a further investigation of the flexibility of numerical models compared to experimental models.

- **Local analysis of cross-sections and modeling structural details:** By conducting a more detailed analysis of cross-sections, including modeling specific features like stiffeners, welds, and other details, a deeper understanding of how wind and wave loads affect different parts of the structure can be obtained. This would provide more precise information on the localized areas prone to fatigue damage.

- **Investigation of a wider range of wind and wave loads:** Expanding the range of wind velocities, including conditions closer to the rated wind speed, and exploring various combinations of significant wave heights and peak periods provide a more comprehensive understanding of the impact the loads have on the fatigue damage.

- **Exploring different directions of wind and wave loads:** This suggestion involves varying the direction of wind and wave loads in the analysis. By simulating different angles and observing the resulting fatigue damage, the research can explore the directional sensitivity of the structure and compare the cumulative fatigue damage between combined simulations and individual load simulations. It would also be interesting to observe how the fatigue damage evolves if the wind and wave loads have different angles, and how the summation of fatigue damage compares to the combined simulations.

Bibliography

[1] O. Edenhofer, R. Pichs-Madruga, Y. Sokona, K. Seyboth, S. Kadner, T. Zwickel, P. Eicke-meier, G. Hansen, S. Schlömer, C. von Stechow, *et al.*, *Renewable energy sources and climate change mitigation: Special report of the intergovernmental panel on climate change.* Cambridge University Press, 2011.

[2] DHI, "Decode offshore wind engineering challenges at every stage," 2021.

[3] F. Håland, "Combining fully coupled analysis and linear potential theory time domain analysis to obtain cross-sectional loads in the substructure of a floating offshore wind turbine," Master's thesis, NTNU, 2022.

[4] C. Allen, A. Viscelli, H. Dagher, A. Goupee, E. Gaertner, N. Abbas, M. Hall, and G. Barter, "Definition of the umaine volturnus-s reference platform developed for the iea wind 15-megawatt offshore reference wind turbine," tech. rep., National Renewable Energy Lab.(NREL), Golden, CO (United States); Univ. of ..., 2020.

[5] O. Faltinsen, *Sea loads on ships and offshore structures*, vol. 1. Cambridge university press, 1993.

[6] M. Hansen, *Aerodynamics of wind turbines*. Routledge, 2015.

[7] E. Gaertner, J. Rinker, L. Sethuraman, F. Zahle, B. Anderson, G. Barter, N. Abbas, F. Meng, P. Bortolotti, W. Skrzypinski, *et al.*, "Definition of the iea 15-megawatt offshore reference wind turbine," 2020.

[8] T. J. Larsen and T. D. Hanson, "A method to avoid negative damped low frequent tower vibrations for a floating, pitch controlled wind turbine," in *Journal of Physics: Conference Series*, vol. 75, p. 012073, IOP Publishing, 2007.

[9] NTNU, "3 sea state parameters and engineering wave spectra," 1999.

[10] T. Burton, N. Jenkins, D. Sharpe, and E. Bossanyi, *Wind energy handbook.* John Wiley & Sons, 2011.

[11] I. Langen and R. Sigbjörnsson, *Dynamisk analyse av konstruksjoner: Dynamic analysis of structures.* Tapir, 1979.

[12] E. E. Bachynski, "Design and dynamic analysis of tension leg platform wind turbines," 2014.

[13] M. I. Kvittem, "Modelling and response analysis for fatigue design of a semi-submersible wind turbine," 2014.

[14] I. Rychlik, "A new definition of the rainflow cycle counting method," *International journal of fatigue*, vol. 9, no. 2, pp. 119–121, 1987.

[15] S. Ocean, "Riflex 4.10. 3 user guide," 2017.

[16] Q. Wang, "Design of a steel pontoon-type semi-submersible floater supporting the dtu 10mw reference turbine," 2014.

[17] B. J. Jonkman, "Turbsim user's guide: Version 1.50," tech. rep., National Renewable Energy Lab.(NREL), Golden, CO (United States), 2009.

[18] D. S. at DNV, "Sesam: Software suite for hydrodynamic and structural analysis of renewable, offshore and maritime structures."

[19] E. M. Sunderland, A. Amirbahman, N. M. Burgess, J. Dalziel, G. Harding, S. H. Jones, E. Kamai, M. R. Karagas, X. Shi, and C. Y. Chen, "Mercury sources and fate in the gulf of maine," *Environmental Research*, vol. 119, pp. 27–41, 2012.

[20] W. Turbines, "Part 1: Design requirements, iec 61400-1," *International Electrotechnical Commission: Geneva, Switzerland*, 2005.

[21] P. Gonzalez, G. Sanchez, A. Llana, and G. Gonzalez, "Deliverable 1.1 oceanographic and meteorological conditions for the design," tech. rep., LIFES50+, 2015.

[22] DNV, "Fatigue design of offshore steel structures," tech. rep., DNV-RP-C203, 2011.

[23] H. Li, Z. Gao, E. Bachynski-Polić, Y. Zhao, and S. Fiskvik, "Effect of floater flexibility on global dynamic responses of a 15-mw semi-submersible floating wind turbine," *Available at SSRN 4455719*.

[24] 7Waves, "About us."

[25] O. Rsted, "Making green energy affordable-how the offshore wind energy industry matured and what we can learn from it," *Ørsted: Fredericia, Denmark*, 2019.

[26] W. W. E. Association *et al.*, "World market for wind power saw another record year in 2021: 97, 3 gigawatt of new capacity added," 2022.

[27] A. R. Henderson, *Analysis tools for large floating offshore wind farms*. University of London, University College London (United Kingdom), 2000.

[28] T.-T. Tran and D. Lee, "Development of jacket substructure systems supporting 3mw offshore wind turbine for deep water sites in south korea," *International Journal of Naval Architecture and Ocean Engineering*, vol. 14, p. 100451, 2022.

[29] L. Oftedahl, "Havvind: – det haster om norge skal ta ledertrøya," 2022.

[30] S. Rodriguez and J. Jaworski, "Strongly-coupled aeroelastic free-vortex wake framework for floating offshore wind turbine rotors. part 2: Application," *Renewable Energy*, vol. 149, pp. 1018–1032, 10 2019.

[31] A. Du, "Semi-submersible, spar and tlp. how to select floating wind foundation types?," 2021.

[32] A. R. Winslow, "Urban wind generation: comparing horizontal and vertical axis wind turbines at clark university in worcester, massachusetts," 2017.

[33] TWI-global, "Addressing the challenges of offshore wind?."

[34] M. Hall and A. Goupee, "Validation of a lumped-mass mooring line model with deepcwind semisubmersible model test data," *Ocean Engineering*, vol. 104, pp. 590–603, 2015.

[35] A. J. Coulling, A. J. Goupee, A. N. Robertson, J. M. Jonkman, and H. J. Dagher, "Validation of a fast semi-submersible floating wind turbine numerical model with deepcwind test data," *Journal of Renewable and Sustainable Energy*, vol. 5, no. 2, p. 023116, 2013.

[36] D.-C. Lee, S.-k. Na, S. Kim, and C.-w. Kim, "Deterministic fatigue damage evaluation of semi-submersible platform for wind turbines using hydrodynamic-structure interaction analysis," *International Journal of Precision Engineering and Manufacturing-Green Technology*, vol. 9, no. 5, pp. 1317–1328, 2022.

[37] S. Netzband, C. W. Schulz, U. Göttsche, D. Ferreira González, and M. Abdel-Maksoud, "A panel method for floating offshore wind turbine simulations with fully integrated aero-and hydrodynamic modelling in time domain," *Ship Technology Research*, vol. 65, no. 3, pp. 123–136, 2018.

[38] L. Zhang, W. Shi, M. Karimirad, C. Michailides, and Z. Jiang, "Second-order hydrodynamic effects on the response of three semisubmersible floating offshore wind turbines," *Ocean Engineering*, vol. 207, p. 107371, 2020.

[39] Z. Zhao, W. Wang, W. Shi, and X. Li, "Effects of second-order hydrodynamics on an ultra-large semi-submersible floating offshore wind turbine," in *Structures*, vol. 28, pp. 2260–2275, Elsevier, 2020.

[40] X. Mei and M. Xiong, "Effects of second-order hydrodynamics on the dynamic responses and fatigue damage of a 15 mw floating offshore wind turbine," *Journal of Marine Science and Engineering*, vol. 9, no. 11, p. 1232, 2021.

[41] M. I. Kvittem and T. Moan, "Time domain analysis procedures for fatigue assessment of a semi-submersible wind turbine," *Marine Structures*, vol. 40, pp. 38–59, 2015.

[42] E. Uzunoglu, D. Karmakar, and C. Guedes Soares, "Floating offshore wind platforms," in *Floating offshore wind farms*, pp. 53–76, Springer, 2016.

[43] C. Bjerkseter and A. Ågotnes, "Levelised costs of energy for offshore floating wind turbine concepts," Master's thesis, Norwegian University of Life Sciences, Ås, 2013.

[44] F. F. IRENA, "A game changer for offshore wind power," *International Renewable Energy Agency, Abu Dhabi*, 2016.

[45] D. Roddier, C. Cermelli, and A. Weinstein, "Windfloat: a floating foundation for offshore wind turbines—part i: design basis and qualification process," in *International Conference on Offshore Mechanics and Arctic Engineering*, vol. 43444, pp. 845–853, 2009.

[46] A. Aubault, C. Cermelli, and D. Roddier, "Windfloat: A floating foundation for offshore wind turbines—part iii: Structural analysis," in *International Conference on Offshore Mechanics and Arctic Engineering*, vol. 43413, pp. 213–220, 2009.

[47] C. Cermelli, D. Roddier, and A. Aubault, "Windfloat: a floating foundation for offshore wind turbines—part ii: hydrodynamics analysis," in *International conference on offshore mechanics and arctic engineering*, vol. 43444, pp. 135–143, 2009.

[48] T. Duarte, S. Price, A. Peiffer, and J. M. Pinheiro, "Windfloat atlantic project: Technology development towards commercial wind farms," in *Offshore Technology Conference*, OnePetro, 2022.

[49] K. Xu, K. Larsen, Y. Shao, M. Zhang, Z. Gao, and T. Moan, "Design and comparative analysis of alternative mooring systems for floating wind turbines in shallow water with emphasis on ultimate limit state design," *Ocean Engineering*, vol. 219, p. 108377, 2021.

[50] Y. Liu, S. Li, Q. Yi, and D. Chen, "Developments in semi-submersible floating foundations supporting wind turbines: A comprehensive review," *Renewable and Sustainable Energy Reviews*, vol. 60, pp. 433–449, 2016.

[51] M. Le Boulluec, J. Ohana, A. Martin, and A. Houmard, "Tank testing of a new concept of floating offshore wind turbine," in *International Conference on Offshore Mechanics and Arctic Engineering*, vol. 55423, p. V008T09A100, American Society of Mechanical Engineers, 2013.

[52] K. F. Svendsen, "Structural design and dynamic analysis of a tension leg platform wind turbine, considering elasticity in the hull," Master's thesis, NTNU, 2016.

[53] J. M. Jonkman and K. Shaler, *Fast. farm user's guide and theory manual*. National Renewable Energy Laboratory Golden, CO, 2021.

[54] Y. Ma, "Novel modeling and fatigue analysis for early-phase design of a 15-mw fowt," Master's thesis, NTNU, 2022.

[55] M. Kim and D. Yue, "The nonlinear sum-frequency wave excitation and response of a tension-leg platform," 1988.

[56] S. K. Chakrabarti, *Hydrodynamics of offshore structures*. WIT press, 1987.

[57] J. F. Manwell, J. G. McGowan, and A. L. Rogers, *Wind energy explained: theory, design and application*. John Wiley & Sons, 2010.

[58] S. Ocean, "Simo 4.10. 3 user guide," 2017.

[59] J. Katz and A. Plotkin, *Low-speed aerodynamics*, vol. 13. Cambridge university press, 2001.

[60] J. McGowan, A. Rogers, and J. Manwell, "Wind energy explained: Theory, desing and application england: John wiley and sons, ltd," 2009.

[61] J. Chen, Z. Hu, G. Liu, and D. Wan, "Coupled aero-hydro-servo-elastic methods for floating wind turbines," *Renewable energy*, vol. 130, pp. 139–153, 2019.

[62] L. H. Holthuijsen, *Waves in oceanic and coastal waters*. Cambridge university press, 2010.

[63] N. D. Katopodes, *Free-Surface Flow:: Shallow Water Dynamics*. Butterworth-Heinemann, 2018.

[64] DNV, "Environmental conditions and environmental loads," tech. rep., DNV-RP-C205, 2010.

[65] A. Naess and T. Moan, *Stochastic dynamics of marine structures*. Cambridge University Press, 2013.

[66] J. N. Newman, *Marine hydrodynamics*. The MIT press, 2018.

[67] J. K. Paik and A. K. Thayamballi, *Ultimate limit state design of steel-plated structures*. John Wiley & Sons, 2003.

[68] DNV, "Design of offshore wind turbine structures," tech. rep., DNV-OS-J101, 2014.

[69] M. Masciola, A. Robertson, J. Jonkman, and F. Driscoll, "Investigation of a fast-orcaflex coupling module for integrating turbine and mooring dynamics of offshore floating wind turbines," tech. rep., National Renewable Energy Lab.(NREL), Golden, CO (United States), 2011.

[70] A. Cordle and J. Jonkman, "State of the art in floating wind turbine design tools," in *The twenty-first international offshore and polar engineering conference*, OnePetro, 2011.

[71] N. Johnson, J. Jonkman, A. Wright, G. Hayman, and A. Robertson, "Verification of floating offshore wind linearization functionality in openfast," in *Journal of Physics: Conference Series*, vol. 1356, p. 012022, IOP Publishing, 2019.

[72] SIMA, "Marine operations and mooring analysis software," 2019.

[73] H. Ormberg and E. E. Bachynski, "Global analysis of floating wind turbines: Code development, model sensitivity and benchmark study," in *The Twenty-second International Offshore and Polar Engineering Conference*, OnePetro, 2012.

[74] A. Robertson, J. Jonkman, M. Masciola, H. Song, A. Goupee, A. Coulling, and C. Luan, "Definition of the semisubmersible floating system for phase ii of oc4," tech. rep., National Renewable Energy Lab.(NREL), Golden, CO (United States), 2014.

[75] DNV, "Position mooring," tech. rep., DNVGL-OS-E301, 2015.

[76] DNV, "Design of floating wind turbine structures," tech. rep., DNV-OS-J103, 2013.

[77] DNV, "Floating wind turbine structures," tech. rep., DNV-ST-0119, 2021.

[78] W. Turbines, "Part 2: Safety of small wind turbines, iec 61400-2," *International Electrotechnical Commission: Geneva, Switzerland*.

[79] W. Turbines, "Part 3: Design requirements for offshore wind turbines, iec 61400-3," *International Electrotechnical Commission: Geneva, Switzerland*.

[80] P. Gipe and E. Möllerström, "An overview of the history of wind turbine development: Part i—the early wind turbines until the 1960s," *Wind Engineering*, vol. 46, no. 6, pp. 1973–2004, 2022.

[81] P. Watson and B. Dabell, "Cycle counting and fatigue d~ 1age," *Society'of Enfironmental Engineers*, 1975.

[82] N. Hong, "A modified rainflow counting method," *International Journal of Fatigue*, vol. 13, no. 6, pp. 465–469, 1991.

[83] S. K. Chakrabarti, *Handbook of Offshore Engineering (2-volume set)*. Elsevier, 2005.

Appendix A

Unresolved Attempted Models

A.1 Sesam Wind Manager

An attempt was undertaken to employ the DNV Sesam Wind Manager to conduct a local analysis of the wind turbine. However, it proved to be more time-consuming than predicted. The use of this software required a Wasim file from HydroD, which in turn needed a .pln-file. Generating a .pln-file is a detailed and time-consuming process that is highly sensitive to minor adjustments. Consequently, it is crucial to model each component in detail.

The invalidity of the model depicted in Figure A.1 may originate from the manner in which the 'curve lines' are represented in GeniE. Nevertheless, various combinations were attempted, yielding similar or unsatisfying outcomes. Another approach explored involved directly modeling the structure as a whole in HydroD, resulting in the outcomes depicted in Figure A.1. This gave the most successful attempt. However, only one of the pontoons meshed, and the cylinders lacked adequate surface representation. Consequently, it was determined that this method would demand excessive time and effort compared to the benefits it would yield.

An alternative approach could involve modeling only one-third of the floater to observe local responses in that specific area. Additional time would also afford the opportunity to familiarize and adapt to the program.
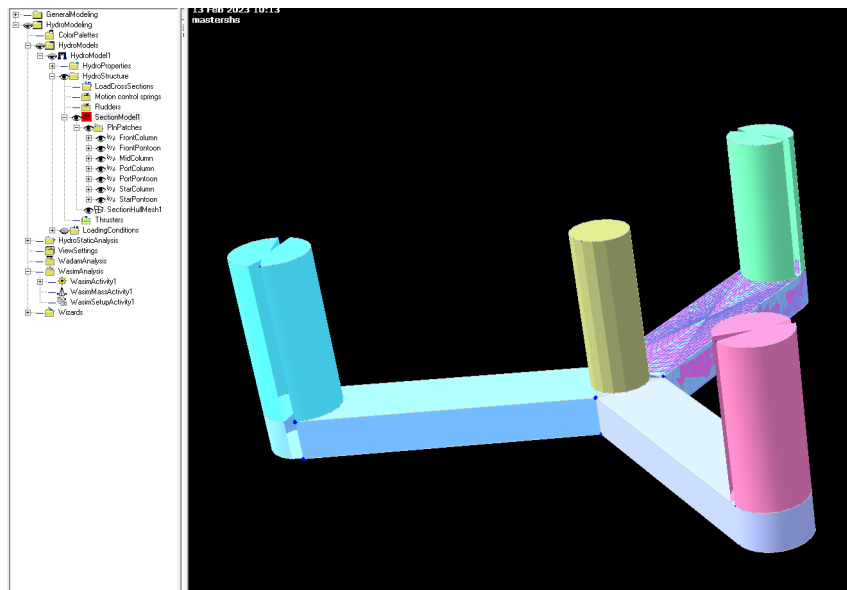

Figure A.1: Modeled floater as a Section Model in HydroD to extract as .pln-file

A.2 Further Modified Model

A third option to the rigid WT and the modified WT explained in chapter 5, is the flexible WT. This model is an even further modified model of the modified WT. It also contains RIFLEX elements for the columns as illustrated in Figure A.2.
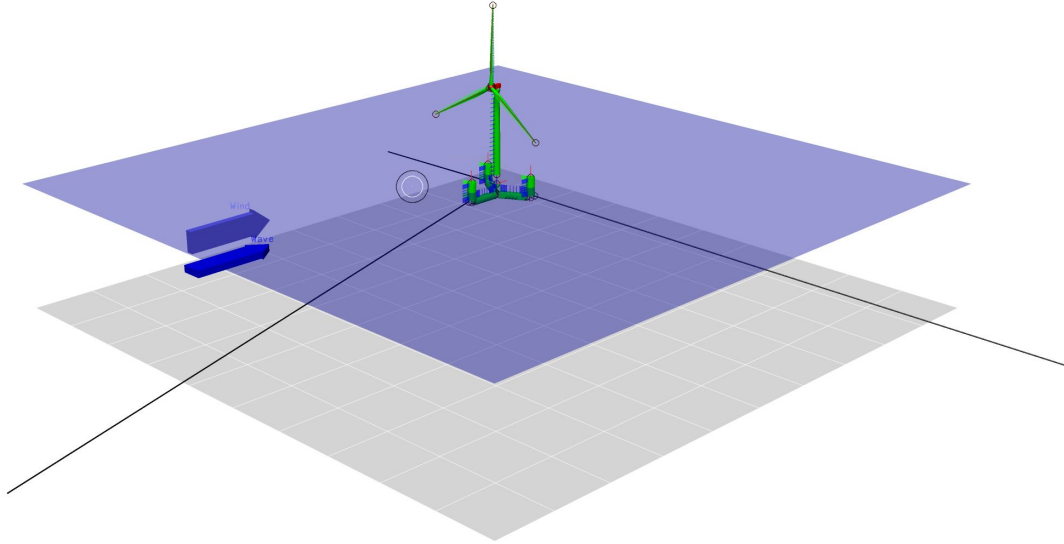

Figure A.2: Attempt of a more flexible model of the wind turbine in SIMA

The model is created using RIFLEX-elements for the columns. The pontoons and columns are connected with SIMO-bodies in the transitions from pontoon to column. The RIFLEX-elements are connected to the SIMO bodies by dummy transitions, the same as for the Modified WT. The Flexible WT model is also analyzed through decay tests. The eigenperiod and frequency of the flexible model from the tests are listed in Table A.1.

	Flexible model in this thesis		Flexible model by Li et al [23]	
	Period	**Frequency**	**Period**	**Frequency**
Unit	[s]	[Hz]	[s]	[Hz]
Surge	132.8	0.0075	135.1	0.0074
Sway	133.85	0.0075	135.1	0.0074
Heave	22.09	0.0453	20.66	0.0484
Roll	25.26	0.0396	28.57	0.0350
Pitch	25.28	0.0395	28.74	0.0348
Yaw	88.55	0.0113	88.50	0.0113

Table A.1: Comparison of eigenvalues of Flexible model and a flexible model presented by Li et al. [23]

In SIMA, the RIFLEX-elements are Morison, slender system. This is difficult to model, as the theory works for higher periods, but is not capturing the effect correctly for lower periods. Therefore, in SIMA simulations, when modeling low wave periods, the limitations and assumptions of the Morison equation may become more pronounced, resulting in reduced accuracy.

However, a research paper published by Li et al. at NTNU, confirms the findings of the further flexible model [23]. The paper investigates a new approach where the floater is divided into multiple rigid bodies connected by flexible beams developed for the advanced modeling of flexible floaters in combination with coupled time-domain simulations. This method is the same as the Flexible model in this thesis. Table 5.1 presents the differences in the natural frequency from free decay simulations.

Comparing the results of Li et al. with the flexible model in this thesis, the results depict the same results, except for roll and pitch motions. The motion of the Flexible WT model is compared with the Modified WT model in Figure A.3, and the corresponding response spectra in Figure A.4. The illustrations illustrate how the roll and pitch motions generally respond differently than expected. Due to these responses, the Modified WT was further investigated in this thesis. With more time, the flexible model could have been investigated for fatigue damage due to wind and wave loads.
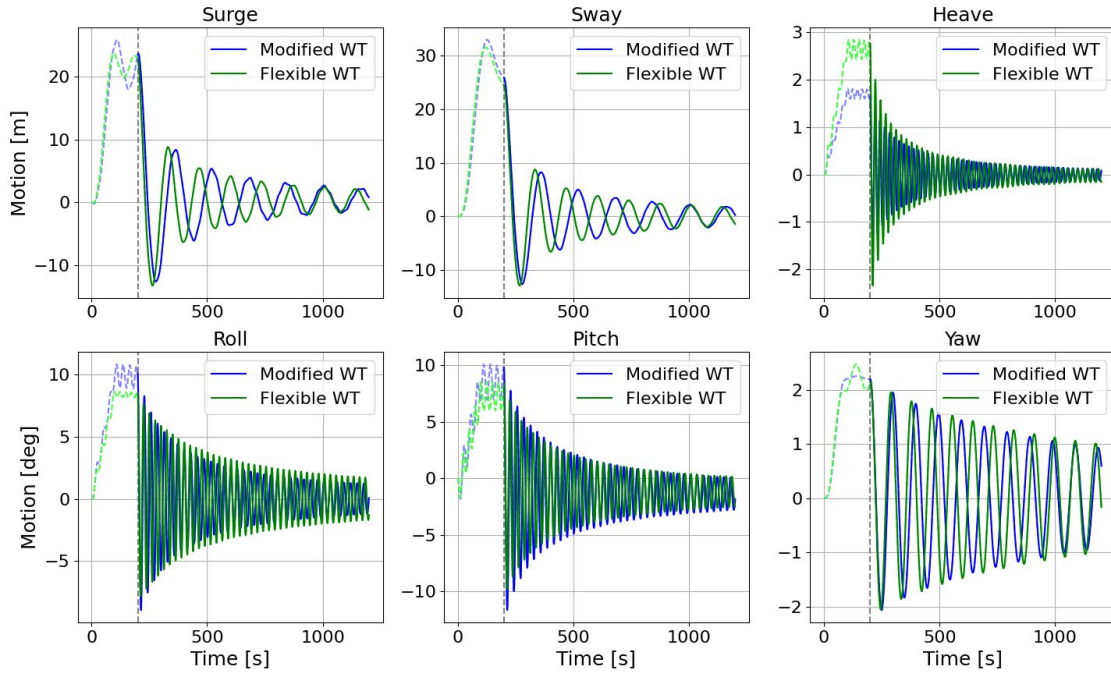

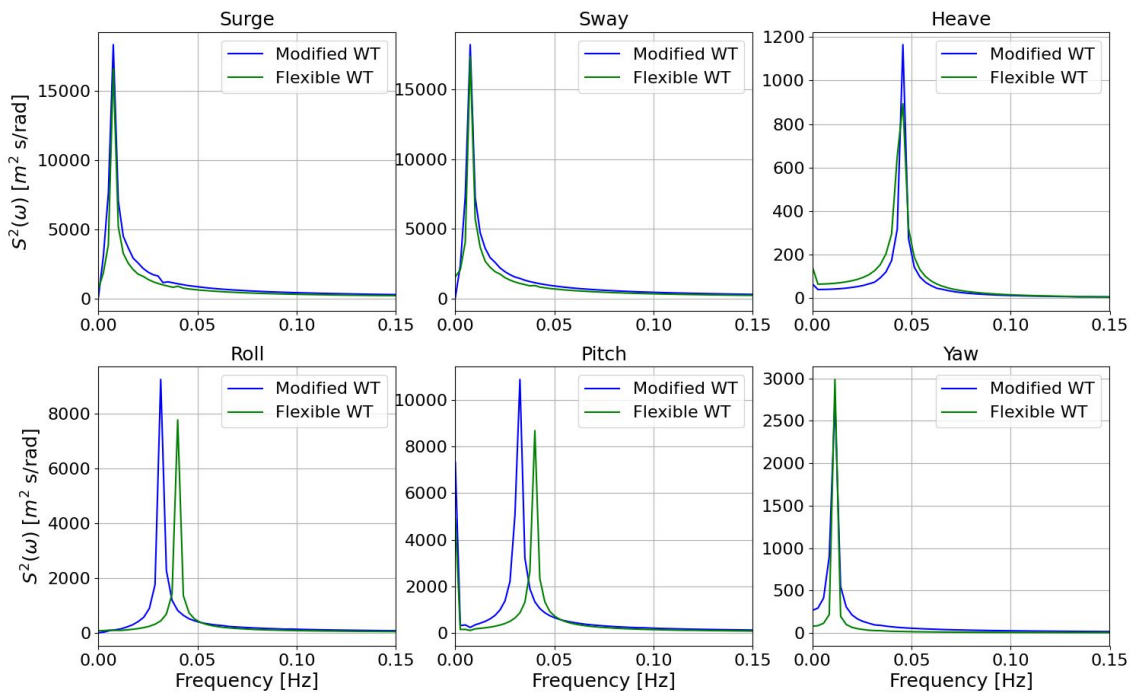Figure A.3: Motions of the Flexible WT and Modified WT as a response to decay tests

Figure A.4: Response spectra of bending moments of the Flexible WT and Modified WT

Appendix B

Fatigue Damage Due to Waves Alone With Probability

This section aims to show and discuss how fatigue damage (FD) evolves if the probability of wave conditions is taken into account, based on the Lifes50+ report [21]. The finding in this section is focused on the FD in the tower base and is compared to the findings of the waves alone without considering the probability in Section 5.9.2.

The development of the FD with increasing peak periods and significant wave height are presented for the parked and operating WT in Table B.1 and Table B.2, and additionally illustrated in Figure B.1. Generally, the results exhibit the same tendencies as for the analyses done without considering the probability. However, there are a few differences worth mentioning.

For a significant wave height of 0.5m, the development with increasing peak period is not increasing until a blunt peak at 7.5 - 8.5 s as for the cases without the probability. For the parked WT, the FD results are more or less in the order of 10^{-4}. The FDs of the operating WT experience an increase from an order of 10^{-6} to 10^{-5} from 5.5s to 6.5s, but generally remain stable.

Unlike the wave analysis without considering the probability, the FD for a peak period of 4.5s is higher for a wave height of 1.5m than 2.5m. However, in general, the FDs of the cases with a wave height of 2.5m are slightly higher than for 1.5m.

Comparing the fatigue damage values considering the probability versus those without, the values are significantly lower. All values fall within a safety margin of 0.1 and do not exceed 1. This indicates that the wind turbine remains within the safe operational range.

FD [-]		Hs [m]		
		0.5	1.5	2.5
	4.5	0.0001	0.0020	0.0008
	5.5	6.71e-05	0.0054	0.0214
Tp	6.5	0.00014	0.0078	0.0680
[s]	7.5	4.55e-05	0.0141	0.0790
	8.5	4.68e-05	0.0136	0.0570
	9.5	0.0002	0.0061	0.0291

FD [-]		Hs [m]		
		0.5	1.5	2.5
	4.5	7.72e-07	0.0003	0.00011
	5.5	9.56e-07	0.0011	0.0030
Tp	6.5	7.96e-06	0.0033	0.0231
[s]	7.5	6.84e-06	0.0105	0.0497
	8.5	7.60e-06	0.0110	0.0466
	9.5	1.64e-05	0.0053	0.0273

Table B.1: 20-year FD results for the parked WT considering probability

Table B.2: 20-year FD results for the operating WT considering probability
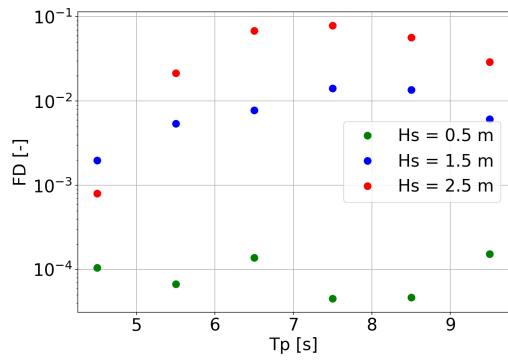
(a) Parked wind turbine
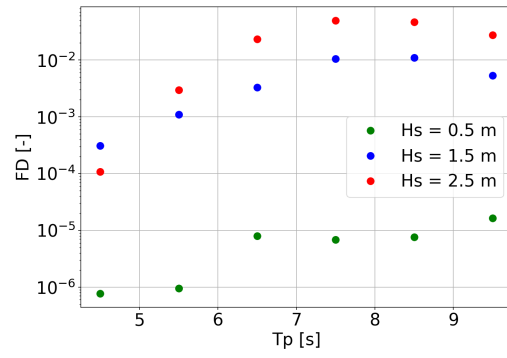
(b) Operating wind turbine

Figure B.1: 20-year fatigue damage results due to irregular wave loads alone considering the probability

Appendix C

Fatigue Damage Study of Class C

This section aims to demonstrate the progression of fatigue damage in accordance with the IEC 6400-1 standard. The changes in turbulence intensity have a negative exponential decrease as the wind velocity increases, which is explained and visually depicted in Figure 3.5. To observe the development of the fatigue damage for the wind turbine following the standard, the wind turbine is found to be of class C. This class represents the category for lower turbulence characteristics. The development of the fatigue damage following the standard is listed in Table C.1 and illustrated in Figure C.1. Observing the results, the fatigue damage generally follows the same trend as a TI of 15% and 5% presented in Section 5.10.1. The parked wind turbine depicts significantly lower fatigue damage than the operating wind turbine. This is due to the interaction of the rotating rotor. Moreover, the initial fatigue damage of the parked wind turbine decreases until it increases at 8 m/s. However, the operating wind turbine increases initially. Noticeably, all fatigue damage stays below 1.

FD [-]		Operating	Parked
	4	0.00447	0.00037
	6	0.0519	4.08e-05
Uw	8	0.12684	1.14e-05
[m/s]	10	0.27947	3.45e-05
	12	0.40616	3.02e-05
	14	0.71227	5.28e-05

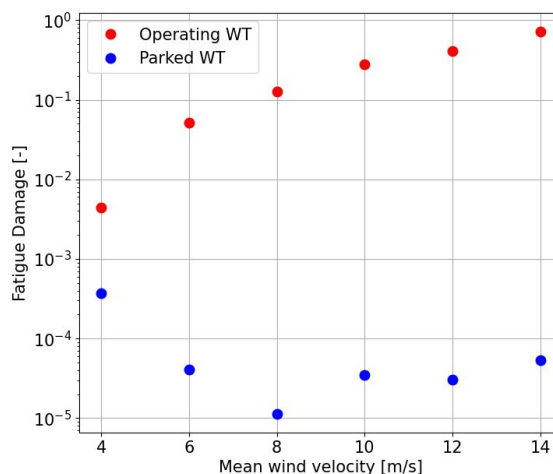Table C.1: 20-year FD results in the tower base, class C wind loads solely

Figure C.1: 20-year fatigue damage results in the tower base due to class C wind loads solely

Appendix D

Fatigue Damage Analysis of Disregarded Pontoon Cross-Sections

Generally, the cross-sections in the two additional pontoons show similar results to those discussed for pontoon 1 in the fatigue damage results chapter of this thesis. The intent of this chapter is to provide additional illustrations of the fatigue damage developments for the cross-sections in the two other pontoons. No further discussion is considered necessary, as the figures show the same outcomes.

D.1 Fatigue Damage Results in Pontoon 2

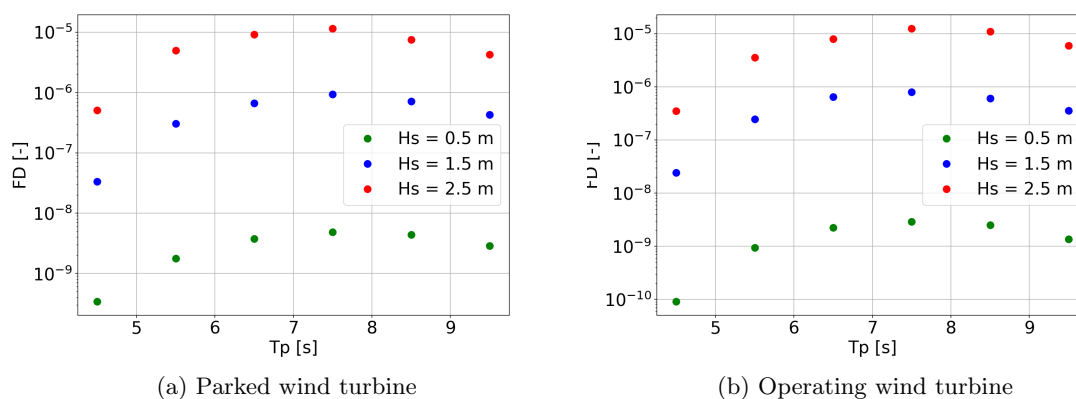### D.1.1 Fatigue Damage Due to Wave Loads Alone

(a) Parked wind turbine

(b) Operating wind turbine

Figure D.1: 20-year fatigue damage results in the pontoon (P2.1) due to waves alone

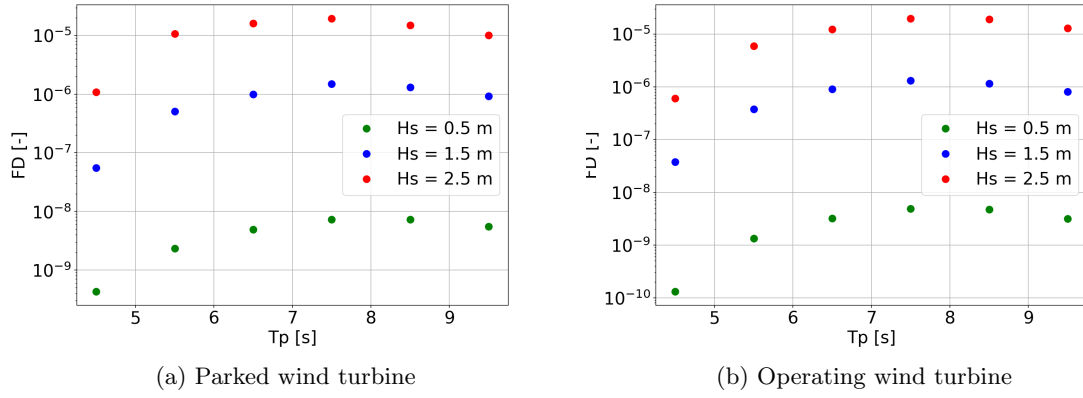(a) Parked wind turbine   (b) Operating wind turbine

Figure D.2: 20-year fatigue damage results in the pontoon (P2.2) due to waves alone
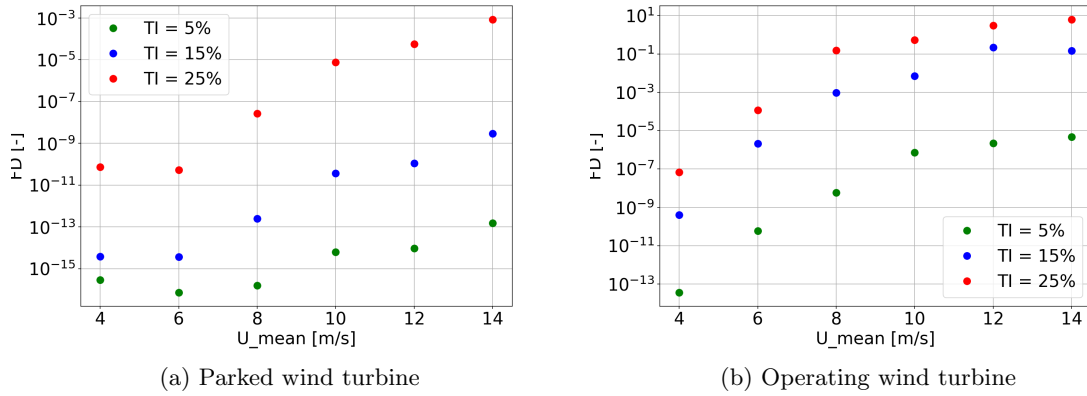
D.1.2   Fatigue Damage Due to Wind Loads Alone

(a) Parked wind turbine   (b) Operating wind turbine

Figure D.3: 20-year fatigue damage results in pontoon (P2.1) due to wind loads alone

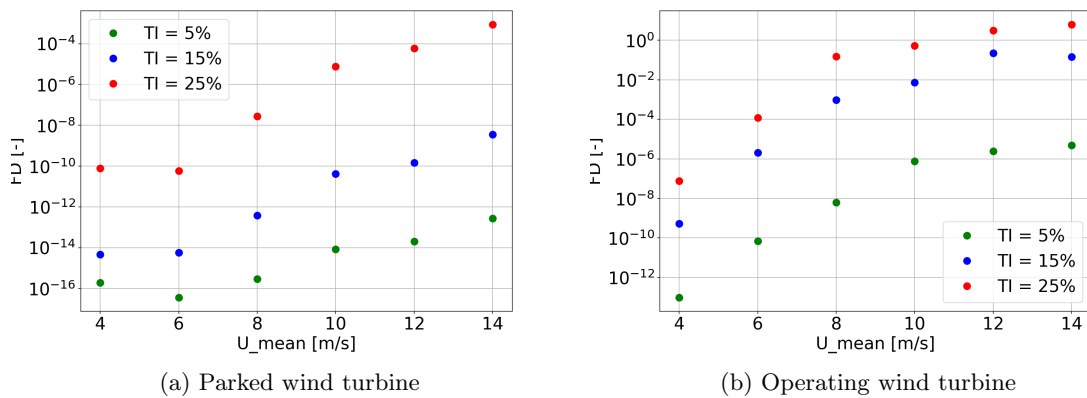(a) Parked wind turbine   (b) Operating wind turbine

Figure D.4: 20-year fatigue damage results in pontoon (P2.2) due to wind loads alone

D.2 Fatigue Damage Results in Pontoon 3

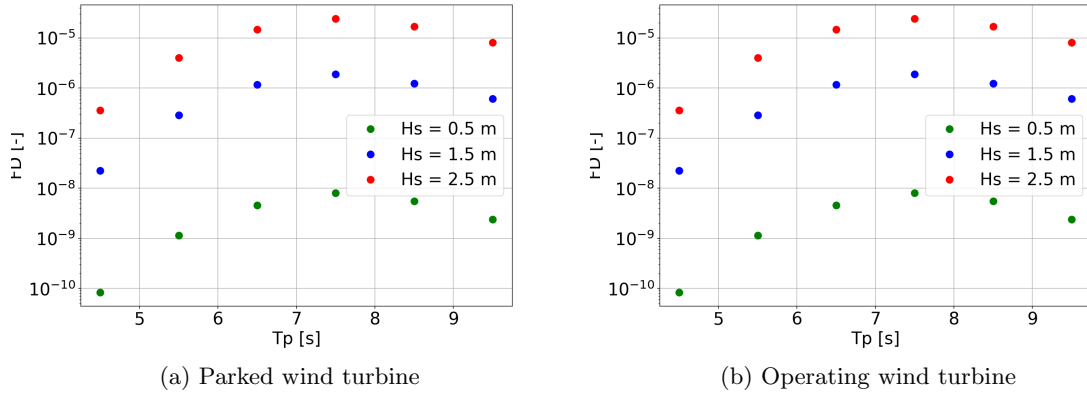### D.2.1 Fatigue Damage Due to Wave Loads alone

(a) Parked wind turbine

(b) Operating wind turbine

Figure D.5: 20-year fatigue damage results in the pontoon (P3.1) due to waves alone
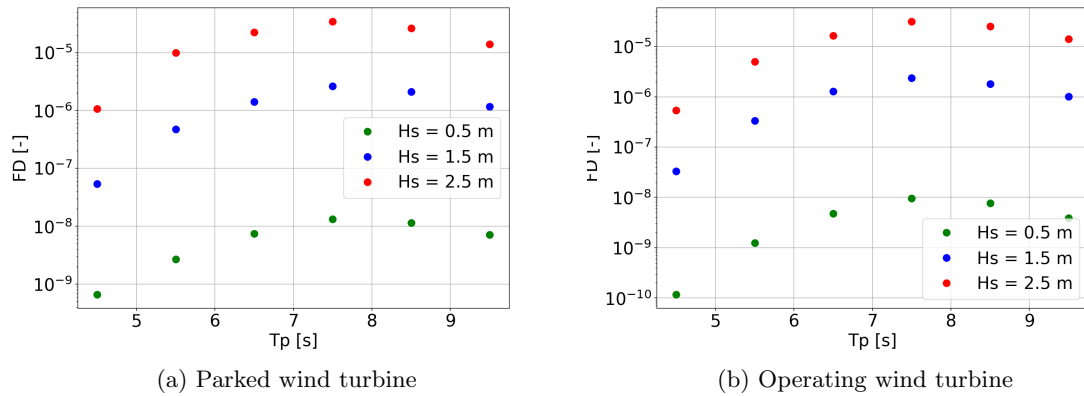

(a) Parked wind turbine

(b) Operating wind turbine

Figure D.6: 20-year fatigue damage results in the pontoon (P3.2) due to waves alone

D.2.2 Fatigue Damage Due to Wind Loads alone

(a) Parked wind turbine
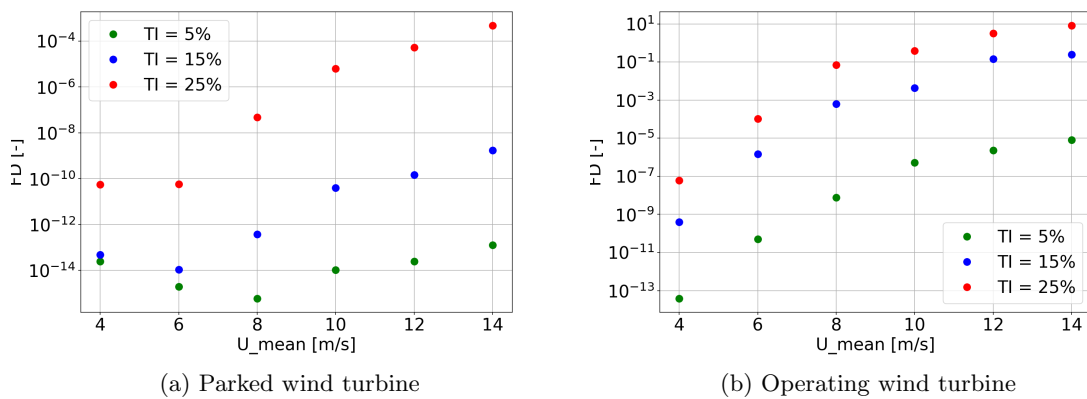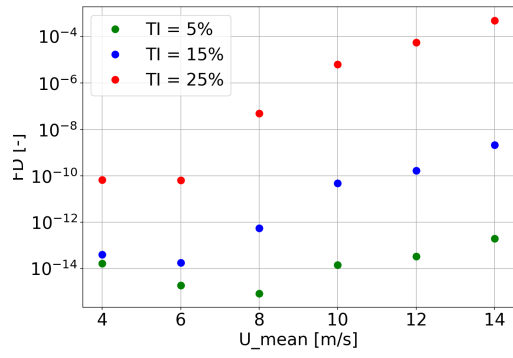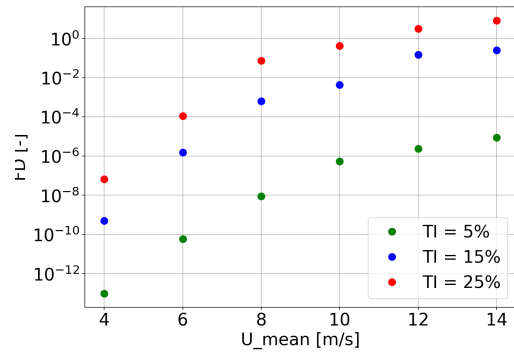
(b) Operating wind turbine

Figure D.7: 20-year fatigue damage results in pontoon (P3.1) due to wind loads alone

(a) Parked wind turbine

(b) Operating wind turbine

Figure D.8: 20-year fatigue damage results in pontoon (P3.2) due to wind loads alone

Appendix E

One-Peaked or Two-Peaked JONSWAP Spectrum

Two-peaked JONSWAP spectrum is better at capturing low frequent excitation on the structure. This could make the surge and sway motions more apparent in the response spectrum. The response spectra of the highest fatigue damage at Tp = 7.5 s are illustrated for both cases in Figure E.2. This illustrates how the structure experience more response from the tower, and response over a wider range of frequencies for the two-peaked spectrum than the one-peaked. However, the one-peaked spectrum experiences a more narrow and higher response due to the waves.
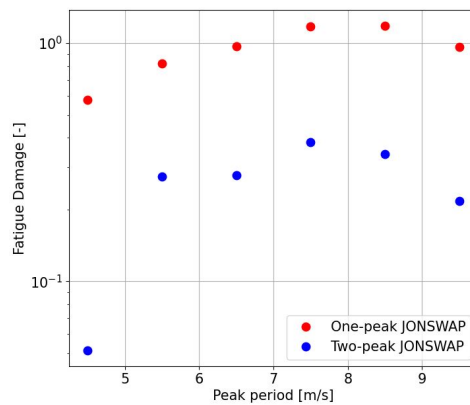

Figure E.1: Comparison fatigue damage due to using one-peaked or two-peaked JONSWAP spectrum
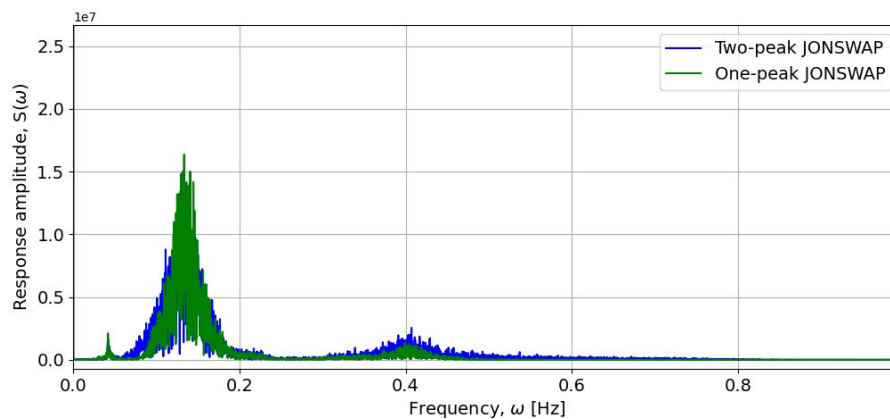

Figure E.2: Comparison of response spectra for one-peaked or two-peaked wave spectrum

Appendix F

Fatigue Analysis of Regular Waves Excitations

The aim of this chapter is to observe the influence of wave load conditions alone on fatigue damage for different sections of the wind turbine due to regular waves. Simulations have been done for both the wind turbine operating and parked. In the end, combined wind and wave conditions are observed.

F.1 Fatigue Damage on the Tower Base due to Regular Wave Conditions

The Fatigue Damage (FD) at the tower base, denoted as T0.1, are listed in Table F.1 and Table F.2. It can be observed a direct correlation between increasing wave height and larger FD values. The largest FDs are achieved for a wave height of 2.5m, and the lowest for a wave height of 0.5m. This observation applies to both the parked and operating WT.

FD [-]		Hs [m]		
		0.5	1.5	2.5
	4.5	0.0025	0.0428	0.5844
	5.5	0.0020	0.0236	0.1530
Tp	6.5	0.0135	1.6519	22.472
[s]	7.5	0.0597	11.406	42.143
	8.5	0.0504	10.813	42.774
	9.5	0.0094	1.579	18.130

Table F.1: 20-year FD results in tower base, regular wave loads for the parked wind turbine

FD [-]		Hs [m]		
		0.5	1.5	2.5
	4.5	7.48e-5	0.0270	0.5586
	5.5	9.92e-5	0.0148	0.1433
Tp	6.5	0.0065	1.5979	21.227
[s]	7.5	0.0492	10.207	37.553
	8.5	0.0440	10.153	39.414
	9.5	0.0065	1.5259	18.404

Table F.2: 20-year FD results in tower base, regular wave loads for the operating wind turbine

A more interesting observation is the development of FDs with increasing wave peak period. Initially, the FD increases, followed by a blunted peak during wave periods of 7.5 - 8.5s. the excitation forces.

The occurrence of the higher response during the 7.5 - 8.5s wave period range could potentially be connected to the interaction between the center column and the first column. When the bottom of a wave impacts one column, and the top of the wave hits the center column, it creates opposite-directed forces. This interaction can result in substantial excitation forces due to the contrasting pressures exerted on the columns. According to analytical calculations, considering the distance of 40.5m between the column and the tower base, this corresponds to a wave period of 10.2s, which could indeed result in significant excitation forces. However, this explanation does not fully account for the elevated response observed specifically within the 7.5 - 8.5s period range.

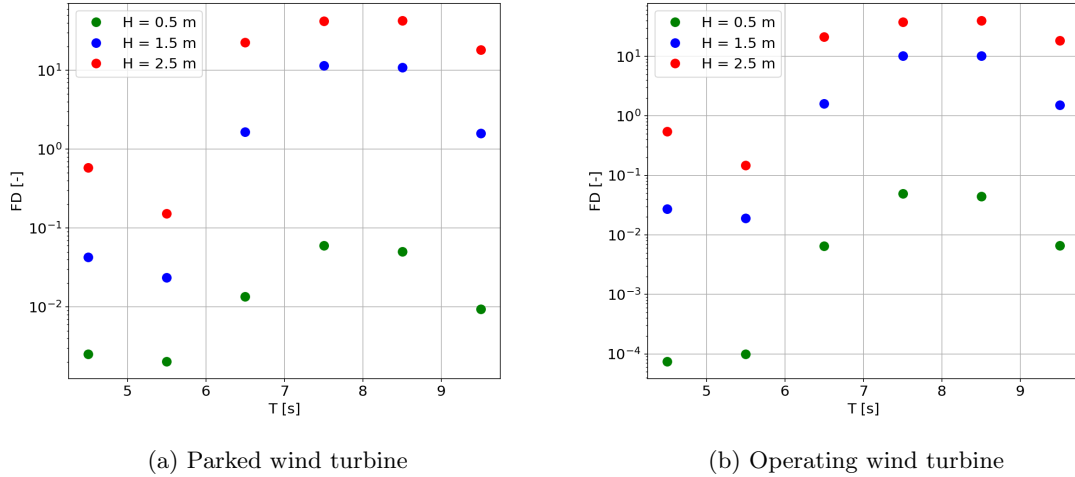(a) Parked wind turbine   (b) Operating wind turbine

Figure F.1: 20-year fatigue damage results on the tower base due to regular wave loads alone

Interestingly, examining the excitation forces obtained from HydroD, a peak at 9s becomes apparent, as shown in Figure 5.20. Notably, the pitch excitation force exhibits a peak at 8s. These findings imply that the increased fatigue damage experienced during the 7.5 - 8.5s period range may be due to these excitation forces.

Observing Table F.1 and **??**, there are minor differences between the parked and the operating WT. In general, the values of the parked wind turbine tend to be greater than those of the operating wind turbine. This is logical as the wind turbines are not actively functioning in the absence of wind. Nevertheless, subtle contrasts occur, potentially arising due to blade pitching for stability purposes, which alters the center of gravity (COG). Another contributing aspect could be the feathering of the blades when they are parked. Meanwhile, the blades of the operating WT are angled to achieve the thrust force giving the highest generated power.

F.2   Fatigue Damage on the Pontoon due to Regular Wave Conditions

In this section, the focus is on the cross-sections within the pontoons of the floater. These cross-sections are positioned 16.5 meters below the SWL, where the wave energy is reduced. Investigating these sections provides valuable insights into the variations between the SWL and the subsurface. Additionally, comparing the cross-section located near the tower (denoted P1.2) with the cross-section situated farther from the tower (denoted P1.1) offers crucial insights into the factors influencing the floater and underscores the important considerations during the design phase of the wind turbine.

FD [-]		Hs [m]		
		0.5	1.5	2.5
	4.5	2.06e-9	1.41e-7	2.62e-6
	5.5	5.33e-7	0.00014	0.00205
Tp	6.5	1.07e-5	0.0028	0.0420
[s]	7.5	1.71e-5	0.0034	0.0293
	8.5	2.71e-5	0.0063	0.0761
	9.5	1.62e-6	0.00033	0.0032

Table F.3: 20-year FD results in pontoon (P1.2), regular wave loads for the parked wind turbine

FD [-]		Hs [m]		
		0.5	1.5	2.5
	4.5	2.57e-10	1.552e-7	2.44e-6
	5.5	4.77e-7	0.00014	0.0020
Tp	6.5	1.021e-5	0.0026	0.0387
[s]	7.5	1.64e-5	0.0030	0.0263
	8.5	2.59e-5	0.0057	0.0661
	9.5	5.50e-6	0.0031	0.0029

Table F.4: 20-year FD results in pontoon (P1.2), regular wave loads for the operating wind turbine

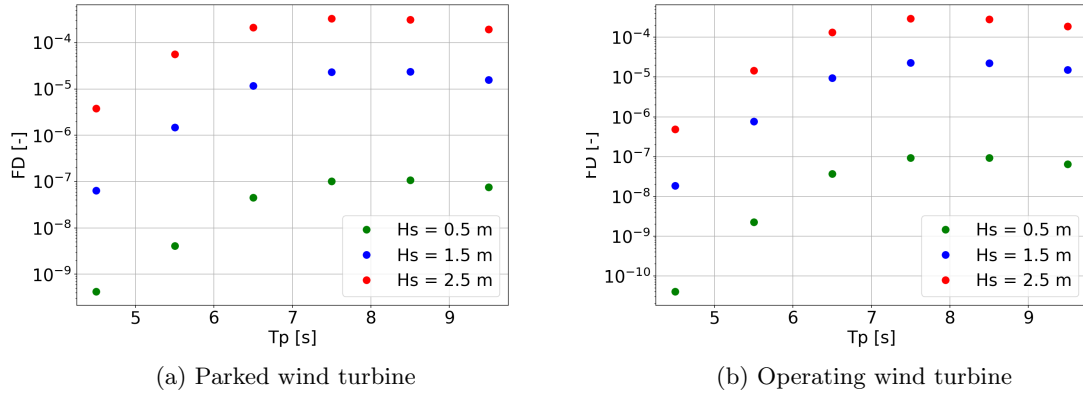| (a) Parked wind turbine | (b) Operating wind turbine |

Figure F.2: 20-year fatigue damage results in the pontoon cross-section P1.2 due to regular wave loads alone

Comparing the FD results of the pontoon with the damage of the tower base, there is a tremendous reduction. The FD results in the tower base exceed those in the pontoon by a factor of 10000. As mentioned previously, the wave energy is decreased at greater depths, a characteristic reflected in the obtained results.

Analyzing Figure F.3, the FD with increasing wave heights and periods follows a matching trend as for the tower base. It increases with higher wave heights, while also revealing peak values at 8.5 seconds and 7.5 seconds.

Further, the fatigue damage of the cross-section P1.2 can be compared to the cross-section further away from the tower. (P1.1). Analyzing the results in Table F.5 and Table F.6, the Fatigue Damage (FD) is slightly lower than for the section near the center column and tower base. As these sections are located at the same depths, and the same distance from each column, the influence of the tower base can be found to be close to ten times higher close to the tower base for some of the periods. Opposed to the tower base (T0.1) and the section close to the tower base (P1.2), the peak period occurs at 6.5 seconds, significantly higher than 7.5 seconds and 8.5 seconds, the peak for the other sections.

FD [-]		Hs [m]		
		0.5	1.5	2.5
	4.5	3.57e-10	1.76e-08	3.37e-08
	5.5	5.04e-07	0.00012	0.00124
Tp	6.5	4.52e-06	0.00115	0.01629
[s]	7.5	1.58e-06	0.00030	0.00250
	8.5	1.99e-06	0.00046	0.00533
	9.5	6.51e-08	1.24e-05	0.00011

Table F.5: 20-year FD results in pontoon (P1.1), regular wave loads for the parked wind turbine

FD [-]		Hs [m]		
		0.5	1.5	2.5
	4.5	1.20e-10	1.70e-08	3.88e-08
	5.5	4.83e-07	0.00011	0.00123
Tp	6.5	4.43e-06	0.00113	0.01586
[s]	7.5	1.57e-06	0.00031	0.00278
	8.5	1.94e-06	0.00043	0.00502
	9.5	6.24e-08	1.24e-05	0.00012

Table F.6: 20-year FD results in pontoon (P1.1), regular wave loads for the operating wind turbine
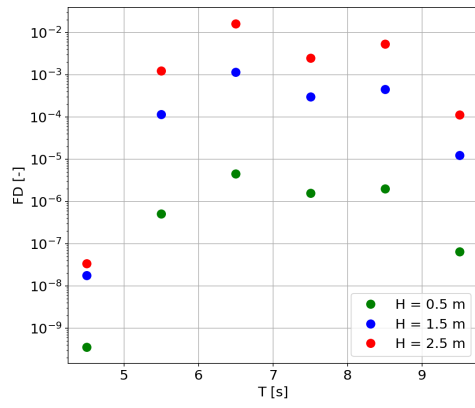
(a) Parked wind turbine
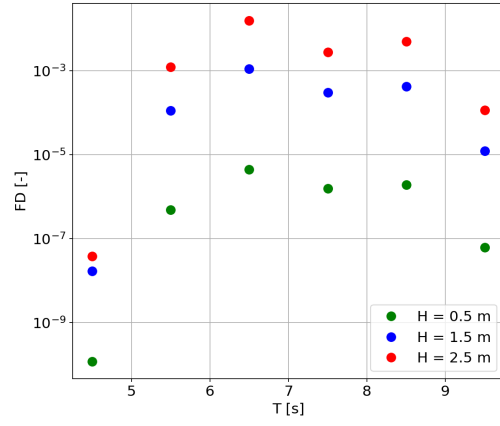
(b) Operating wind turbine

Figure F.3: 20-year fatigue damage results in the pontoon cross-section P1.1 due to regular wave loads alone